# Modeling the Statistics of Elementary Calcium Release Events

Ghanim Ullah and Peter Jung
Department of Physics and Astronomy and Quantitative Biology Institute, Ohio University, Athens, Ohio

ABSTRACT Elementary $Ca^{2+}$ signals, such as "$Ca^{2+}$ puffs", which arise from the release of $Ca^{2+}$ from endoplasmic reticulum through small clusters of inositol 1,4,5-trisphosphate receptors, are the building blocks for intracellular $Ca^{2+}$ signaling. The small number of release channels involved during a $Ca^{2+}$ puff renders the puffs stochastic, with distributed amplitudes, durations, and frequency, well characterized experimentally. We present a stochastic model that accurately describes simultaneously the statistical properties of the duration, amplitudes, frequencies, and spatial spread with a single set of parameters.

## INTRODUCTION

$Ca^{2+}$ signaling is one of the most important intracellular signaling mechanisms, controlling, e.g., the contraction of muscle cells, the release of neurotransmitter from neurons and astrocytes, and metabolic processes in liver and pancreas. Calcium signaling is characterized by a hierarchy of processes ranging from the spatially and temporally limited $Ca^{2+}$ puffs over global oscillations (in small cells, such as astrocytes) to propagating waves in large cells like oocytes (1–4).

The amplitude, duration, and spatial spread of elementary calcium release events (puffs and blips) varies widely (2,5,6). Sun et al. (5) showed that the amplitude of single events has a skewed distribution with a maximum $F/F_0$ (ratio of the fluorescence at each pixel during a response to the resting fluorescence at that pixel before simulation of Oregon Green 488 BAPTA-1) at 1.5 and a tail as high as 3.5. The signal mass distribution of discrete events is exponential (Fig. 8 *B* of Sun et al. (5)). The smallest events resolved correspond to a signal mass of $2 \times 10^{-20}$ mole and large events to $2 \times 10^{-18}$ mole. A current underlying a large puff is estimated by this study at 2.5 pA. This current was used to estimate the number of open channels involved in a single puff at five to eight. Another independent study led to a distribution where amplitudes span a range of values from a few tens to several hundreds of nanomolars (6).

Event-duration distribution (full duration at half-maximal amplitude (FDHM)) shows a peak at ~150 ms and an exponential decay for durations up to 600 ms (5,6). The distribution for spatial spread (full width at half magnitude (FWHM)) of puffs, obtained by Haak et al. (7), ranges from 0.5 $\mu$m to 3.5 $\mu$m (Fig. 5 *B* of Haak et al. (7)). The time interval between consecutive puffs follows a distribution with a peak at ~1.5 s or 3.4 s, depending on whether the puffs are focal (puffs that initiated $Ca^{2+}$ waves) or nonfocal (puffs that could not initiate $Ca^{2+}$ waves) (1).

A central role for the diverse intracellular $Ca^{2+}$ patterns is played by the release of $Ca^{2+}$ from the endoplasmic reticulum (ER) through small clusters of release channels called inositol 1,4,5-trisphosphate receptors ( $IP_3Rs$ ) (see Falcke (8) for an excellent review), which have an estimated 10–40 channels per cluster (9–11). Various studies on the structure of $IP_3Rs$ revealed a flower-like structure fitting within a cube with sides of ~18 nm (12). Thus, 10–40 $IP_3Rs$ would correspond to a cluster of the order of 50—150 nm in size. These clusters are randomly distributed, with an average distance of ~2–3 $\mu$m (11,13). The small number of channels per cluster causes a stochastic release of $Ca^{2+}$ through the cluster. The collective opening and closing of several channels in a single cluster causes the wide distribution of event sizes described above.

A mathematical description of $Ca^{2+}$ puffs should reproduce the statistical properties of $Ca^{2+}$ puffs, i.e., the distribution of puff amplitudes, puff durations, and frequencies. The available detailed statistical features of puffs are indeed an excellent test bench for mathematical models of calcium signaling. Stochastic versions of older models, like the DeYoung-Keizer model (14) or derivatives such as the Li-Rinzel model (15), can explain a number of features like the puff amplitude distribution (10), but predict event durations on the order of seconds. On the other hand, the peak of experimentally obtained distribution of duration is of the order of 150 ms (5,6) (also see Fig. 1). Similar problems are encountered in Swillens et al. (11) for realistic $IP_3$ concentrations used in experiments that investigate calcium puffs through uncaging of $IP_3$ (see Results).

In this article, we investigate whether a stochastic version of the kinetic model of the $IP_3Rs$ by Sneyd and Dufour (16) (SD model) can be used to accurately describe the experimentally observed statistical properties of $Ca^{2+}$ puffs, such as distributions of puff duration, puff amplitude, frequency, and spatial extent. The SD model incorporates new insights into the kinetics of the $IP_3$ receptor, including non-mass-action law kinetics for $Ca^{2+}$ binding and serial binding of $IP_3$ and $Ca^{2+}$ to activating binding sites. However, the SD

*Submitted August 29, 2005, and accepted for publication February 7, 2006.*

Address reprint requests to Ghanim Ullah, Dept. of Physics and Astronomy, Ohio University, Athens, OH 45701. Tel.: 740-593-9671; Fax: 740-593-0433; E-mail: ghanimul@helios.phy.ohiou.edu.



0006-3495/06/05/3485/11 $2.00

doi: 10.1529/biophysj.105.073460

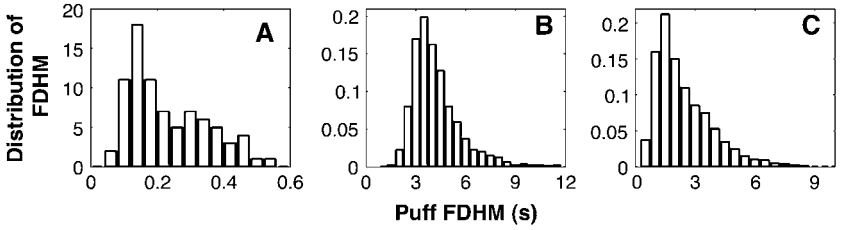


FIGURE 1 The distribution of puff durations observed by Sun et al. (5) (*A*) is compared with predictions using stochastic versions (10) of the Li-Rinzel model (15) (*B*) and the DeYoung-Keizer model (14) (*C*).

model, is modified to resolve an ambiguity in the kinetic states following Falcke (8).

A cluster is defined by a small group of $IP_3Rs$ that are geometrically close enough that, on the timescale of the channel kinetics, they share the same $Ca^{2+}$ concentration released by the channels. We model a single cluster of $IP_3R$ channels embedded in the ER membrane in contact with the cytosole, allowing the $Ca^{2+}$ released by ER to diffuse. Based on the estimates of Swillens et al. (11) and Shuai et al. (13), we consider the cluster to be composed of 20 $IP_3Rs$. We study the statistical distribution of amplitude, spatial spread, lifetime, and interpuff intervals and compare with the experimental data.

## MATERIALS AND METHODS

### The $IP_3R$ model

On the typical timescale of calcium release events (≈100 ms) and using the effective $Ca^{2+}$ diffusion coefficient of 30.0 $\mu m^2\ s^{-1}$, the diffusion length is of the order of $\sqrt{30\times0.1}\mu m \approx 1.73\mu m$, and thus larger than the size of the cluster. Thus, even in the absence of direct physical interaction, the $IP_3Rs$ within one cluster effectively interact by being exposed to almost the same $Ca^{2+}$ concentration. This interaction gives rise to the collective events underlying the calcium puffs described above.

For a single $IP_3$ receptor we adopted the kinetic model put forward by Sneyd and Dufour (16), according to which the receptor is composed of four independent subunits, each with four binding sites, one for $IP_3$, two for $Ca^{2+}$ activation, and one for $Ca^{2+}$ inactivation. The full kinetic scheme of a subunit is shown in Fig. 2 *A*. Lumping all the R states (R′, $\overline{R}$, and $\tilde{R}$) under R, $\tilde{O}$ and $\overline{O}$ states under O, and $\tilde{A}$ and $\overline{A}$ states under A, the subunit has essentially six states R, O, A, S, $I_1$, and $I_2$ (Fig. 2 *B*). In state R, neither $Ca^{2+}$ nor $IP_3$ is bound. The subunit can inactivate directly from this state, i.e., going to state $I_1$, by binding $Ca^{2+}$. Before the subunit can switch into the activated state A, it has to bind first $IP_3$ (state O) and subsequently $Ca^{2+}$. In the activated state, the subunit can inactivate directly by binding $Ca^{2+}$ to the inactivating binding site. While in the open state, O, the subunit can switch spontaneously to the shut state S if $IP_3$ is bound. Based on this skeleton of the model, the triangular motifs, e.g., $\tilde{R}$, R′, and $I_1$, were introduced to generate transition rates between R (lumped) and $I_1$ that do saturate with increasing $Ca^{2+}$ concentration (for details see Falcke (8) and Sneyd and Dufour (16)). The downside of this method, however, is that these motifs are not conservative with respect to $Ca^{2+}$. For example, if a subunit were to go through the cycle $\tilde{A}\rightarrow\overline{A}\rightarrow I_2\rightarrow\tilde{A}$, it would pick up a $Ca^{2+}$ ion (at the activating site) with each transition from $\tilde{A}$ to $\overline{A}$ without losing it in another transition of the cycle. The motifs consisting of $\tilde{R}$, $\overline{R}$, and $\tilde{O}$ and $\acute{R}$, $\tilde{R}$, and $I_1$ have the same problem. To solve this problem, we followed Falcke (8) and introduced three additional states $\acute{O}$, $\bar{I}_1$, and $\bar{I}_2$ into the scheme of Fig. 2 *A*. Thus, we replaced the motifs ($\acute{R}$, $\tilde{R}$, $I_1$), ($\tilde{R}$, $\overline{R}$, $\tilde{O}$), and ($\tilde{A}$, $\overline{A}$, $I_2$) of Fig. 2 *A* with new motifs shown in Fig. 2 *C* (the states $I_1$ and $I_2$ of Fig. 2 *A* are represented by $\tilde{I}_1$ and $\tilde{I}_2$ in Fig. 2 *C*). For the channel to be open, all four subunits must be activated.

### Consistency with the original Sneyd-Dufur model

Since the basic structure of our model is taken from the model by Sneyd and Dufour (16), we needed to verify that the modifications we made did not interfere with its ability to describe $Ca^{2+}$ oscillations. To compare our prediction with that of the original Sneyd-Dufour model (16), we followed their protocol in simplifying the equations through adiabatic elimination. In the scheme of Fig. 2, *A* and *C*, the following transitions are fast and the associated states can be considered in instantaneous equilibrium: $\tilde{R}\rightleftharpoons\overline{R}$, $\tilde{R}\rightleftharpoons\acute{R}$, $\tilde{O}\rightleftharpoons\acute{O}$, $\tilde{O}\rightleftharpoons\overline{O}$, $\tilde{I}_1\rightleftharpoons\bar{I}_1$, $\tilde{A}\rightleftharpoons\acute{A}$, and $\tilde{I}_2\rightleftharpoons\bar{I}_2$. We thus obtain $c\tilde{R}=L_1\acute{R}$, $c\tilde{R}=L_3\overline{R}$, $c\tilde{O}=L_5\overline{O}$, $c\tilde{O}=L_3\acute{O}$, $c\tilde{I}_1=L_1\bar{I}_1$, $c\tilde{A}=L_1\overline{A}$, and $c\tilde{I}_2=L_1\bar{I}_2$. Now, defining $R=\overline{R}+\tilde{R}+\acute{R}$, $O=\overline{O}+\tilde{O}+\acute{O}$, $I_1=\bar{I}_1+\tilde{I}_1$, $A=\tilde{A}+\overline{A}$, and $I_2=\tilde{I}_2+\bar{I}_2$, we arrive at the simplified kinetic scheme for the subunits of the $IP_3$ receptors shown in Fig. 2 *B*:

$$\begin{aligned}
\frac{dR}{dt} &= \phi_{-2}O - \phi_2 pR + (k_{-1}+l_{-2})I_1 - \phi_1 R\\
\frac{dO}{dt} &= \phi_2 pR - (\phi_{-2}+\phi_4+\phi_3)O + \phi_{-4}A + k_{-3}S\\
\frac{dA}{dt} &= \phi_4 O - (\phi_{-4}+\phi_5)A + (k_{-1}+l_{-2})I_2\\
\frac{dI_1}{dt} &= \phi_1 R - (k_{-1}+l_{-2})I_1\\
\frac{dI_2}{dt} &= \phi_5 A - (k_{-1}+l_{-2})I_2,
\end{aligned} \tag{1}$$

with the saturating (non-mass-action) binding rates

$$\begin{aligned}
\phi_1 &= \frac{(k_5 c + L_1 k_1)c}{L_1 + c\left(1+\frac{L_1}{L_3}\right)}\\
\phi_2 &= \frac{l_4 c + L_3 k_2}{L_3 + c\left(1+\frac{L_3}{L_1}\right)}\\
\phi_{-2} &= \frac{(l_{-4}+k_{-2})(c+L_3)}{L_3 + c\left(1+\frac{L_3}{L_5}\right)}\\
\phi_3 &= \frac{L_5 k_3}{L_5 + c\left(1+\frac{L_5}{L_3}\right)}\\
\phi_4 &= \frac{(k_4 L_5 + l_6)c}{L_5 + c\left(1+\frac{L_5}{L_3}\right)}\\
\phi_{-4} &= \frac{k_{-4}+l_{-6}}{1+\frac{c}{L_1}}\\
\phi_5 &= \frac{(k_5 c + L_1 k_1)c}{L_1 + c}.
\end{aligned} \tag{2}$$

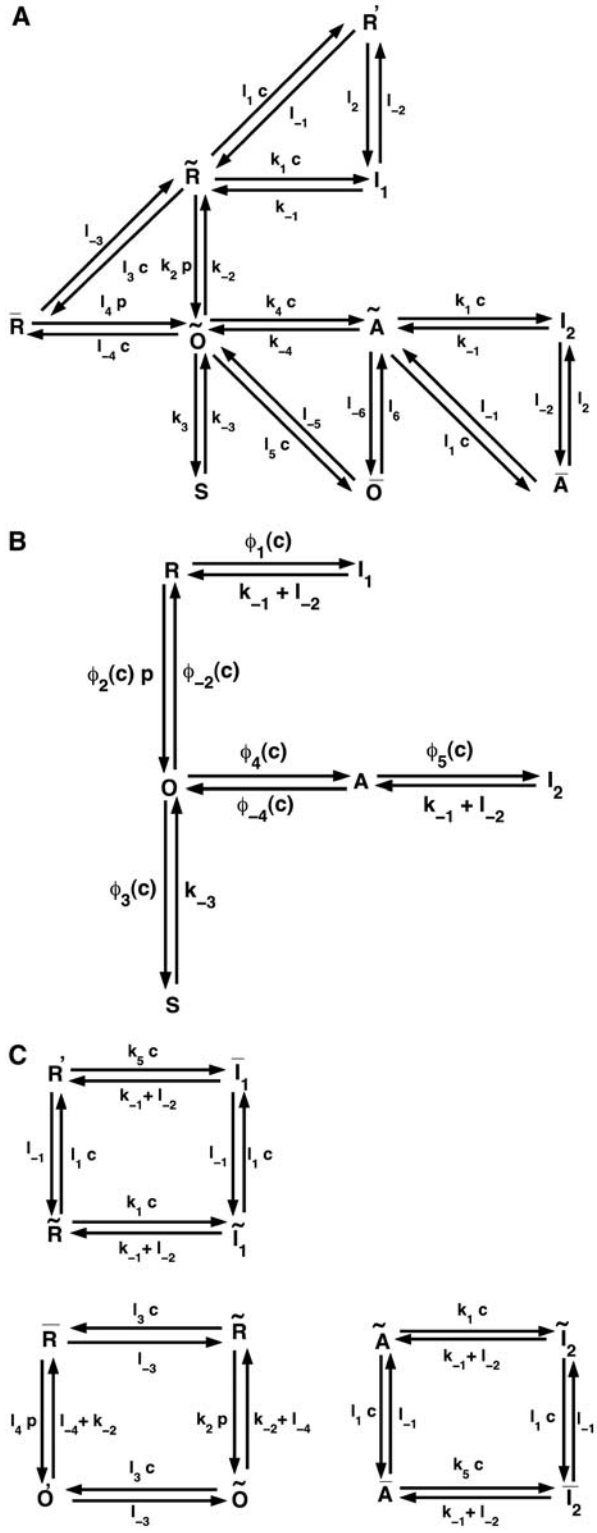


FIGURE 2 (*A*) The full model for one subunit of the $IP_3R$: *R*, receptor; *O*, open state; *A*, activated state; *S*, shut state; *I*, inactivated state. *c*, $Ca^{2+}$ concentration; *p*, $IP_3$ concentration (16). (*B*) Simplified scheme of the model with lumped nodes. Considering the fast equilibrium, this scheme is equivalent to the scheme of *A*. The open probability of the receptor for this scheme is $(0.1O + 0.9A)^4$, i.e., $(N_0/N)$ in Eq. 1 is replaced by $(0.1O + 0.9A)^4$. (*C*) Modifications of the triangular motifs of the SD model ( $\dot{R}$, $\tilde{R}$, $I_1$), ($\tilde{R}$, $\bar{R}$, $\tilde{O}$), and ($\tilde{A}$, $\bar{A}$, $I_2$) in *A* by rectangular motifs.

The steady-state open probability of the model (Eqs.1 and 2) as a function of the cytosolic $Ca^{2+}$ concentration for various $IP_3$ concentrations exhibits a bell-shaped curve for physiologically relevant $IP_3$ concentrations (results not shown). In Fig. 3, we show the bifurcation diagram of this reduced model with the $IP_3$ concentration as the control parameter. There is one steady state for low $IP_3$ concentrations, which loses stability at $IP_3 = 5.34\ \mu M$. This state remains unstable for $IP_3 < 11.73\ \mu M$, above which it gains stability through a subcritical Hopf bifurcation and remains stable as the $IP_3$ concentration increases further.

To compare our simplified scheme to that of the SD model (17), we consider the bifurcation diagram of the reduced scheme with $c_t$ as the control parameter (results not shown). The bifurcation diagram from our model is very similar to Fig. 2 (plot for a closed-cell model) of (17). However, the range of $c_t$ values where the model shows oscillatory behavior is slightly different. Thus, despite the change of the motifs, the model remains effectively similar to the original model (16).

## Spatiotemporal cytosolic $Ca^{2+}$ dynamics

As $Ca^{2+}$ is released through the cluster of $IP_3Rs$, it can spread out in the cytosol by diffusion. The spread of released $Ca^{2+}$ affects the dynamics of the subunits, as it lowers the $Ca^{2+}$ concentration at the channel cluster and thus plays an important role for the time course of the release event. The spread is modulated by mobile and stationary buffers that absorb free $Ca^{2+}$ and/or diffuse bound calcium. The experimental study of Dargan et al. (18) showed that EGTA (a buffer with a small ''on rate'') disrupts cluster-cluster interactions, thus dissociating $Ca^{2+}$ waves into local signals. BAPTA (a fast buffer), on the other hand, promotes the ''globalization'' of $Ca^{2+}$ signals. Such processes have been modeled with a myriad of reaction-diffusion equations for each buffer (19). As we only consider single puffs and their statistical properties, and not the interaction of clusters, we model the spread of released $Ca^{2+}$ by diffusion with an effective diffusion constant (20). Experimentally derived values of effective diffusion coefficients from confocal line scans (21) are $\sim 30\ \mu m^2/s$.

Thus, the spatiotemporal dynamics of the cytosolic $Ca^{2+}$ concentration, *c*, is modeled by a reaction diffusion equation with a stochastic term describing the influx of $Ca^{2+}$ through the $IP_3Rs$. If we define $V_{cluster}$ as the maximum flux of $Ca^{2+}$ generated by the channel cluster, the source density for cytosolic calcium is given by

$$J_{IPR} = V_{cluster}\left(\frac{N_o}{N}\right)(c_e - c), \tag{3}$$

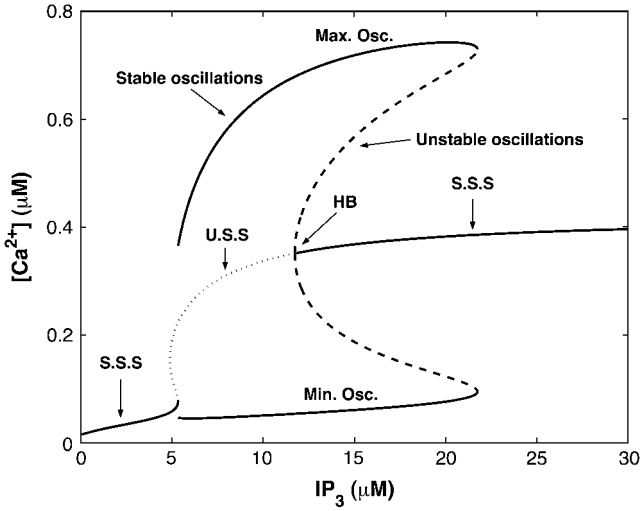


FIGURE 3 Bifurcation diagram of the simplified model, where S.S.S indicates stable steady states and U.S.S. unstable steady states; $V_{cluster} = 0.96\ s^{-1}$.

where $c_e$ denotes the calcium concentration in the ER, $N_o$ the number of open channels, and $N$ the total number of channels in the cluster. It is assumed that the spatial variability of the flux across the area of the channel cluster can be neglected. The leakage of $Ca^{2+}$ from ER to cytoplasm is described by

$$J_{leak} = V_{leak}(c_e - c). \quad (4)$$

Following Sneyd et al. (17), we used conservation of $Ca^{2+}$ to eliminate the $Ca^{2+}$ concentration in the ER, $c_e$, by $c_e = \gamma(c_t - c)$, with $c_t$ the total calcium concentration inside the cell, $c$ the average cytosolic $Ca^{2+}$ concentration, and $\gamma$ the ratio of cytoplasmic volume to ER volume.

Calcium is removed from the cytoplasm by the ATP-dependent sarcoendoplasmic reticulum $Ca^{2+}$ pump. We assumed that these pumps are distributed uniformly on the ER membrane and that the pump-flux is described by the quasi-Hill formula

$$J_{pump} = \left(\frac{V_{pump}c}{K_p + c}\right)\left(\frac{1}{c_e}\right), \quad (5)$$

where negative feedback from the luminal calcium concentration is taken into account through the term $1/c_e$. This term avoids overloading the ER with calcium by reducing the pump flow if luminal calcium is high. Denoting the effective diffusion coefficient of $Ca^{2+}$ by $D$, the equation for the cytosolic calcium concentration has the form

$$\frac{dc}{dt} = D\nabla^2 c + \zeta(x,y) \times J_{IPR} + J_{leak} - J_{pump}, \quad (6)$$

where the form function $\zeta(x,y)$ is 1 at a cluster location and 0 otherwise. The effective diffusion coefficient $D$ incorporates the effect of buffers. We use values for the effective diffusion coefficient derived from confocal line scans (21) of $\sim 30 \mu m^2/s$. Our model describes an isolated cell where the total amount of $Ca^{2+}$ is conserved. Only the exchange of $Ca^{2+}$ between cytoplasm and ER is taken into account. Table 1 lists the values of all model parameters.

**TABLE 1 Model parameters**

| Parameter | Value |
|---|---|
| Cluster flux coefficient $V_{cluster}$ | 600–800 $s^{-1}$ |
| Leak flux coefficient $V_{Leak}$ | 0.002 $s^{-1}$ |
| Maximum $Ca^{2+}$ uptake $V_{Pump}$ | 120 $\mu M^2$ $s^{-1}$ |
| Pump dissociation coefficeint $K_p$ | 0.18 $\mu M$ |
| Diffusion coefficient of free $Ca^{2+}$ D | 25-35 $\mu m^2$ $s^{-1}$ |
| Total $Ca^{2+}$ concentration inside the cell $c_t$ | 13.0 $\mu M$ |
| Cytoplasm volume/ER volume ($\gamma$) | 5.405 |
| Channel subunit parameters ($L_i = l_{-i}/l_i$) | |
| $k_1$ | 0.64 $\mu M^{-1}$ $s^{-1}$ |
| $k_{-1}$ | 0.04 $s^{-1}$ |
| $k_2$ | 37.4 $\mu M^{-1}$ $s^{-1}$ |
| $k_{-2}$ | 1.4 $s^{-1}$ |
| $k_3$ | 0.11 $s^{-1}$ |
| $k_{-3}$ | 29.8 $s^{-1}$ |
| $k_4$ | 4.0 $\mu M^{-1}$ $s^{-1}$ |
| $k_{-4}$ | 0.54 $s^{-1}$ |
| $k_5$ | 2.0 $\mu M^{-1}$ $s^{-1}$ |
| $l_1$ | 10.0 $\mu M^{-1}$ $s^{-1}$ |
| $l_3$ | 100.0 $\mu M^{-1}$ $s^{-1}$ |
| $l_5$ | 0.1 $\mu M^{-1}$ $s^{-1}$ |
| $L_1$ | 0.12 $\mu M$ |
| $L_3$ | 0.025 $\mu M$ |
| $L_5$ | 38.2 $\mu M$ |
| $l_2$ | 1.7 $s^{-1}$ |
| $l_{-2}$ | 0.8 $s^{-1}$ |
| $l_4$ | 1.7 $\mu M^{-1}$ $s^{-1}$ |
| $l_{-4}$ | 2.5 $s^{-1}$ |
| $l_6$ | 4707.0 $s^{-1}$ |
| $l_{-6}$ | 11.4 $s^{-1}$ |

## Stochastic simulation of the $Ca^{2+}$ release through a cluster of channels

Each subunit of an $IP_3R$ undergoes stochastic transitions between its states through stochastic binding and dissociation of the agonist. Thus, the state of the channel will be subject to stochastic fluctuations. If the number of channels per cluster is large, these fluctuations average out under the assumption that $Ca^{2+}$ assumes a uniform steady state across the cluster on the timescale of the channel kinetics. The small number of release channels per cluster requires stochastic modeling of the channels and subunits (9,10,19,22). Since the cluster is small, and thus the number of subunits is small, we can afford to simulate each subunit and each transition directly. If the subunit is at time $t$ in a state $i$, we have to determine the probabilities with which it remains in that state or switches into another state allowed by the kinetic scheme in Fig. 2 within the time interval $\delta t$. For example, if a subunit is in state $\tilde{R}$, possible transitions are to states $\acute{R}$, $\tilde{I}_1$, $\tilde{O}$, and $\overline{R}$. For a sufficiently small time interval $\delta t$, the probabilities for these transitions are given by

$$\begin{aligned} P_1 &\equiv P_{(\tilde{R}\to\acute{R})} = l_1 c\delta t, \\ P_2 &\equiv P_{(\tilde{R}\to\tilde{I}_1)} = k_1 c\delta t, \\ P_3 &\equiv P_{(\tilde{R}\to\overline{R})} = l_3 c\delta t, \\ P_4 &\equiv P_{(\tilde{R}\to\tilde{O})} = k_2 p\delta t, \end{aligned} \quad (7)$$

for which the values of the rates are listed in Table 1 and the $Ca^{2+}$ concentration referred to in these rates is the calcium at the channel cluster. The probability for the subunit to remain in its initial state $\tilde{R}$ is given by $P_5 \equiv P_{(\tilde{R}\to\tilde{R})} = 1 - (P_1 + P_2 + P_3 + P_4)$. To determine a transition, we followed the procedure outlined in part by the Gillespie algorithm (23). The unit interval is divided into five subintervals of lengths $P_i\delta t$, each subinterval $i$ representing the probability for one of the possible transitions. If a random number $\alpha$, drawn from a uniform distribution over the unit interval, falls into the subinterval $P_i\delta t$, the corresponding transition is performed. This procedure was followed for each subunit at each time interval $\delta t$. The time interval $\delta t$ was kept sufficiently small for the linear dependence of $P_i$ on the time interval to remain valid. The probability for the subunit to remain in the same state after $\delta t$ was always >95%. For most of the simulations in this study, a time step of $2 \times 10^{-5}$ s was used.

To incorporate the cytosolic diffusion of $Ca^{2+}$, we considered a planar patch of the ER membrane of size 5 $\mu m \times 5$ $\mu m$. The patch was discretized and represented by a two-dimensional lattice with grid distance $\Delta x$. The $Ca^{2+}$ concentration thus only depended on the coordinates $(x,y)$ of the flat ER membrane. A single cluster of 20 $IP_3Rs$ was placed at the center of the patch as a point source of $Ca^{2+}$, regardless of its actual physical size. It can be easily shown in a one-dimensional diffusion equation with a distributed source density that such a procedure generates an accurate $Ca^{2+}$ profile outside the channel cluster. Such a procedure is standard in classical mechanics and electrodynamics, where distributions of masses and charges are represented by point masses and point charges. We solved the partial differential equations by a forward difference method (24), with a spatial discretization of $\Delta x = 50$ nm. We considered the boundary conditions where calcium can diffuse out of the integrating patch to avoid piling up of $Ca^{2+}$ but cannot enter the patch from outside. We successfully tested the validity of the point-source release approximation at the cluster site by using a finer grid (of 20 nm) and distributing the channels over several grid elements with independent stochastic simulations of the $Ca^{2+}$ release within those grid elements. Differences between the results presented here were extremely small.

## RESULTS

The stochastic scheme described above allowed us to simulate calcium puffs generated by a single cluster. The simulation was performed for a cluster of 20 $IP_3Rs$ placed in a 5 $\mu$m $\times$ 5 $\mu$m cytosolic region with an effective $Ca^{2+}$ diffusion coefficient of 30 $\mu m^2\ s^{-1}$ and $IP_3$ concentration of 5.0 $\mu$M (for a discussion of this value, see section Amplitude distribution of $Ca^{2+}$ puffs). To be consistent with the experimental analysis of puffs, the $Ca^{2+}$ concentration was averaged across an area of 1 $\mu m^2$ that includes the cluster of $IP_3Rs$. In Fig. 4 *A*, we show a representative example of the time course of a $Ca^{2+}$ puff compared with the time course generated with a stochastic De Young-Keizer model (14) (Fig. 4 *B*) and an experimentally observed puff (Fig. 4 *D*). Each of the spikes in Fig. 4 *A* represents a $Ca^{2+}$ puff.

By visual comparison we can conclude that our new stochastic model generates puffs on a timescale consistent with experimental data. In the following sections, we generate statistical measures of the puffs, such as amplitude distribution and width distribution, to compare the model predictions with experimental data in more detail.

Fig. 4 *C* shows the total number of open channels corresponding to the time course of the $Ca^{2+}$ concentration shown in Fig. 4 *A*. The stochastic opening of channels initiates stochastic $Ca^{2+}$ release events. The resulting elevated $Ca^{2+}$ concentration in turn causes the termination of puffs. From our simulations, the number of open channels for the larger events (puffs) is four to ten, which is close to the five to eight estimated in Parker's lab (5) from their confocal line-scan data.

In Fig. 4 *E*, we show the temporal evolution of a single puff obtained from simulations in Fig. 4 *A* and compare it with the experimental puffs (Fig. 4 *D*) (5); the timescale of theoretical puffs and experimental puffs agrees well. Puffs

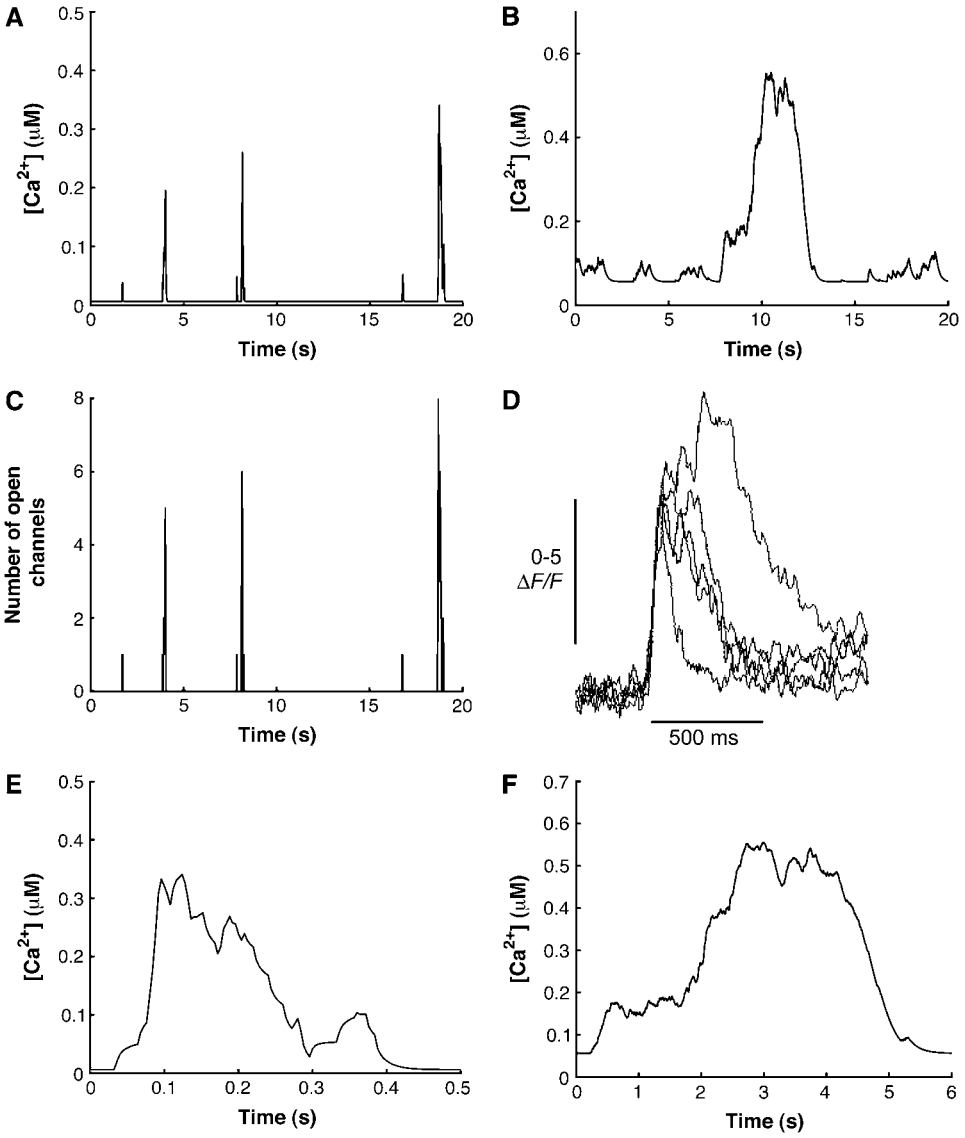


FIGURE 4 Calcium puffs of a cluster of 20 $IP_3Rs$ ($IP_3$ = 5.0 $\mu$M, $V_{cluster}$ = 600.0 $s^{-1}$, and $D$ = 30.0 $m^2\ s^{-1}$) predicted by our model (*A*) are compared with those generated by the stochastic De Young-Keizer model (*B*) and experiment (*D*). (*C*) Number of open channels during each release event. (*D*) Information taken from experimental data in Sun et al. (5). (*E*) Temporal evolution of a single puff from simulations in panel *A*. (*F*) Temporal evolution of a single puff obtained from a stochastic version of the De Young-Keizer model (14).

obtained from the stochastic version of the De Young-Keizer model (14) (Fig. 4 *F*) are much longer than the experimental puffs.

The $Ca^{2+}$ concentration around a single cluster with open channels is strongly localized, as shown in Fig. 5. Since the system is isotropic, the $Ca^{2+}$ profiles are radially symmetric and can be characterized by cross sections. Such a cross section is shown in Fig. 5. In this case, the $Ca^2$ concentration decayed by 82% at a distance 0.82 $\mu$m from the center of the cluster, which gives a decay constant equal to 0.24 $\mu m^{-1}$. The decay constant is obtained by fitting the $Ca^{2+}$ concentration profile in Fig. 5 to the exponential curve. Note that the actual profile is not as sharp as Fig. 5 indicates, since the point-source method produces profiles that are not accurate within the cluster. Within the cluster, the profile is relatively flat, with an almost constant $Ca^{2+}$ concentration (see Appendix).

## Amplitude distributions of $Ca^{2+}$ puffs

As shown in Fig. 4 *C*, the number of open channels during a single puff varies stochastically. As a consequence, the amplitudes of $Ca^{2+}$ puffs span a considerable range of values. Calcium puffs are generated experimentally by uncaging $IP_3$ or a homolog of $IP_3$ into the cell. $IP_3$ is released with an ultraviolet laser flash, but the exact amount is not known and there is uncertainty about the cytosolic concentrations of $IP_3$ required to evoke $Ca^{2+}$ signals among different cells (see, for example, Bird et al. (25) and Leybaert et al. (26)). We simulated the $IP_3R$ clusters for a range of $IP_3$ concentrations between 4.0 $\mu$M and 10 $\mu$M. However, the exact value of the $IP_3$ concentration does not affect the main findings of our study, because the affinity of $IP_3Rs$ can be adjusted as necessary to match the properties of different cells. For example, for smaller $IP_3$ concentrations, increasing the $IP_3$ binding rates $l_4$ and $k_2$ (see Fig. 2) yields statistical properties of puffs similar to those reported here. Since in the experiments the calcium concentration is collected from a volume of 1.0 fl (1.0 $\mu m^3$), we averaged the calcium concentration over an area of 1.0 $\mu m^2$ with the cluster of $IP_3Rs$ in the center. Each calcium release event that exceeded an amplitude of 20.0 nM was tracked and the maximum averaged $Ca^{2+}$ concentration during the event was recorded as the amplitude. The cut-off concentration of 20.0 nM was chosen, as it lies between blip amplitudes (single-channel release events with amplitudes of ~30.0 nM) and noise background. Fig. 6 shows the amplitude distribution for various effective diffusion coefficients and $IP_3$ values. Fig. 6 *A* depicts the puff-amplitude distribution obtained experimentally by Thomas et al.(6). The overall agreement between the simulations and the experiments is best at an effective diffusion coefficient of $D = 30\ \mu m^2/s$, consistent with estimates for the effective diffusion coefficient obtained from confocal line-scan data (21). Fig. 6 *B* shows the puff-amplitude distribution obtained from our model for $D = 30\mu m^2/s$ and an $IP_3$ concentration of 5.5 $\mu$M. At those parameter values, the puffs have a mean amplitude of 215.0 nM and range between 50 and 600 nM, in excellent agreement with experimental data by Thomas et al. (6). As the diffusion coefficient $D$ increases, the peak in the puff-amplitude distribution shifts toward smaller $Ca^{2+}$ concentrations (Fig. 6 *C*), because the $Ca^{2+}$ released through the $IP_3Rs$ diffuses away more rapidly and the number of open channels during a single puff decreases.

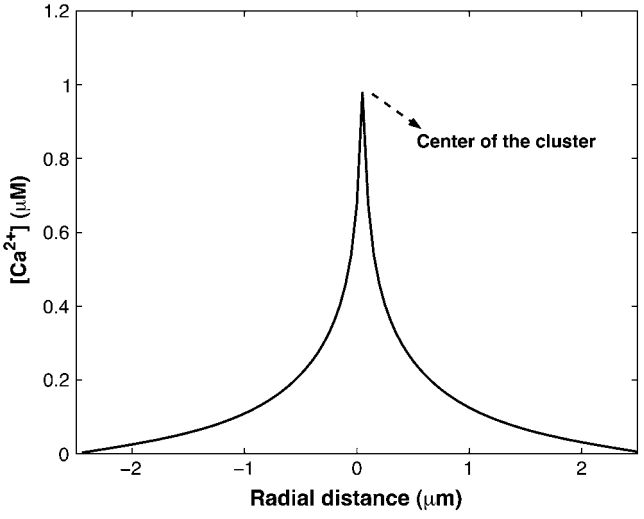


FIGURE 5 Spatial steady-state $Ca^{2+}$ profile for a single open cluster in two spatial dimensions. Parameters different from those in Table 1 are: $D = 30.0\ \mu m^2\ s^{-1}$, $IP_3 = 5.0\ \mu M$, and $V_{cluster} = 600.0\ s^{-1}$.

The amplitude distribution and its peak also depends on the $IP_3$ concentration. Fig. 6, *B* and *D*, shows the puff-amplitude distributions for two concentrations of $IP_3$, 5.5 $\mu$M (*B*) and 10 $\mu$M (*D*). Although the peak of the distribution in *D* is at approximately the same calcium concentration as in *B*, it is more symmetric around the maximum in *D*. Furthermore, the average puff amplitude in *D* is larger. The latter occurs because at larger $IP_3$ concentrations the open probabiliity of an $IP_3R$ is larger and hence more channels open during a release event, increasing the release of $Ca^{2+}$. This behavior is consistent with the experimental observation of Thomas et al. (6), where it has been shown that the peak of the puff-amplitude distribution shifts toward larger values as the histamine concentration (the agonist) increases (Fig. 5 of Thomas et al. (6)). The peak in Fig. 6 *B* resembles more the saw-toothed shape of the experimental puff-amplitude distribution. The amplitude distribution from our simulations is also qualitatively similar to the amplitude distribution of puffs from *Xenopus* oocytes (compare Fig. 6 with Fig. 8 *A* of Sun et al. (5)). Since the amplitude distribution obtained from HeLa cells in Thomas et al. (6) is calibrated in nanomolars (rather than fluorescence units), we use those amplitudes for quantitative comparison. Tovey et al. (2) showed that the kinetics of puffs are similar in various cells with different

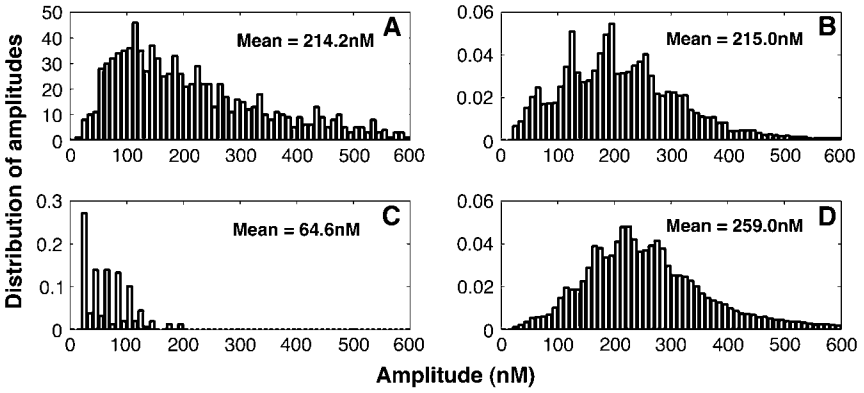


FIGURE 6 Amplitude distribution of puffs with various diffusion coefficients and $IP_3$ concentrations. (*A*) Experimental data. The vertical axis represents the number of events obtained for corresponding amplitudes. (*B*) $D = 30.0\ \mu m^2\ s^{-1}$. (*C*) $D = 100.0\ \mu m^2\ s^{-1}$. (*D*) $IP_3 = 10\ \mu M$, $D = 30\ \mu m^2\ s^{-1}$. (*B–D*) $V_{cluster} = 800.0\ s^{-1}$. The experimental data have been estimated by eye from Fig. 3 of Thomas et al. (6).

relative abundances of $IP_3R$ isoforms. We therefore hope that the results from our simulations are comparable to puffs from various cell types.

## Lifetime distribution of $Ca^{2+}$ puffs

A detailed examination of the elementary calcium release events obtained with improved resolution not only revealed variability in puff amplitudes but also their time course. Despite being evoked by identical stimulus strengths, the durations of the puffs varied almost 10-fold (5–7). The lifetime of puffs, or the FDHM, is defined as the time during which the calcium concentration at the puff site remains above one-half of the maximal value. Fig. 7 shows lifetime distributions of puffs for various diffusion coefficients and $IP_3$ values. Experimental data by Sun et al. (5) are shown in Fig. 7 *A*. Fig. 7 *B* shows the distribution of lifetimes obtained from our model at $D = 30\ \mu m^2/s$ and an $IP_3$ concentration of 5.5 $\mu$M. Both distributions (Fig. 7, *A* and *B*) exhibit a rise, a subsequent maximum at ~100 ms and then a decay to zero at ~600 ms. At short times, however, the experimental distribution and the model predictions seem to be different. This discrepancy is likely to be caused by a cut-off in the experimental protocol (for a more detailed discussion, see the next section). The peak of the puff lifetime distribution shifts toward smaller lifetimes as the diffusion coefficient $D$ increases (Fig. 7 *C*). This shift in the distribution occurs because for larger diffusion coefficients, calcium diffuses more rapidly away from the puff site, causing a decrease in the open probability for more channels and, hence, duration of puffs. Similar to the mean of the amplitude distribution, which shifts to larger amplitudes with increasing $IP_3$ concentration, the peak of the lifetime distribution shifts to larger lifetimes for increasing $IP_3$ concentration. In Fig. 7, *B* and *D*, we compare the puff lifetime distribution at $D = 30\ \mu m^2/s$ for $IP_3$ concentrations of 5.5 $\mu$M (*B*) and 10 $\mu$M (*D*).

## Correlation of lifetime and amplitude of puffs

In the experiment, only a small correlation was observed between the lifetime and the amplitude of puffs (Fig. 3 *C b* of Thomas et al. (6)). To test our model for such behavior, we calculated the correlation between puff amplitude $A$ and lifetime $T$ using

$$C = \frac{\langle (A - \langle A \rangle)(T - \langle T \rangle) \rangle}{(\langle (A - \langle A \rangle)^2 \rangle)^{1/2} (\langle (T - \langle T \rangle)^2 \rangle)^{1/2}}, \tag{8}$$

where $\langle\ \rangle$ indicates temporal averaging.

We find that our simulations predict correlation values of $C \approx 0.31$ for various $IP_3$ concentrations and calcium diffusion coefficients (we tested for $4\ \mu M < IP_3 < 7\ \mu M$ and $20\ \mu m^2/s < D < 35\ \mu m^2/s$). It is therefore expected that the

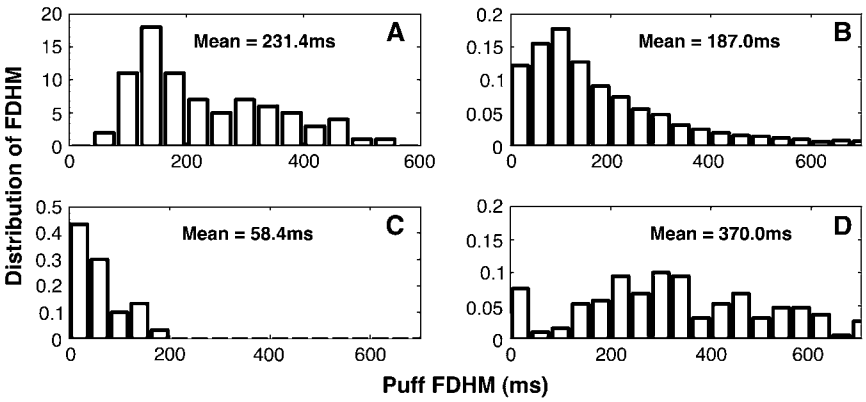


FIGURE 7 Distribution of puff widths at various values of the diffusion coefficient and $IP_3$ concentration. (*A*) Experimental data, estimated by eye from Fig. 2 of Sun et al. (5). The vertical axis represents the number of events for the corresponding duration. (*B*) $D = 30.0\ \mu m^2\ s^{-1}$. (*C*) $D = 100.0\ \mu m^2\ s^{-1}$. (*D*) $IP_3 = 10\ \mu M$, $D = 30\ \mu m^2\ s^{-1}$, and $V_{cluster} = 800\ s^{-1}$.

puffs with larger amplitudes will have larger lifetimes. However, this is not a strict rule and it is possible to observe puffs with smaller amplitude but larger lifetime and vice versa. Fig. 8 shows a scatter plot of puff amplitude versus lifetime at $IP_3 = 5.0\ \mu M$ and $D = 30.0\ \mu m^2\ s^{-1}$. Similar behavior can be seen for other $IP_3$ concentrations and values for $D$ (results not shown here).

### Interpuff-interval distribution of puffs

Another important characteristic of calcium puffs is the distribution of time intervals between two consecutive puffs. Marchant et al. (1) showed that a single puff cannot initiate a calcium wave by itself. However, several puffs at discrete sites coordinate to initiate a global response. The authors showed that the frequency of puffs increases before a wave is initiated. Also the interpuff interval becomes shorter (Figs. 8 and 10 of Marchant et al. (1)) before the generation of a wave. Their experimental investigation revealed interpuff-interval distributions that exhibit a single peak at ~1.5 s or 3.4 s, depending on whether the puffs are focal or nonfocal. The interpuff interval distribution obtained from our model is shown in Fig. 9 for various $IP_3$ concentrations and diffusion coefficients $D$. As shown in Fig. 9 *A*, the distribution shifts toward smaller times as the $IP_3$ concentration increases. For increasing diffusion coefficients, the distribution shifts toward larger times (Fig. 9 *B*). This increase occurs because the increased diffusion removes the calcium rapidly from the puff site, decreasing the chance for the channels to be reactivated.

### Width distribution

The spatial spread of puffs can vary between events, depending on their amplitude and channel open-times during each event. Haak et al. (7) analzyed the spatial spread of $Ca^{2+}$ sparks and puffs in oligodendrocyte progenitors. They showed that the phospholipase C/$IP_3$-linked muscarinic agonist MeCh-evoked puffs showed a spatial width distribution from ~0.5 to ~3.5 $\mu$m and peaked around 1.75 $\mu$m. In a separate set of experiments, Machacha (27) found puffs with an average width of ~2.0 $\mu$m in oocytes and a little wider in eggs.

Fig. 10 shows the distribution of spatial puff width obtained from our simulations at $IP_3$ concentrations of 5 $\mu$M (Fig. 10 *B*) and 6 $\mu$M (Fig. 10 *C*). To compute the spatial spread of puffs, we recorded the maximum calcium concentration at the cluster during each event at the center of the patch. The FWHM is defined as twice the radial distance from the center to the points where the $Ca^{2+}$ concentration has decreased to half of the amplitude at the center. As shown in Fig. 10, the distribution shifts toward larger values as $IP_3$ increases.

The agreement between data (Fig. 10 *A*) and simulations (Fig. 10, *B* and *C*) is not very good, most likely since we did not explicitly take into account the buffer kinetics.

## DISCUSSION

Elementary $Ca^{2+}$ release events such as puffs and blips are at the basis of local $Ca^{2+}$ signaling and can act as building blocks to generate global events like waves and oscillations (1–4). The characteristics of such elementary $Ca^{2+}$ release events convey important information about the gating and spatial distribution of the intracellular $Ca^{2+}$ release channels through which these events are generated. However, due to the limitations of microfluorimetric detection methods, neither the spatial dimensions nor the actual contents could

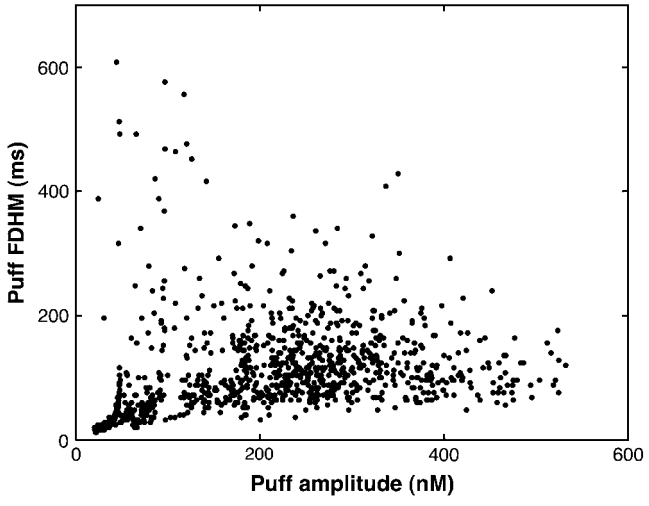


FIGURE 8 The scatter plot of puff FDHM versus puff amplitude demonstrates small correlations between lifetime and amplitude of puffs. Parameters not given in Table 1: $IP_3 = 5.0\ \mu M$, $V_{Cluster} = 600.0\ s^{-1}$, and $D = 30.0\ \mu m^2\ s^{-1}$.

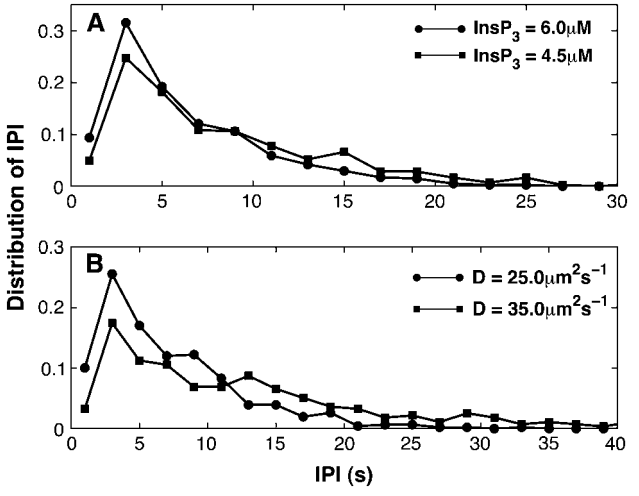


FIGURE 9 Interpuff interval distribution of puffs at various $IP_3$ concentrations (*A*) and various values for the diffusion coefficient $D$ (*B*). (*A*) $D = 25.0\ \mu m^2\ s^{-1}$. (*B*) $IP_3 = 5.0\ \mu M$. $V_{cluster} = 600.0\ s^{-1}$ for both panels *A* and *B*.

be estimated precisely. Hence, theoretical tools are used to estimate these features. We present here a stochastic model based on the kinetic Sneyd-Dufur model (16) that consistently describes multiple statistical features of elementary $Ca^{2+}$ release events with one set of parameters. Such a model can be used in the future as a basic building block to accurately predict more complex features, such as whole-cell signaling behavior.

The model combines a stochastic model for the $IP_3$ receptor that incorporates recent insights about the kinetics of the $IP_3$ receptor with solving a partial differential equation for the spread of $Ca^{2+}$ in the cytosol. We ignored the spatial resolution of the cluster and hence considered the cluster as a point source. This point-source approximation has been tested by simulations that take into account the spatial structure of the cluster (simulations performed with 20.0-nm grid size; results not shown). Consistent with the conclusion made by Swillens et al. (11), we conclude that the point-source approximation is accurate. The parameters used here to mimic the statistical properties of blips and puffs are based on estimates in Sneyd et al. (16) for whole-cell $Ca^{2+}$ signaling. Although the statistical properties of the elementary $Ca^{2+}$ puffs critically depend on the values of these parameters, this set of parameters—without further adjustment—led to good overall agreement between experimentally observed features such as puff amplitude and lifetime distributions and model predictions. We ignored the complicating effects of $Ca^{2+}$ buffers (19,20). To minimize these effects, we used the rapid buffering approximation of Wagner and Keizer (20) and the effective diffusion constant $D = \sim 30.0\ \mu m^2\ s^{-1}$, which is reduced in comparison to the diffusion coefficient of free $Ca^{2+}$ to account for $Ca^{2+}$-binding to buffers (28). Our numerical simulations confirm that puffs and blips vary in amplitude, duration, spatial spread, and interpuff interval (Figs. 4–10). The variation in these characteristics is due to the variability in the number of channels recruited and the open time of channels during individual puffs. Thus, our results indicate that a fixed puff morphology, which has been used previously (29), is not a good assumption for analysis of elementary $Ca^{2+}$ release events.

Using the approach discussed in the Materials and Methods, we were able to generate numerous features of the experimentally observed statistical properties of calcium puffs. Consistent with the theoretical study of Swillens et al. (11), our model predicts single-peak amplitude distributions for various $IP_3$ concentrations that have been consistently observed in experiments (5–7). An improvement over the results from Swillens et al. (11) occurred in that the shape of the distributions and range of amplitude values are quantitatively close to those observed by Parker's group (5) and Bootman's group (6). Although the amplitude distribution predicted by the model in Swillens et al. (11) has a peak that is close to the experimental value, the range of the amplitudes is much smaller than that observed experimentally (see Fig. 4, *A* and *B*, of Swillens et al. (11)). By increasing the $IP_3$ concentration in (11) arbitrarily, the range of amplitudes can be shifted to the experimentally observed values, but the maximum of the distribution moves to a too-large value.

Determining the shape and range of puff lifetime distributions was the primary motivation of this study. In experiments, a distribution with a single peak and a subsequent exponential decay has been found. Parker and coworkers showed that lifetime distributions of puffs span a range of values from 15 to 600 ms, with a peak at ~150 ms (5). Thomas et al. (6) reported a similar distribution. The theoretical study of Shuai et al. (10), using a stochastic version of the Li-Rinzel model (15), led to a single-peak distribution, but the predicted lifetimes are about one order of magnitude too large. As shown in Fig. 4, *D* and *F*, the puffs obtained from the more detailed stochastic De Young-Keizer model (14) are also much wider in temporal extent than those observed experimentally. The main reason for the prolonged puffs predicted with the De Young-Keizer model is the rapid binding and unbinding of $IP_3$ that leads to rapid sequences of channel opening and thus long cumulative opening before the subunit inactivates. We were not able to correct this feature of the De Young-Keizer model by adjusting parameters, since the required dramatic changes would strongly interfere with other desired features such as those present in the generation of $Ca^{2+}$ oscillations. In the Sneyd-Dufour model, these rapid bindings and unbindings do not occur. The subunit rapidly inactivates after it is activated, thus producing short channel open times.

Our model predicts a lifetime distribution (Fig. 7) that is in good overall agreement with the experimental findings of Sun et al. (5). However, our model predicts more events with shorter durations compared to that observed in the experiment (note the larger bars at FDHM ≈ 50 ms in Fig. 7). This difference could be caused by the experimental protocol used

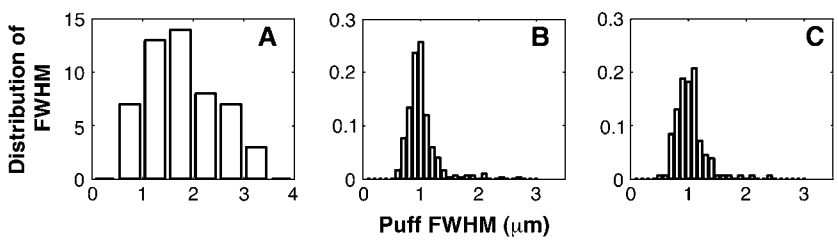


FIGURE 10 Distribution of spatial widths of $Ca^{2+}$ puffs at various values of the $IP_3$ concentration. (*A*) Experimental data obtained from Haak et al. (7). The vertical axis represents the number of events obtained with the corresponding width. (*B*) $IP_3 = 5.0\ \mu M$. (*C*) $IP_3 = 6.0\ \mu M$. Parameters not given in Table 1: $V_{Cluster} = 600.0\ s^{-1}$; $D = 25.0\ \mu m^2\ s^{-1}$.

by Parker et al. (30). They argued that the approximately Gaussian distribution of ''blips'' (Fig. 3 *B* of Parker and Yao (30)) might be based on the fact that many undetectable ''blips'' had been ignored. Motivated by this comment, we increased the cut-off level for puffs to 40.0 nm and indeed obtained a distribution that resembles that found in the experiment for short puffs as well (results not shown).

The variations in amplitude and duration of puffs are related to the variations in number and duration of open $IP_3Rs$ in the cluster. Often, a large number of open channels corresponds to puffs of large amplitude and long duration (Fig. 4, *A* and *C*). However, a large puff may also be caused by a small fraction of open $IP_3Rs$, but with long open times. Our model typically predicts 4 to 10 open channels during a puff (see Fig. 4 *C*), which is consistent with other studies and experimental data (5,10,11).

Consistent with the experimental findings, our stochastic model predicts a single-peak distribution of interpuff intervals. The model further predicts a shift of the distribution toward smaller values as the $IP_3$ concentration is increased. Marchant et al. (1) showed that the distribution of interpuff intervals peaks around time intervals of 1.5 s and 3.4 s, depending on whether the puffs are focal or nonfocal. The interpuff interval distributions for focal puffs peaks at a smaller interval value than those of nonfocal puffs. They also showed that global calcium waves can be initiated only with a larger $IP_3$ stimulus. Thus, it is expected that the interpuff interval distribution will shift toward smaller intervals, or, equivalently, the frequency of puffs will increase as the $IP_3$ concentration is increased (see Marchant et al. (1) for details). A similar behavior is observed in our model, where the mean interval shifts toward shorter intervals as the $IP_3$ concentration is increased (Fig. 9 *A*).

The diffusion coefficient also has an effect on interpuff interval distribution (Fig. 9 *B*). The distribution shifts slightly to larger intervals when the diffusion coefficient is increased. However, on the larger scale, that does not necessarily indicate that increased diffusion reduces the chance for puffs to initiate global calcium waves. Increased diffusion can coordinate the neighboring puff sites more effectively and thus cause a global calcium response.

The study presented here has important implications for modeling of intracellular calcium signaling and downstream processes. Calcium release from stores can signal different messages, depending on the spatial extent, amplitude, and frequency of the calcium elevation (for a recent review, see Niggli (31)), depending on the system that decodes the calcium signals. The time course of the puffs is important for, e.g., nuclear functions such as transcription (32), since local cytosolic increases of $Ca^{2+}$ cause increases in nuclear $Ca^{2+}$, which in turn regulate transcription. Hence, it is important that a model for local calcium elevation describes the amplitudes, durations, and frequencies quantitatively correctly. We present here a model that accurately describes all these features with one set of parameters.

## APPENDIX

The purpose of this appendix is to show that the assumption that all $IP_3$ channels are exposed to the same $Ca^{2+}$ concentration within one cluster is justified, although the point-souce approximation yields a profile that seems to indicate otherwise. To this end, we consider a simplified one-dimensional system with a cluster of length $2a$. The source of $Ca^{2+}$ is evenly distributed over the interval $[-a, a]$ of the $x$ axis. $Ca^{2+}$ released into the one-dimensional space diffuses and is absorbed with a linear rate $\gamma c$. The diffusion equation is given by

$$\frac{\partial c}{\partial t} = D\frac{\partial^2 c}{\partial x^2} - \gamma c + \tilde{j}\,\mathrm{rect}(x, x_0), \tag{9}$$

where $\tilde{j}$ describes the source density of $Ca^{2+}$ (concentration $c$) and $\mathrm{rect}(x, a) = 1$ for $|x| < a$ and $\mathrm{rect}(x, a) = 0$ otherwise. The steady-state profile is given by the solution of the ordinary differential equation

$$\frac{\partial^2 c}{\partial x^2} = \kappa^2 c - \frac{\tilde{j}}{D}\,\mathrm{rect}(x, a), \tag{10}$$

where $\kappa^2 = \gamma/D$. Solving Eq. 10 for $|x| < a$ and $|x| > a$ separately, with the integration constants obtained by requiring a profile that is continuous and once differentiable at $x = \pm a/2$ (which is a feature that follows directly from Eq. 10 by integrating over an $\varepsilon$-interval around $x = \pm\, a/2$) we find the solution in dimensionless variables $\bar{x} = \kappa x, \bar{a} = \kappa a$

$$c(\bar{x}) = \begin{cases} \dfrac{j}{2D\kappa}\dfrac{1}{\bar{a}}\dfrac{\sinh(\bar{a})}{\cosh(\bar{a})+\sinh(\bar{a})}\exp(-(|\bar{x}|-\bar{a})) & \text{for} |\bar{x}| > \bar{a} \\ \dfrac{\tilde{j}}{2D\kappa}\dfrac{1}{\bar{a}}\left(1-\dfrac{\cosh(\bar{a})}{\cosh(\bar{a})+\sinh(\bar{a})}\right) & \text{for} |\mathrm{x}| < \bar{a} \end{cases}, \tag{11}$$

with $j \equiv 2a\tilde{j}$.

Using the point-source approximation, we replaced the distributed source by a point source with the same total flux $j = 2a\tilde{j}$ as the distributed source, i.e.

$$\frac{\partial c}{\partial t} = D\frac{\partial^2 c}{\partial x^2} - \gamma c + j\delta(x). \tag{12}$$

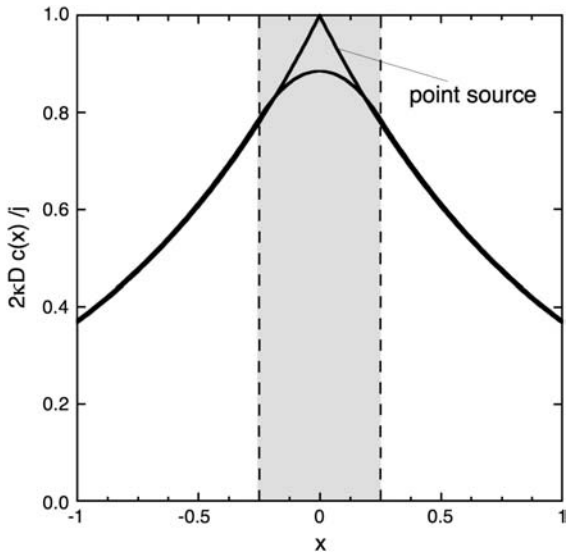


FIGURE 11 The one-dimensional steady-state profiles obtained in Eqs. 11 and 14 are compared. The shaded interval represents the spatial extent of the cluster. The point-exact solution is relatively flat inside the cluster, whereas the point-source solution exhibits a sharp peak at the point source.

The steady-state profile is determined by the ordinary differential equation

$$\frac{\partial^2 c}{\partial x^2} = \kappa^2 c - \frac{j}{D}\delta(x), \tag{13}$$

with $\delta(x)$ the Dirac's $\delta$ function. Solving this equation for $x < 0$ and $x > 0$ separately, and matching the solution such that the profile is continuous and the first derivative has a discontinuity $c'(0_+) - c'(0_-) = -j/D$ (obtained by integrating Eq. 13 from $-\varepsilon$ to $\varepsilon$), one finds the solution in dimensionless units $\bar{x} = x\kappa$,

$$c(\bar{x}) = \frac{j}{2\kappa D} e^{-|\bar{x}|}. \tag{14}$$

It is straightforward to see that both solutions (11,14) are identical in the limit $a \to 0$. For $\bar{a} = 0.25$, i.e., when the diffusion-length $1/\kappa$ is twice the cluster size, we compare both solutions in Fig. 11. It is clear that outside the cluster $|x| > a$, both solutions agree well, whereas inside the cluster the actual profile is relatively flat, justifying the assumption that all $IP_3Rs$ are clamped to the same $Ca^{2+}$ concentration. The sharp profile in Fig. 5 is thus an artifact of the point-source approximation within the spatial extent of the cluster and does not indicate that the $Ca^{2+}$ concentration varies dramatically within the cluster.

This material is based upon work supported by the National Science Foundation ( IOB-0345500).

## REFERENCES


1. Marchant, J., N. Callamaras, and I. Parker. 1999. Initiation of $IP_3$-mediated $Ca^{2+}$ waves in *Xenopus* oocytes. *EMBO J.* 18:5285–5299.
2. Tovey, C. S., D. P. Smet, P. Lipp, D. Thomas, K. W. Young, L. Missiaen, D. H. Smedt, J. B. Parys, M. J. Berridge, J. Thuring, A. Holmes, and M. D. Bootman. 2001. Calcium puffs are generic $IP_3$-activated elementary calcium signals and are downregulated by prolonged hormonal stimulation to inhibit cellular calcium responses. *J. Cell Sci.* 114:3979–3989.
3. Callamaras, N., J. S. Marchant, X. P. Sun, and I. Parker. 1998. Activation and coordination of $IP_3$-mediated elementary $Ca^{2+}$ events during global $Ca^{2+}$ signals in *Xenopus* oocytes. *J. Physiol.* 509:81–91.
4. Bootman, M., E. Niggli, M. Berridge, and P. Lipp. 1997. Imaging the hierarchical $Ca^{2+}$ signalling system in HeLa cells. *J. Physiol.* 499: 307–314.
5. Sun, X. P., N. Callamaras, J. S. Marchant, and I. Parker. 1998. A continuum of $IP_3$-mediated elementary $Ca^{2+}$ signalling events in *Xenopus* oocytes. *J. Physiol.* 509:67–80.
6. Thomas, D., P. Lipp, M. J. Berridge, and M. D. Bootman. 1998. Hormone-evoked elementary $Ca^{2+}$ signals are not stereotypic, but reflect activation of different size channel clusters and variable recruitment of channels within a cluster. *J. Biol. Chem.* 273:27130–27136.
7. Haak, L. L., L. S. Song, T. F. Molinski, I. N. Pessah, H. Cheng, and J. T. Russell. 2001. Sparks and puffs in oligodendrocyte progenitors: cross talk between ryanodine receptors and inositol trisphosphate receptors. *J. Neurosci.* 21:3860–3870.
8. Falcke, M. 2004. Reading the patterns in living cells—the physics of $Ca^{2+}$ signaling. *Adv. Phys.* 53:255–440.
9. Falcke, M., L. Tsimring, and H. Levine. 2000. Stochastic spreading of intracellular $Ca^{2+}$ release. *Phys. Rev. E.* 62:2636–2643.
10. Shuai, J. W., and P. Jung. 2002. Stochastic properties of $Ca^{2+}$ release of inositol 1,4,5-trisphosphate receptor clusters. *Biophys. J.* 83: 87–97.
11. Swillens, S., G. Dupont, L. Combettes, and P. Champeil. 1999. From calcium blips to calcium puffs: theoretical analysis of the requirements for interchannel communication. *Proc. Natl. Acad. Sci. USA.* 96: 13750–13755.
12. Taylor, W. C., P. C. A. da Fonseca, and E. P. Morris. 2004. $IP_3$ receptors: the search for structure. *Trends Biochem. Sci.* 29:210–219.
13. Shuai, J. W., and P. Jung. 2003. Optimal ion channel clustering for intracellular calcium signaling. *Proc. Natl. Acad. Sci. USA.* 100:506–510.
14. DeYoung, G. W., and J. Keizer. 1992. A single pool inositol 1,4,5-trisphosphate-receptor-based model for agonist stimulated oscillations in $Ca^{2+}$ concentration. *Proc. Natl. Acad. Sci. USA.* 89:9859–9899.
15. Li, Y. X., and J. Rinzel. 1994. Equations for InsP3 receptor-mediated $Ca^{2+}$ oscillations derived from a detailed kinetic-model: a Hodgkin-Huxley like formalism. *J. Theor. Biol.* 166:461–473.
16. Sneyd, J., and J. F. Dufour. 2002. A dynamic model of the type-2 inositol trisphosphate receptor. *Proc. Natl. Acad. Sci. USA.* 99:2398–2403.
17. Sneyd, J., K. Tsaneva-Atanasova, D. I. Yule, J. L. Thompson, and T. J. Shuttleworth. 2004. Control of calcium oscillations by membrane fluxes. *Proc. Natl. Acad. Sci. USA.* 101:1392–1396.
18. Dargan, L. S., and I. Parker. 2003. Buffer kinetics shape the spatiotemporal patterns of $IP_3$-evoked $Ca^{2+}$ signals. *J. Physiol.* 553:775–788.
19. Falcke, M. 2003. Buffers and oscillations in intracellular $Ca^{2+}$ dynamics. *Biophys. J.* 84:28–41.
20. Wagner, J., and J. Keizer. 1994. Effects of rapid buffers on $Ca^{2+}$ diffusion and $Ca^{2+}$ oscillations. *Biophys. J.* 67:447–456.
21. Yao, Y., J. Choi, and I. Parker. 1995. Quantal puffs of intracellular $Ca^{2+}$ evoked by inositol trisphosphate in *Xenopus* oocytes. *J. Physiol.* 482:533–553.
22. Swillens, S., P. Champeil, L. Combettes, and G. Dupont. 1998. Stochastic simulation of a single inositol 1,4,5-trisphosphate-sensitive $Ca^{2+}$ channel reveals repetitive opening during 'blip-like' $Ca^{2+}$ transients. *Cell Calcium.* 23:291–302.
23. Gillespie, D. 1976. General method for numerically simulating stochastic time evolution of coupled chemical reactions. *J. Comput. Phys.* 22:403–434.
24. Burden, L. R., and J. D. Faires. 2001. Numerical Analysis, 7th Ed. Brooks/Cole, Stamford, CT.
25. Bird, J. G., K. G. Oliver, D. A. Horstman, J. Obie, and W. Putney, Jr. 1991. Relationship between the calcium-mobilizing action of inositol 1,4,5-trisphosphate in permeable AR4–2J cells and the estimated levels of inositol 1,4,5-trisphosphate in intact AR4–2J cells. *Biochem. J.* 273: 541–546.
26. Leybaert, L., K. Paemeleire, A. Strahonja, and M. J. Sanderson. 1998. Inositol-trisphosphate-dependent intercellular calcium signaling in and between astrocytes and endothelial cells. *Glia.* 24:398–407.
27. Machaca, K. 2004. Increased sensitivity and clustering of elementary $Ca^{2+}$ release events during oocyte maturation. *Dev. Biol.* 275:170–182.
28. Keizer, J., G. D. Smith, S. Ponce-Dawson, and J. E. Pearson. 1998. Saltatory propagation of $Ca^{2+}$ waves by $Ca^{2+}$ sparks. *Biophys. J.* 75: 595–600.
29. Huser, J., and L. A. Blatter. 1997. Elementary events of agonist-induced $Ca^{2+}$ release in vascular endothelial cells. *Am. J. Physiol.* 273: C1775–C1782.
30. Parker, I., and Y. Yao. 1996. $Ca^{2+}$ transients associated with openings of inositol trisphosphate-gated channels in *Xenopus* oocytes. *J. Physiol. (Lond.).* 491:663–668.
31. Niggli, E. 1999. Localized intracellular calcium signaling in muscle: calcium sparks and calcium quarks. *Annu. Rev. Physiol.* 61:311–335.
32. Lipp, P., D. Thomas, M. J. Berridge, and M. D. Bootman. 1997. Nuclear calcium signalling by individual cytoplasmic calcium puffs. *EMBO J.* 16:7166–7173.

# Assimilating Seizure Dynamics

**Ghanim Ullah[1]*, Steven J. Schiff[1,2]**

**1** Center for Neural Engineering, Department of Engineering Science and Mechanics, The Pennsylvania State University, University Park, Pennsylvania, United States of America, **2** Departments of Neurosurgery and Physics, The Pennsylvania State University, University Park, Pennsylvania, United States of America

## Abstract

Observability of a dynamical system requires an understanding of its state—the collective values of its variables. However, existing techniques are too limited to measure all but a small fraction of the physical variables and parameters of neuronal networks. We constructed models of the biophysical properties of neuronal membrane, synaptic, and microenvironment dynamics, and incorporated them into a model-based predictor-controller framework from modern control theory. We demonstrate that it is now possible to meaningfully estimate the dynamics of small neuronal networks using as few as a single measured variable. Specifically, we assimilate noisy membrane potential measurements from individual hippocampal neurons to reconstruct the dynamics of networks of these cells, their extracellular microenvironment, and the activities of different neuronal types during seizures. We use reconstruction to account for unmeasured parts of the neuronal system, relating micro-domain metabolic processes to cellular excitability, and validate the reconstruction of cellular dynamical interactions against actual measurements. Data assimilation, the fusing of measurement with computational models, has significant potential to improve the way we observe and understand brain dynamics.

**Citation:** Ullah G, Schiff SJ (2010) Assimilating Seizure Dynamics. PLoS Comput Biol 6(5): e1000776. doi:10.1371/journal.pcbi.1000776

**Editor:** Karl J. Friston, University College London, United Kingdom

**Received** January 19, 2010; **Accepted** April 1, 2010; **Published** May 6, 2010



**Funding:** This study was supported by NIH Grants No. R01MH50006 and No. K02MH01493, the Pennsylvania Keystone Innovation Zone Program and Tobacco Settlement, and a grant from the National Academies - Keck Futures Initiative. The funders had no role in study design, data collection and analysis, decision to publish, or preparation of the manuscript.

**Competing Interests:** The authors have declared that no competing interests exist.

* E-mail: ghanim@psu.edu

## Introduction

A universal dilemma in understanding the brain is that it is complex, multiscale, nonlinear in space and time, and we never have more than partial experimental access to its dynamics. To better understand its function one not only needs to encompass the complexity and nonlinearity, but also estimate the unmeasured variables and parameters of brain dynamics. A parallel comparison can be drawn in weather forecasting [1], although atmospheric dynamics are arguably less complex and less nonlinear. Fortunately, the meteorological community has overcome some of these issues by using model based predictor-controller frameworks whose development derived from computational robotics requirements of aerospace programs in 1960s [2,3]. A predictor-controller system employs a computational model to observe a dynamical system (e.g. weather), assimilate data through what may be relatively sparse sensors, and reconstruct and estimate the remainder of the unmeasured variables and parameters in light of available data. The result of future measured system dynamics is compared with the model predicted outcome, the expected errors within the model are updated and corrected, and the process repeats iteratively. For this recursive initial value problem to be meaningful one needs computational models of high fidelity to the dynamics of the natural systems, and explicit modeling of the uncertainties within the model and measurements [3–5].

The most prominent of the model based predictor-controller strategies is the Kalman filter (KF) [2]. In its original form, the KF solves a linear system. In situations of mild nonlinearity, the extended forms of the KF were used where the system equations could be linearized without losing too much of the qualitative nature of the system. Such linearization schemes are not suitable for neuronal systems with nonlinearities of the scale of action potential spike generation. With the advent of efficient nonlinear techniques in the 1990s such as the ensemble Kalman filter [6,7] and the unscented Kalman filter (UKF) [8,9], along with improved computational models for the dynamics of neuronal systems (incorporating synaptic inputs, cell types, and dynamic microenvironment) [10], the prospects for biophysically based ensemble filtering from neuronal systems are now strong. The general framework of the UKF differs from the extended KF in that it integrates the fundamental nonlinear models directly, along with iterating the error and noise expectations through these nonlinear equations. Instead of linearizing the system equations, UKF performs the prediction and update steps on an ensemble of potential system states. This ensemble gives a finite sampling representation of the probability distribution function of the system state [3,11–15].

Our hypothesis is that seizures arise from a complex nonlinear interaction between specific excitatory and inhibitory neuronal subtypes [16]. The dynamics and excitability of such networks are further complicated by the fact that a variety of metabolic processes govern the excitability of those neuronal networks (such as potassium concentration ($[K]$) gradients and local oxygen availability), and these metabolic variables are not directly measurable using electrical potential measurements. Indeed, it is becoming increasingly apparent that electricity is not enough to describe a wide variety of neuronal phenomena. Several seizure prediction algorithms, based only on EEG signals, have achieved reasonable accuracy when applied to static time-series [17–19]. However,

## Author Summary

To understand a complex system such as the weather or the brain, one needs an exhaustive detailing of the system variables and parameters. But such systems are vastly undersampled from existing technology. The alternative is to employ realistic computational models of the system dynamics to reconstruct the unobserved features. This model based state estimation is referred to as data assimilation. Modern robotics use data assimilation as the recursive predictive strategy that underlies the autonomous control performance of aerospace and terrestrial applications. We here adapt such data assimilation techniques to a computational model of the interplay of excitatory and inhibitory neurons during epileptic seizures. We show that incorporating lower scale metabolic models of potassium dynamics is essential for accuracy. We apply our strategy using data from simultaneous dual intracellular impalements of inhibitory and excitatory neurons. Our findings are, to our knowledge, the first validation of such data assimilation in neuronal dynamics.


many techniques are hindered by high false positive rates, which render them unsuitable for clinical use. We presume that there are aspects of the dynamics of seizure onset and pre-seizure states that are not captured in current models when applied in real-time. In light of the dynamic nature of epilepsy, an approach that incorporates the time evolution of the underlying system for seizure prediction is required. As one cannot see much of an anticipatory signature in EEG dynamics prior to seizures, the same can be said of a variety of oscillatory transient phenomena in the nervous system ranging from up states [20], spinal cord burst firing [21], cortical oscillatory waves [22], in addition to animal [23] and human [24] epileptic seizures. All of these phenomena share the properties that they are episodic, oscillatory, and have apparent refractory periods following which small stimuli can both start and stop such events.

It has recently been shown that the interrelated dynamics of $[K]$ and sodium concentration ($[Na]$) affect the excitability of neurons, help determine the occurrence of seizures, and affect the stability of persistent states of neuronal activity [10,25]. Competition between intrinsic neuronal ion currents, sodium-potassium pumps, glia, and diffusion can produce slow and large-amplitude oscillations in ion concentrations similar to what is observed physiologically in seizures [26,27].

Brain dynamics emerge from within a system of apparently unique complexity among the natural systems we observe. Even as multivariable sensing technology steadily improves, the near infinite dimensionality of the complex spatial extent of brain networks will require reconstruction through modeling. Since at present, our technical capabilities restrict us to only one or two variables at a restricted number of sites (such as voltage or calcium), computational models become the "lens" through which we must consider viewing all brain measurements [28]. In what follows, we will show the potential power of fusing physiological measurements with computational models. We will use reconstruction to account for unmeasured parts of the neuronal system, relating micro-domain metabolic processes to cellular excitability, and validating cellular dynamical reconstruction against actual measurements.

## Results

As a first example of assimilating neural data we used intracellular voltage data from a spiking pyramidal cell (PC) from the Cornu Ammonis region 1 (CA1) of rat hippocampus. Using only the noisy membrane potential measurement, $V$, we employed modified Hodgkin-Huxley equations to reconstruct and track all of the gating variables of the ion channels: sodium channel activation and inactivation variables $m$ and $h$, and potassium channel activation variable $n$ (Figure 1). Beginning with arbitrary initial conditions the root mean square (RMS) error between measured and estimated membrane potential changes with time (Figure 2). As is clear from the figure the RMS error converges to near zero within a few hundred milliseconds for the simulations shown in Figure 1. We also tracked the maximum conductance parameters of the ion channels (not shown).

### Model Inadequacy

Model inadequacy is an issue of intense research in the data assimilation community – no model does exactly what nature does. To deal with inadequate models, researchers in areas such as meteorology have developed various strategies to account for the inaccuracies in the models for weather forecasting [4,5,29]. In complex systems such as neuronal networks, the need to account for model inadequacy is critical. To demonstrate that UKF can track neuronal dynamics in the face of moderate inadequacy, we impaired our model by setting the sodium current rate constant $\alpha_m = 0.5$ instead of using the actual complex function of $V$, $\alpha_m(V)$ (see equation (2) for the functional form of $\alpha_m(V)$), and tracked it as a parameter (Figure 3). That is, we deleted the relevant function for

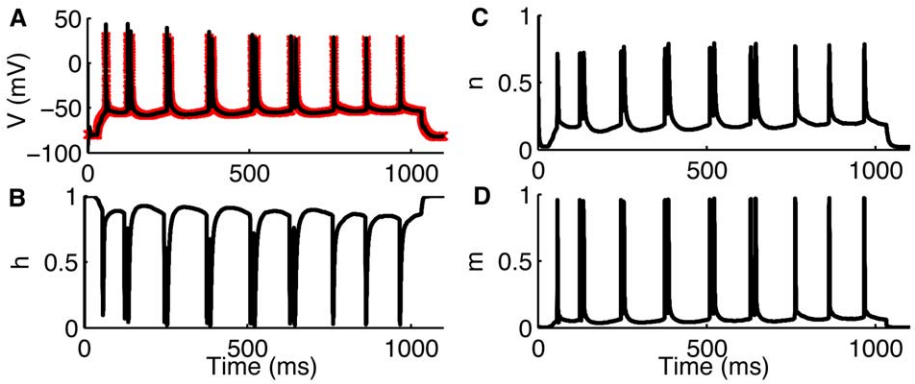


**Figure 1. Assimilating an intracellular membrane potential recording from CA1 hippocampal pyramidal neurons.** In (A) we show measured (red) and estimated (black) voltage, $V$. (B–D) Tracked Hodgkin-Huxley gating variables $h$, $n$, and $m$ respectively. Spiking in the pyramidal cell is generated by injecting a small current of 100 picoampere for 1sec. Data provided by Jokubas Ziburkus.
doi:10.1371/journal.pcbi.1000776.g001

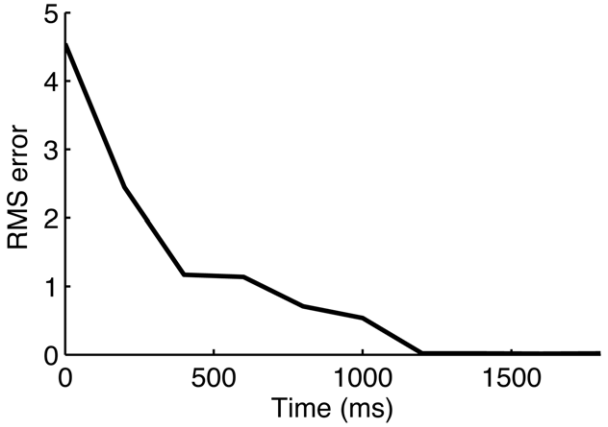


**Figure 2. Convergence of assimilation.** Root mean squared error for measured and estimated $V$ in Figure 1.
doi:10.1371/journal.pcbi.1000776.g002

$\alpha_m$ from the model and allowed UKF to update it as a parameter. The model with fixed $\alpha_m$ is by itself unable to spike, but when it is allowed to float when voltage is assimilated through UKF using the data from hippocampal pyramidal cells (PCs), it is capable of tracking the dynamics of the cell reasonably well. The $\alpha_m$ tracked by the filter is sufficiently close to its functional form values (within 25%) so that spiking dynamics can be reconstructed (Figure 3C and 3D). This occurs because Kalman filtering constantly estimates the trade off between model accuracy and measurements, expressed in the filter gain function [2,3]. This is an excellent demonstration of the robustness of this framework. Looking at the estimated values of $\alpha_m$ it also becomes clear that $\alpha_m$ in fact should be assigned the functional form rather than a constant value.

## Tracking Neuronal Microenvironment during Seizures

Despite decades of effort neuroscientists lack a unifying dynamical principle for epilepsy. An incomplete knowledge of the neural interactions during seizures makes the quest for unifying principles especially difficult [30]. Here we show that UKF can be employed to track experimentally inaccessible neuronal dynamics during seizures. Specifically, we used UKF to assimilate data from pairs of simultaneously impaled pyramidal cells and oriens-lacunosum moleculare (OLM) interneurons (INs) in the CA1 area of the hippocampus [23]. We then used biophysical ionic models to estimate extra- and intracellular potassium, sodium, and calcium ion concentrations and various parameters controlling their dynamics during seizures (Figure 4). In Figure 4A we show an intracellular recording from a pyramidal cell during seizures, and plot the estimated extracellular potassium concentration ($[K]_o$) in Figure 4B. As is clear from the figure the extracellular potassium concentration oscillates as the cell goes into and out of seizures. The potassium concentration begins to rise as the cell enters seizures and peaks with the maximal firing frequency, followed by decreasing potassium concentration as the firing rate decreases and the seizure terminates. Higher $[K]_o$ makes the PC more excitable by raising the reversal potential for $K^+$ currents (equation 7). The increased $K^+$ reversal potential causes the cell to burst-fire spontaneously. Whether the increased $[K]_o$ causes the cells to seize or $[K]_o$ is the result of seizures has been an old question [31] whose resolution will likely take place from better understanding of the coupled $K^+$ dynamics. For present purposes, it is known that increased $[K]_o$ in experiments can support the generation, and increase the frequency and propagation velocity of seizures [32,33]. Changes in the concentration of intracellular sodium ions, $[Na]_i$, are closely coupled with the changes of $[K]_o$ (Figure 4C). As shown in panels (4D–F) we reconstructed the parameters controlling the microenvironment of the cell. These parameters included the diffusion constant of $K^+$ in the extracellular space, $K^+$ buffering strength of glia, and $K^+$ concentration in the reservoir of the perfusing solution *in vitro* (or in the vasculature *in vivo*) during seizures. Note that the ionic concentration in the distant reservoir is different from the more rapid dynamics within the smaller connecting extracellular space near single cell where excitability is determined. We were also able

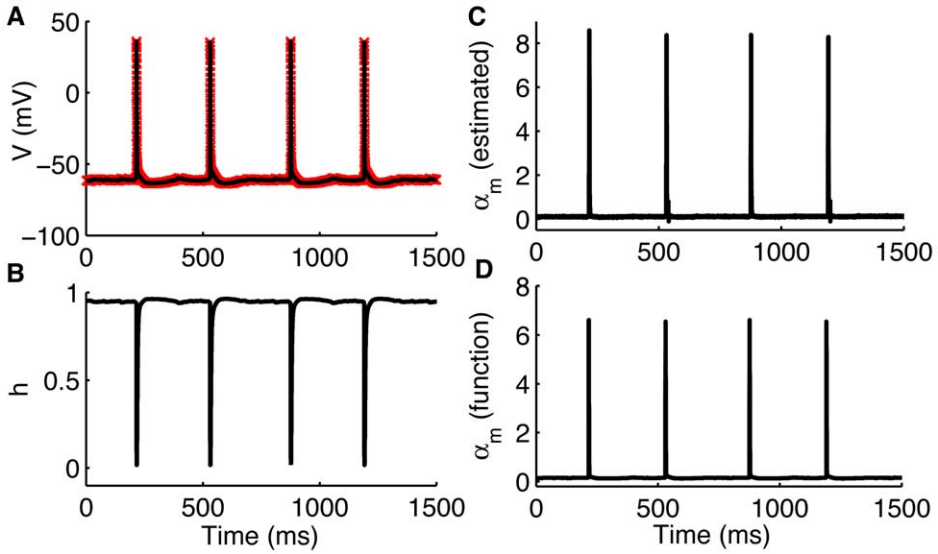


**Figure 3. Robust neuronal dynamics tracking in the face of moderate degree of model inaccuracy.** (A) measured (red), and estimated (black) voltage, $V$, using crippled model where the critical voltage-dependent sodium rate constant, $\alpha_m$, is replaced by a constant. The filter is still able to successfully estimate the gating variables (only $h$ shown in (B)). $\alpha_m$ tracked as a parameter is shown in (C), while the actual functional form of $\alpha_m$ is shown in (D). Spiking in the experimentally observed cell is generated by injecting a constant current of 100 picoampere. By itself, this model cannot spike. Fused with data and allowing the parameter $\alpha_m$ to float, it tracks $\alpha_m$ within 25% of its proper value. Data provided by Jokubas Ziburkus.
doi:10.1371/journal.pcbi.1000776.g003

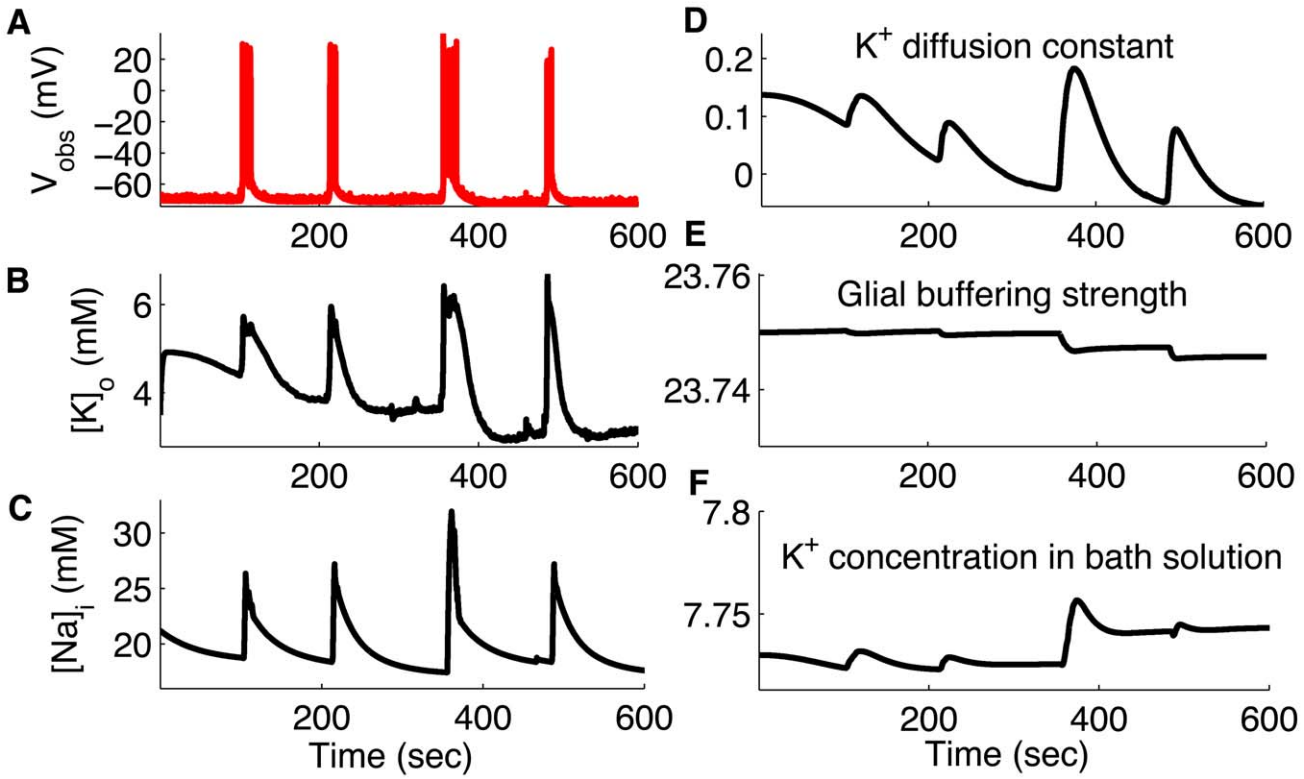


**Figure 4. Assimilating spontaneous seizure data by whole cell recording from CA1 hippocampal pyramidal neurons.** (A) Measured $V$ (red) from single PCs during spontaneous seizures. Estimated (black) $[K]_o$ (B), $[Na]_i$ (C), $K^+$ diffusion constant (D), glial buffering strength (E), and $K^+$ concentration in bath solution (F). Data provided by Jokubas Ziburkus. Panel (A) modified from [23] with permission American Physiological Society.
doi:10.1371/journal.pcbi.1000776.g004

to track other variables and parameters such as extracellular calcium concentration and ion channel conductances.

In Figure 5, we show an expanded view of a single cell response during a single seizure from Figure 4. Extracellular potassium concentration increases several fold above baseline values during seizures [31]. During a single seizure, $[K]_o$ starts rising from a baseline value of 3.0mM as the seizure begins and peaks at 7mM at the middle of the seizure (Figure 5). Interestingly the $[K]_o$ estimated by UKF matches very closely the measured $[K]_o$ seen *in vitro* studies [34].

Considering the slow time scale of seizure evolution (period of more than 100 seconds in our experiments), we test the importance of slow variables such as ion concentrations for seizure tracking. As shown in Figure 6, we found that including the dynamic intra- and extracellular ion concentrations in the model is necessary for accurate tracking of seizures. Using Hodgkin-Huxley type ionic currents with fixed intra- and extracellular ion concentration of $K^+$ and $Na^+$ ions fails to track seizure dynamics in pyramidal cells (Figure 6C). We used physiologically normal concentrations of 4mM and 18mM for extracellular $K^+$ and intracellular $Na^+$ respectively for these simulations. The conclusion remains the same when higher $[K]_o$ and $[Na]_i$ are used. A similar tracking failure is found while tracking the dynamics of OLM interneurons during seizures (not shown). To further emphasize the importance of ion concentrations dynamics for tracking seizures we calculate the Akaike's information criterion (AIC) for the two models used in Figure 6, i.e. the model with and without ion concentration dynamics. AIC is a measure of the goodness of fit of a model and offers a measure of the information lost when a given model is used to describe experimental observations. Loosely speaking, it describes the tradeoff between

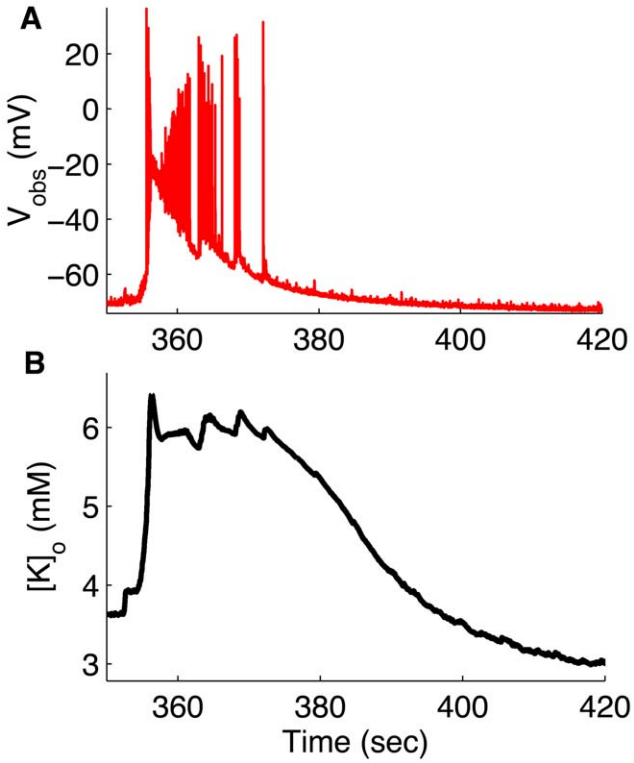


**Figure 5. Expanded view of third seizure in Figure 4 illustrating how $[K]_o$ changes during a seizure.** (A) membrane potential, $V$, (B) extracellular potassium concentration, $[K]_o$.
doi:10.1371/journal.pcbi.1000776.g005

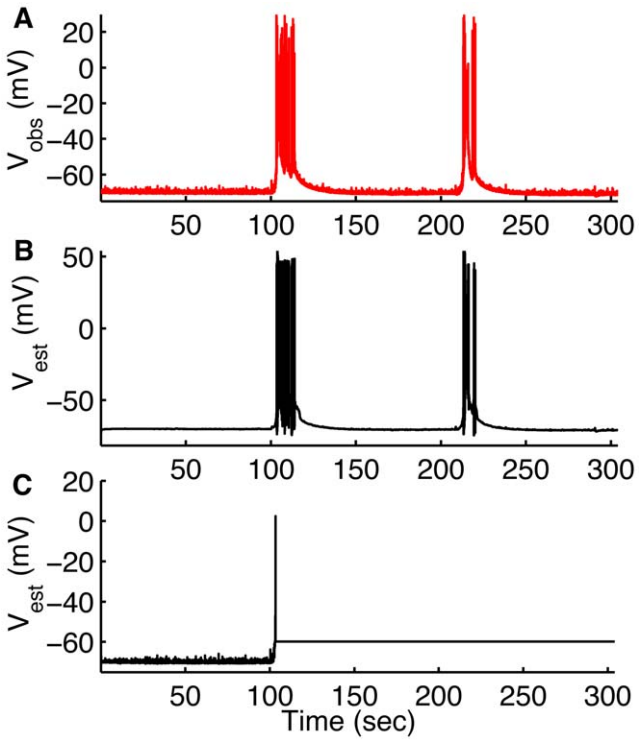


**Figure 6. UKF cannot track seizures without microenvironmental $K^+$ and $Na^+$ dynamics in the model.** Observed (A) and estimated (B) membrane potential using the model with ion concentrations dynamics. In (C) we show estimated membrane potential using the model without ion concentrations dynamics.
doi:10.1371/journal.pcbi.1000776.g006

precision and complexity of the model [35]. We used equation (29) for the AIC measure. The AIC measure for the model without ion concentration dynamics is $6.65 \times 10^5$. The model with ion concentration dynamics on the other hand has AIC value equal to $4.4765 \times 10^3$, indicating the importance of ion concentration dynamics for tracking seizures.

Pyramidal cells and interneurons in the hippocampus reside in different layers with different cell densities. To investigate whether there exist significant differences in the microenvironment surrounding these two cell types we assimilated membrane potential data from OLM interneurons in the hippocampus and reconstructed $K^+$ and $Na^+$ ion concentrations inside and outside the cells. As shown in Figure 7, both the baseline level and peak $[K]_o$ near the interneurons must be very high as compared to that seen for the pyramidal cells (cf. Figure 4B). This is an important prediction in light of the recently observed interplay between pyramidal cells and interneurons during *in vitro* seizures [23]; in these experiments pyramidal cells were silent when the interneurons were intensively firing. Following intense firing the interneurons entered a state of depolarization block simultaneously with the emergence of intense epileptiform firing in pyramidal cells. Such a novel pattern of interleaving neuronal activity is proposed to be a possible mechanism for the sudden drop in inhibition during seizures – it may be permissive of runaway excitatory activity. The mechanism leading to such interplay, specifically the reasons for differential firing patterns in pyramidal cells and interneurons are unknown. Our results here indicate the potential role of the neuronal microenvironment in producing such interplay. Our findings suggest that the $K^+$ buffering mechanism in the OLM layer is weaker as compared with the pyramidal layer, thus causing higher $[K]_o$ in the OLM layer. The higher $[K]_o$ surrounding the interneurons causes increased excitability of the cell by raising the reversal potential for $K^+$ currents (higher than the pyramidal cells, see equation 7). The higher reversal potential for $K^+$ currents causes the interneuron to spontaneously burst fire at higher frequency and eventually drives the interneuron to transition into depolarization block when firing is peaked. As the INs enter the depolarized state, the inhibitory synaptic input from the INs to the PCs drops substantially, releasing PCs to generate the intense excitatory

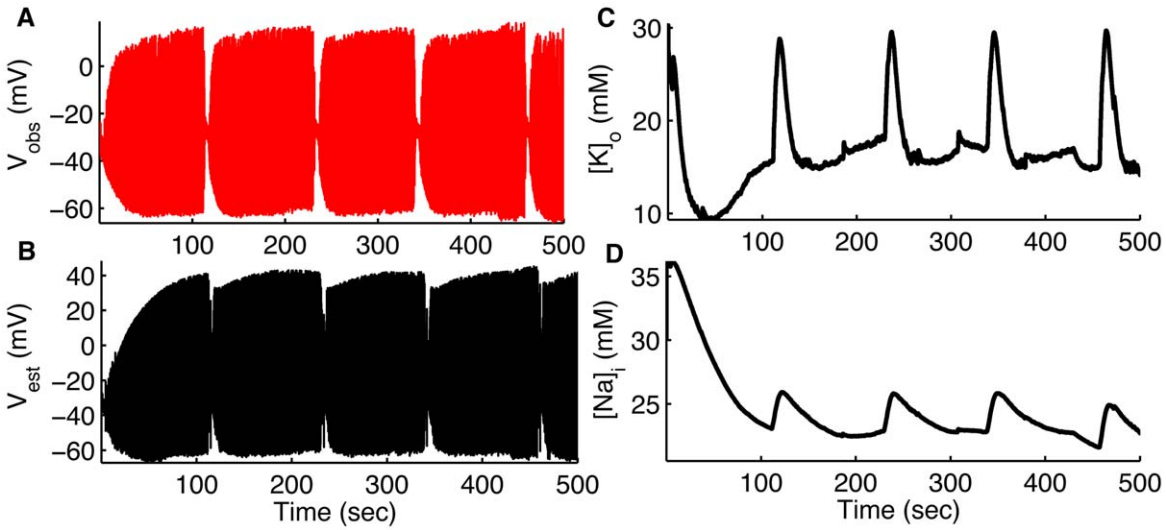


**Figure 7. Assimilating seizure data from CA1 hippocampal OLM interneurons.** Membrane potential measured (red) by whole cell recording from OLM interneurons during spontaneous seizures (A). In (B–D) we show membrane potential, $[K]_o$, and $[Na]_i$ of the same cell respectively estimated (black) by using UKF. As shown in Figure S1, we also tracked the remaining variables for IN. Data provided by Jokubas Ziburkus. Panel (A) modified from [23] with permission American Physiological Society.
doi:10.1371/journal.pcbi.1000776.g007

activity of seizures (equation 8, Figure S3). The collapse of inhibition due to the entrance of INs into a depolarized state also helps explain the sudden decrease in inhibition at seizure onset in neocortex described by Trevelyan, et al. [36] as the loss of *inhibitory veto*. As shown in Figure S1, we also tracked the remaining variables for the INs.

## Reconstructing Network Interaction

Since the interaction of neurons determines network patterns of activity, it is within such interactions that we seek unifying principles for epilepsy. To demonstrate that the UKF framework can be utilized to study cellular interactions, we reconstructed the dynamics of one cell type by assimilating the measured data from another cell type in the network. In Figure 8 we only show the estimated membrane potentials, but we also reconstructed the remaining variables and parameters of both cells (Figures S2 and S3). We first assimilated the membrane potential of the PC to estimate the dynamics of the same cell and also the dynamics of a coupled IN (Figure 8A–D). Conversely, we estimate the dynamics of PC from the simultaneously measured membrane potential measurements of the IN (Figure 8D–F). As is evident from Figure 8 the filter framework is successful at reciprocally reconstructing and tracking the dynamics of these different cells within this network. In Figure S2, we show intracellular $Ca^{2+}$ concentration and gating variables of $K^+$ and $Na^+$ channels in PCs for simulation in Figure 8A–D. The variables modeling the

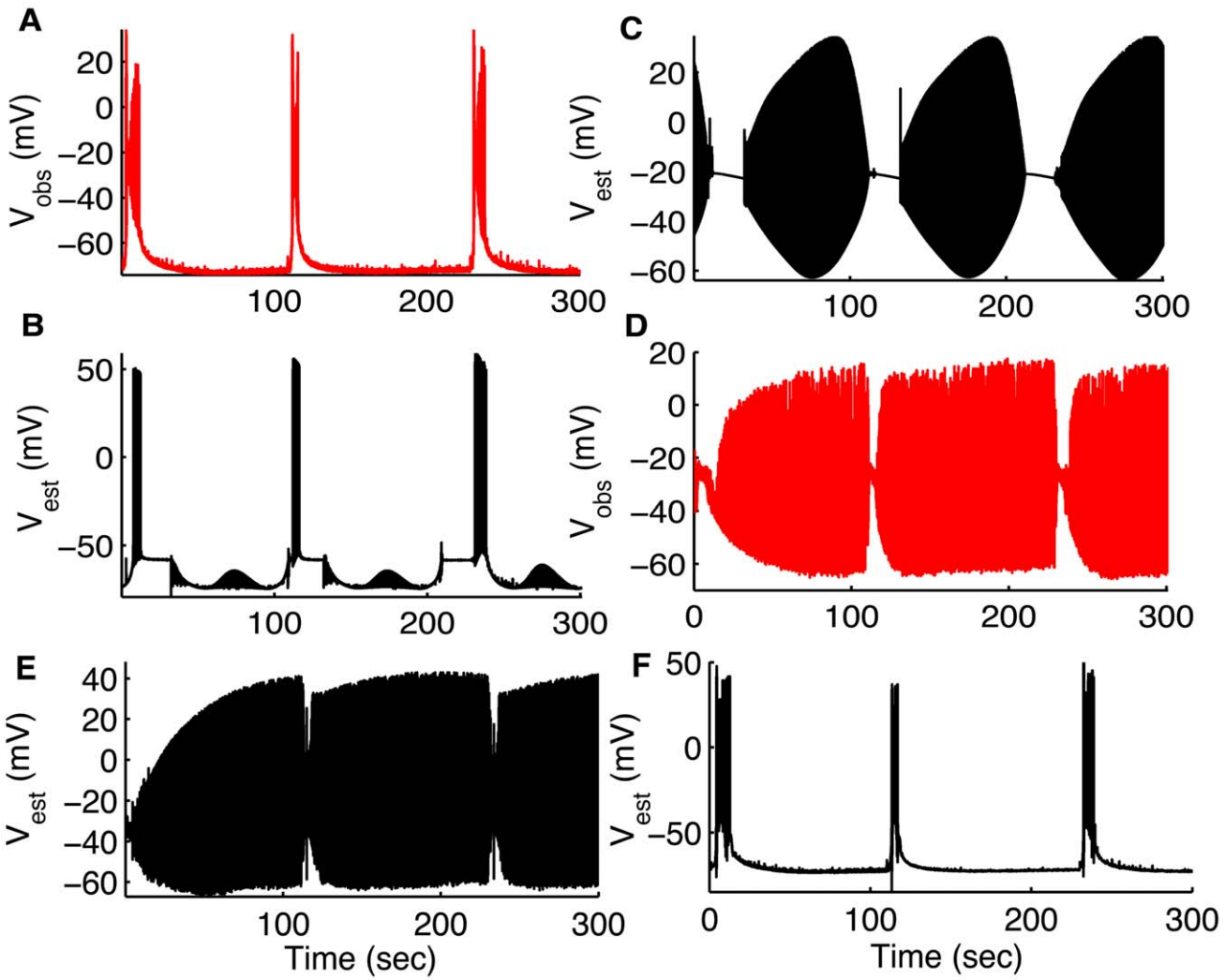


**Figure 8. Reconstructing network interaction.** Measured (A, red) and estimated (B, black) $V$ for pyramidal cell. (C) Estimated $V$ for interneuron. We used the membrane potential recorded from the pyramidal cell (shown in A, red) to not only reconstruct the full dynamics of the same pyramidal cell (only membrane potential shown in B, black) but also reconstructed the dynamics of the interneuron (only membrane potential shown in C, black). Simultaneously recorded $V$ from the IN is shown in (D, red) for comparison. Estimates for intracellular $Ca^{2+}$ concentration and gating variables $n$, $h$ for PC are shown in Figure S2 and the synaptic variables, $s$, $\eta$ are shown in Figure S3. Estimated $V$ for IN (E) and PC (F) by assimilating measured $V$ from IN (shown in (D)). (D–F) are converses of the simulations in (A–C). That is, In (D–F) we used membrane potential recorded from the interneuron (shown in D, red) to not only reconstruct the full dynamics of the same interneuron (only membrane potential shown in E, black) but also the coupled pyramidal cell (only membrane potential shown in F, black: compare with actual values shown in A, red). Simultaneous membrane potential measurements shown in (A,D) were from a pyramidal cell and OLM interneuron in the hippocampus using simultaneous dual whole cell patch clamp recordings demonstrating the firing interplay between these cells during *in vitro* seizures. Data provided by Jokubas Ziburkus. Panels (A,D) are modified from [23] with permission © American Physiological Society.
doi:10.1371/journal.pcbi.1000776.g008

synaptic inputs for both INs and PCs in Figure 8A–D are shown in Figure S3. As clear from Figure S3 (D), the variable $\eta_i$ (equation 8) reaches very high values when the INs lock into depolarization block, shutting off the inhibitory inputs from INs to PCs.

## Discussion

There has been intense interest in the neuroscience communities in bringing control-theoretical tools to bear on neuronal encoding and decoding problems [37–45]. In all of this work, statistical models (continuous or point process) were fit to data recorded from neurons, and these empirical models incorporated into applications. Our use of control theoretic tools is very different. We built computational models from the physiological properties of neurons and their networks, as well as the properties of ion metabolism, *without data fitting*. Using these fundamental models of the physics of neuronal systems, we fuse these models with data – *data assimilation* – in a manner commonly applied in meteorology [1,46–50]. We are aware of a recent laboratory demonstration in fluid mechanics using a simplified model of fluid dynamics (Boussinesq equations) in a similar manner as we have performed here [51] (see also [14]). Other authors have also recently discussed the importance and power of going beyond statistical empirical models in neuronal systems, and simulations have begun to explore the feasibility of carrying this out [52–54]. To our knowledge, our findings are the first experimental validation that a fundamental biophysical model of part of the brain can be employed to assimilate incomplete data and accurately reconstruct its network dynamics.

Our conjecture is that the parallels with numerical meteorology are deep. By the turn of the 20th century, it was apparent that the lack of periodicities in weather limited forecasts based on previous state (autoregressive) statistical models, and that integrating the actual equations of motion of the atmosphere would be required. Infeasible initially, the turning point came when integrating such models gave 'first approximations that bore a recognizable resemblance to the actual motions' [55]. Furthermore, the use of simplified dynamical models that retained the most important of the physical dynamics was a critical development [1].

Our findings suggest that an analogous use of biophysical models of neuronal processes using the recursive predictive strategies employed in meteorological data assimilation is now feasible. We are presently exploring such application in frameworks for model-based data assimilation and control of Parkinson's disease [15]. Experiments are underway exploring the application for seizures in the intact brain, and the assimilation of cognitive rhythms. The potential for such techniques to improve our understanding of the dynamics of single cells and neuronal networks is substantial.

### Conclusion

In conclusion, we have demonstrated the feasibility for data assimilation within neuronal networks using detailed biophysical models. In particular, we demonstrated that estimating the neuronal microenvironment and neuronal interactions can be performed by embedding our improving biophysical neuronal models within a model based state estimation framework. This approach can provide a more complete understanding of otherwise incompletely observed neuronal dynamics during normal and pathological brain function.

## Materials and Methods

### Model

We used two-compartmental models for the pyramidal cells and interneurons: a cellular compartment and the surrounding extracellular microenvironment. The membrane potentials of both cells were modeled by Hodgkin-Huxley equations containing sodium, potassium, calcium-gated potassium (after-hyperpolarization), and leak currents. For the network model, the two cell types are coupled synaptically and through diffusion of potassium ions in the extracellular space. A schematic of the model is shown in Figure 9.

**Membrane potential dynamics.** The membrane potential $V$ of the neurons is modeled with the following set of modified Hodgkin-Huxley equations [10,56]

$$\begin{aligned} C\frac{dV}{dt} &= I_{Na}+I_K+I_{AHP}+I_L,\\ I_{Na} &= -g_{Na}m^3h(V-V_{Na}),\\ I_K &= -g_K n^4(V-V_K),\\ I_{AHP} &= -g_{AHP}\left(\frac{[Ca]_i}{1+[Ca]_i}\right)(V-V_K),\\ I_L &= -g_{KL}(V-V_K)-g_{NaL}(V-V_{Na})-g_{ClL}(V-V_{Cl}),\\ dq/dt &= \alpha_q(1-q)-\beta_q q, q=m,n,h. \end{aligned} \tag{1}$$

where $n^4$ and $m^3h$ represent gating variables for potassium, $I_K$, and sodium, $I_{Na}$, currents. The leak current, $I_L$, has three components: $K^+$ leak, $I_{KL}$, $Na^+$ leak, $I_{NaL}$, and chloride leak, $I_{ClL}$. The after-hyperpolarization current $I_{AHP}$ is only included in the pyramidal cell to account for its frequency adaptation. The meaning and values of parameters used in the model are given in Table 1.

The rate equations for the gating variables are

$$\begin{aligned} \alpha_m &= \frac{0.1(V+30)}{1-exp(-0.1(V+30))}\\ \beta_m &= 4exp\left(-\frac{V+55}{18}\right)\\ \alpha_n &= \frac{0.01(V+34)}{1-exp(-0.1(V+34))}\\ \beta_n &= 0.125exp\left(-\frac{V+44}{80}\right)\\ \alpha_h &= 0.07exp\left(-\frac{V+44}{20}\right)\\ \beta_h &= \frac{1}{1+exp(-0.1(V+14))} \end{aligned} \tag{2}$$

**Ion concentrations dynamics.** The current equations were augmented with dynamic variables representing the intra- and extracellular ion concentrations ($K^+$, $Na^+$, and $Ca^{2+}$). These ion concentrations are affected by the neuron's intrinsic ionic currents as well as a sodium-potassium pump current. The glial buffering, diffusion between the nearest neighbor cells, and diffusion into the environment of the cell (bath solution in slice preparation and vasculature *in vivo*) also modulate the potassium concentration in the microenvironmental extracellular space. The ion concentrations inside and outside the cell are coupled to the

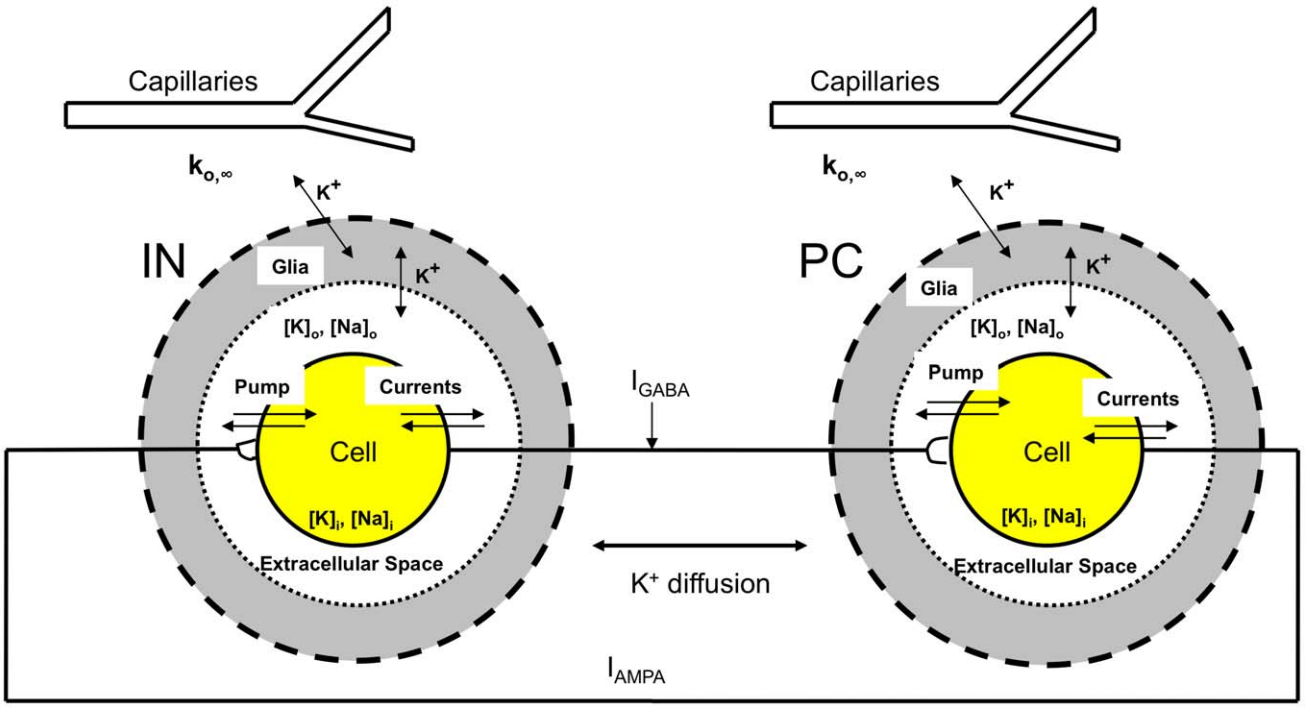


**Figure 9. A schematic of the model dynamics.** Potassium is released to the extracellular space and is pumped back to the cell by the ATP-dependent $K^+-Na^+$ exchange pump, buffered by glia, and diffuses to the microenvironment where it interacts with capillaries. Sodium entering the cell through $Na^+$ channels is pumped out of the cell by the ATP-dependent pump. Pyramidal cell (PC) and interneuron (IN) from the CA1 region of the hippocampus are coupled both synaptically and through lateral $K^+$ diffusion. Symbols used are defined in the text.
doi:10.1371/journal.pcbi.1000776.g009

**Table 1.** Model Parameters.

| Parameter | Value | Description |
|---|---|---|
| $C$ | $1\mathrm{m}F/cm^2$ | Membrane capacitance |
| $g_{Na}$ | $100mS/cm^2$ | Conductance of Sodium Current |
| $g_K$ | $30mS/cm^2$ | Conductance of potassium current |
| $g_{AHP}$ | $0.01mS/cm^2$ | Conductance of afterhyperpolarization current |
| $g_{KL}$ | $0.05mS/cm^2$ | Conductance of potassium leak current |
| $g_{NaL}$ | $0.0175mS/cm^2$ | Conductance of sodium leak current |
| $g_{ClL}$ | $0.05mS/cm^2$ | Conductance of chloride leak current |
| $\phi$ | $3sec^{-1}$ | Time constant of gating variables |
| $g_{Ca}$ | $0.1mS/cm^2$ | Conductance of calcium current |
| $V_{Ca}$ | 120mV | Reversal potential of calcium |
| $\beta$ | 7.0 | Ratio of intracellular to extracellular volume of the cell |
| $I_{max}$ | 1.125mM/sec | Maximum pump strength |
| $G_{glia}$ | 36mM/sec | Maximum strength of glial uptake |
| $\kappa$ | $0.8sec^{-1}$ | Diffusion constant of extracellular $K^+$ |
| $[Cl]_o$ | 6.0mM | Extracellular chloride concentration |
| $[Cl]_i$ | 130.0mM | Intracellular chloride concentration |

Values and description of various parameters used in the model. All other parameters that are not given here are described in the "Materials and Methods" section.
doi:10.1371/journal.pcbi.1000776.t001

membrane voltage equations via the Nernst equation [10,13,25]. Finally, PCs and INs are connected to each other through synaptic inputs and diffusion of extracellular potassium between the nearest neighbor neurons.

Given the potassium ion currents $I_k = I_K + I_{AHP} + I_{KL}$, activity of the pump exchanging $K^+$ and $Na^+$, $I_{pump}$, diffusion of potassium to the microenvironment, $I_{diff}$, and glial buffering, $I_{glia}$, the extracellular potassium dynamics, $[K]_o$, can be represented in the model as (Figure 9).

$$\begin{aligned}
&\frac{d[K]_o}{dt} = 0.3I_k - 2\beta I_{pump} - I_{diff} - I_{glia},\\
&I_{pump} = I_{max}\left(\frac{1}{1+exp((25-[Na]_i)/3)}\right)\left(\frac{1}{1+exp(8-[K]_o)}\right),\\
&I_{diff} = \kappa([K]_o - k_{o,\infty}),\\
&I_{glia} = \frac{G_{glia}}{1+exp((18-[K]_o)/2.5)}
\end{aligned} \tag{3}$$

where the $Na^+-K^+$ pump is modeled as a product of a sigmoidal functions, $I_{max}$ is the pump strength under normal conditions, and $[Na]_i$ is the intracellular sodium concentration. Each sigmoidal term saturates for high values of internal sodium and external potassium respectively. More biophysically realistic models of pumps, such as those in [57] produce substantially similar results. $k_{o,\infty}$ in the diffusion equation is the potassium concentration in the nearby reservoir. Physiologically, this would correspond to either the bath solution in a slice preparation, or the vasculature in the intact brain (noting that $[K]_o$ is kept below the plasma level by trans-endothelial transport). Both active and passive $K^+$ uptake into glia is incorporated into a simplified single sigmoidal response

function that depends on extracellular $K^+$ concentration with $G_{glia}$ representing the maximum buffering strength. A similar but more physiological approach was used in [58]. Two factors allow the glia to provide a nearly insatiable buffer for the extracellular space. The first is the large size of the glial network. Second, the glial endfeet surround the pericapillary space, which, through interaction with arteriole walls, can effect blood flow; this in turn can increase the buffering capability of the glia [59–61].

We consider a spherical cell with a radius of $7\mu m$. The diffusion coefficient of $[K]_o$ to the nearby reservoir $\kappa$, is obtained from Fick's law, $\kappa = 2D/\Delta x^2$, where $D = 250 \times 10^{-6} cm^2/\text{sec}$ is the $K^+$ diffusion constant in neocortex [62], and $\Delta x \approx 25\mu m$ for brain reflects the average distance between capillaries [63]. The factor $0.3\text{mM}\cdot cm^2/\mu\text{coul}$ in equation (3) converts ionic current to concentration rate of change and is calculated using $\beta A/FV$ [10], where $A$, $V$ and $F$ represent cell area, volume and Faraday constant respectively. $k_{o,\infty}$ is equal to 3mM in physiological conditions, and the intra- to extracellular volume ratio $\beta = 7$ [64].

To complete the description of $K^+$ dynamics, we make the assumption that the flow of $Na^+$ into the cell is compensated by flow of $K^+$ out of the cell to maintain bulk electroneutrality. Thus the internal potassium concentration ($[K]_i$) can be approximated by [10]

$$[K]_i = 140\text{m}M + (18\text{m}M - [Na]_i) \tag{4}$$

where 140mM and 18mM respectively are the normal resting concentrations of $K^+$ and $Na^+$ inside the cell.

The intracellular and extracellular $Na^+$ concentrations ($[Na]_i$, $[Na]_o$) are also updated in the model as [10]

$$\begin{aligned} \frac{d[Na]_i}{dt} &= 0.3\frac{I_{Na}}{\beta} - 3I_{pump}, \\ [Na]_o &= 144\text{m}M - \beta([Na]_i - 18\text{m}M) \end{aligned} \tag{5}$$

where 144mM is the normal resting extracellular $Na^+$ concentration. $I_{pump}$ in equations (3) and (5) are multiplied by factor 2 and 3 respectively due to the fact that the $K^+ - Na^+$ pump has an electrogenic 2:3 ratio.

The intracellular $Ca^{2+}$ concentration, $[Ca]_i$, is modeled with the following rate equation [65]

$$\frac{d[Ca]_i}{dt} = -\left(\frac{0.002 g_{Ca}(V - V_{Ca})}{1 + exp(-(V+25)/2.5)}\right) - [Ca]_i/80. \tag{6}$$

The reversal potentials for $K^+$, $Na^+$ and $Cl^-$ are updated based on the instantaneous ion concentrations using the Nernst equations

$$\begin{aligned} V_k &= 26.64\ ln\left(\frac{[K]_o}{[K]_i}\right), \\ V_{Na} &= 26.64\ ln\left(\frac{[Na]_o}{[Na]_i}\right), \\ V_{Cl} &= 26.64\ ln\left(\frac{[Cl]_i}{[Cl]_o}\right). \end{aligned} \tag{7}$$

Equation (7) binds the ion concentrations dynamics to the Hodgkin-Huxley equations (1, 2).

**Coupled cells model.** The pyramidal cells and OLM interneurons are coupled both synaptically and through extracellular $K^+$ diffusion as shown in Figure 9. The following synaptic currents are added to the membrane potential equations [25]

$$\begin{aligned} I_{syn}^{p/i} &= -\alpha_{ip/pi} s_{i/p} \chi_{i/p} (V^{p/i} - V_{ip/pi}), \\ \chi_{p/i} &= exp(-\eta^{p/i}/v) \\ \frac{d\eta_{p/i}}{dt} &= \gamma_{p/i}(V^{p/i} - V_b) - \tilde{\gamma}\eta_{p/i} \\ \gamma_{p/i} &= \begin{cases} 0.4 & if\ -30 < V^{p/i} < -10 \\ 0 & otherwise \end{cases}. \end{aligned} \tag{8}$$

Where the superscripts $p$ and $i$ represent pyramidal cell and interneuron respectively. $V^p$ and $V^i$ is the membrane potential of the PCs and INs respectively. The variable $\chi$ takes into account the firing interplay between pyramidal cells and interneurons [25]. Ziburkus, et al. [23] observed during *in vitro* seizures that pyramidal cells were silent when the interneurons were burst firing, followed by high frequency firing in pyramidal cells when interneurons were locked into a depolarized state called depolarization block. The variable $\chi$ in equation (8) causes the synaptic input to drop to zero when the cells go to depolarization block. Various parameters used in equation (8) are: $V_{ip} = -80$, $V_{pi} = 0$, $V_b = -50$, $\tilde{\gamma} = 0.4$, and $v = 5.0$. Synaptic strengths $\alpha_{ip}$, $\alpha_{pi}$ are mimicked according to $GABA_A$ and AMPA inputs and values of 0.84 and 0.17, respectively, are used for the simulations. The variable $s_p$ gives the temporal evolution of the synaptic input from the pyramidal cell to the interneuron and $s_i$ is the synaptic input from the interneuron to the pyramidal cell. $s_p$ and $s_i$ evolve as

$$\begin{aligned} \tau_{p/i}\frac{ds_{p/i}}{dt} &= A\sigma(V^{p/i})(1 - s_{p/i}) - s_{p/i} \\ \sigma(V^{p/i}) &= \frac{1}{1 + exp(-(V^{p/i} + 20)/3)} \end{aligned} \tag{9}$$

The parameters $\tau_p = 4$ and $\tau_i = 8$ are the time constants for the excitatory and inhibitory synapses respectively and $A = 20$.

In the case of coupled pyramidal cells and interneurons, the rate equation for $[K]_o$ is updated by adding the following lateral diffusion term ($I_{lateral}$)

$$I_{lateral} = \begin{cases} \frac{D}{\Delta x_1^2}([K]_o^i - [K]_o^p) & for\ pyramidal\ cell \\ \frac{D}{\Delta x_1^2}([K]_o^p - [K]_o^i) & for\ interneuron \end{cases} \tag{10}$$

where $\Delta x_1 = 50\mu m$ is the separation between the interneurons and pyramidal cells.

## Unscented Kalman Filter

To estimate and track the dynamics of the neuronal networks, we applied a nonlinear ensemble version of the Kalman filter, the unscented Kalman filter (UKF) [8,9]. The UKF uses known nonlinear dynamical equations and observation functions along with noisy, partially observed data to continuously update a Gaussian approximation for the neuronal state and its uncertainty. At each integration step, perturbed system states that are consistent with the current state uncertainty, *sigma points*, are

chosen. The UKF consists of integrating the system from the *sigma points*, estimating mean state values, and then updating the covariance matrix that approximates the state uncertainty. The Kalman gain matrix updates the new most likely state of the system based on the estimated measurements and the actual partially measured state. The estimated states (filtered states) are used to estimate the experimentally inaccessible parameters and variables by synchronizing the model equations to the estimated states. To estimate the system parameters from data, we introduced the unknown parameters as extra state variables with trivial dynamics. The UKF with random initial conditions for the parameters will converge to an optimal set of parameters, or in the case of varying parameters, will track them along with the state variables [11–13].

Given a function $F(x,t)$ describing the dynamics of the system (equations 1–10 in our case), and an observation function $W(x,t)$ contaminated by uncertainty characterized in the covariance matrix $R$, for a $D$-dimensional state vector with mean $\bar{x}$ the UKF generates the $2D$ *sigma points* $\chi^{(1)}$, …, $\chi^{(2D)}$ so that their sample mean and sample covariance are $\bar{x}$ and $P^{xx}$. The *sigma points* are the $2D$ rows of the matrix

$$\chi^{(i)} = \bar{x} \pm (\sqrt{DP^{xx}})_i^T \tag{11}$$

The index $(i)$ on the left-hand side corresponds to the *ith* row taken from the matrix in the parenthesis on right-hand side. The square root sign denotes the matrix square root and $T$ indicates transpose of the matrix. Sigma points can be envisioned as sample points at the boundaries of a covariance ellipsoid. In what follows, superscript tilde $(\tilde{\cdot})$ represents the *a priori* values of variables and parameter, i.e. the values at a given time-step $k$ when observation up to time-step $k-1$ are available, while hat $(\hat{\cdot})$ represents the *a posteriori* quantities, i.e. the values at time-step $k$ when observations up to time-step $k$ are available.

Applying one step of the dynamics $F$ to the *sigma points* and calling the results $\tilde{X}^{(i)} = F(\chi^{(i)},t)$, and denoting the observations of the new states by $\tilde{Y}^{(i)} = W(\tilde{X}^{(i)},t)$, we define the means

$$\begin{aligned} \tilde{x} &= \frac{1}{2D}\sum_{i=1}^{2D} \tilde{X}^{(i)}, \\ \tilde{y} &= \frac{1}{2D}\sum_{i=1}^{2D} \tilde{Y}^{(i)}, \end{aligned} \tag{12}$$

where $\tilde{x}$ and $\tilde{y}$ are the *a priori* state and measurement estimates, respectively. Now define the *a priori* covariances

$$\begin{aligned} \tilde{P}^{xx} &= \frac{1}{2D}\sum_{i=1}^{2D} (\tilde{X}^{(i)} - \tilde{x})(\tilde{X}^{(i)} - \tilde{x})^T, \\ \tilde{P}^{xy} &= \frac{1}{2D}\sum_{i=1}^{2D} (\tilde{X}^{(i)} - \tilde{x})(\tilde{Y}^{(i)} - \tilde{y})^T, \\ \tilde{P}^{yy} &= \frac{1}{2D}\sum_{i=1}^{2D} (\tilde{Y}^{(i)} - \tilde{y})(\tilde{Y}^{(i)} - \tilde{y})^T, \end{aligned} \tag{13}$$

of the ensemble members. The Kalman filter estimates of the new state and uncertainty are given by the *a posteriori* quantities

$$\hat{x} = \tilde{x} + K(y - \tilde{y}) \tag{14}$$

and

$$\hat{P}^{xx} = \tilde{P}^{xx} - K\tilde{P}^{xy}, \tag{15}$$

where $K = \tilde{P}^{xy}(\tilde{P}^{yy})^{-1}$ is the Kalman gain matrix and $y$ is the actual observation [3,8,9,11–13]. Thus $\hat{x}$ and $\hat{P}^{xx}$ are the updated estimated state $x$ and covariance $P$ for the next step. The *a posteriori* estimate of the observation $\hat{y}$ is recovered by $\hat{y} = W(\hat{x})$. Thus by augmenting the observed state variables with unobserved state variables and system parameters, UKF can estimate and track both unobserved variables and system parameters.

**Implementation of the UKF.** In our simulations, the state $x$ is the $D = N + m$ dimensional vector consisting of the $N$ variable values (equations 1–10) describing the dynamics of neurons and the $m$ parameter values to be tracked. The one-step dynamics function $F(x)$ is the system of differential equations (equations 1–10). State vector $x$ for a single PC is given as

$$x = \begin{bmatrix} V \\ h \\ m \\ n \\ [K]_o \\ [Na]_i \\ [Ca]_i \\ parameter_1 \\ parameter_2 \\ \dots \\ \dots \\ parameter_m \end{bmatrix} \tag{16}$$

Where $parameter_1$, $parameter_2$, …. $parameter_m$ are the parameters that we want to track. For example, we tracked three parameters in Figure 4, replacing $parameter_1$, $parameter_2$, …. $parameter_m$ by $\kappa$, $G_{glia}$, and $k_{o,\infty}$ respectively in equation (16). For coupled PC and IN, the state vector $x$ included variables $V$, $h$, $m$, $n$, $[K]_o$, $[Na]_i$, and $[Ca]_i$ for IN along with four synaptic variables, $\eta_p$, $\eta_i$, $s_p$, and $s_i$ in order to represent the synaptic interactions between the two cells. The observation function $W(x,t)$ returned the first component of the vector $x$ (membrane potential, $V$) at given time t. We observed the membrane potential of the cell and treated the rest of the variables as unobserved. For most of our simulations we used an integration time-step dt = 0.01ms while the membrane potential of the neuron was measured each 0.1ms.

An iteration of the filter is performed in the following three steps (see [3,8,9] for more details).

*Initialization:* The filter is initialized as follows

$$\begin{aligned} \hat{x}_0 &= E(x_o) \\ \hat{P}_0^{xx} &= E[(x_0 - \hat{x}_0)(x_0 - \hat{x}_0)^T] \end{aligned} \tag{17}$$

where $x_0$ are the initial values of the state variables, and $E$ represent expectation.

*Prediction:* The following equations are used to propagate the state estimate and covariance from time-step (k−1) to k. First create a set of *sigma points* by applying equation (11) to system state equation (16)

$$\chi_{k-1}^{(i)} = \hat{x}_{k-1} \pm \left(\sqrt{D\hat{P}_{k-1}^{xx}}\right)_i^T,\ i = 1,2,3.....2D \quad (18)$$

The *sigma points* are transformed into vectors $\tilde{X}_k^{(i)}$ by using the nonlinear system of equations $F$ (1–10)

$$\tilde{X}_k^{(i)} = F(\chi_{k-1}^{(i)}, t_k) \quad (19)$$

The average of vectors $\tilde{X}_k^{(i)}$ gives the *a priori* state estimate at time $k$.

$$\tilde{x}_k = \frac{1}{2D}\sum_{i=1}^{2D} \tilde{X}_k^{(i)} \quad (20)$$

The *a priori* error covariance is given as

$$\tilde{P}_k^{xx} = \frac{1}{2D}\sum_{i=1}^{2D} (\tilde{X}_k^{(i)} - \tilde{x}_k)(\tilde{X}_k^{(i)} - \tilde{x}_k)^T + Q_{k-1} \quad (21)$$

where $Q_{k-1}$ represents the process noise.

*Measurement Update:* We implemented the measurement update as follows. Given the current guess for the mean, $\tilde{x}_k$, and covariance, $\tilde{P}_k^{xx}$ of $x_k$, we choose new sigma points

$$\chi_k^{(i)} = \tilde{x}_k \pm \left(\sqrt{D\tilde{P}_k^{xx}}\right)_i^T,\ i = 1,2,3.....2D \quad (22)$$

This step can be omitted by using the *sigma points* from equation (18) to enhance the computational efficiency at the cost of performance [3]. The observation function $W$ is used to transform the *sigma points* into predicted measurements, $\tilde{Y}_k^{(i)}$ vector.

$$\tilde{Y}_k^{(i)} = W(\chi_k^{(i)}, t_k) \quad (23)$$

The average of $\tilde{Y}_k^{(i)}$ is the predicted measurement at time-step $k$:

$$\tilde{y}_k = \frac{1}{2D}\sum_{i=1}^{2D} \tilde{Y}_k^{(i)} \quad (24)$$

Equations (23 and 24) are used to estimate the covariance of predicted measurement

$$\tilde{P}_k^{yy} = \frac{1}{2D}\sum_{i=1}^{2D} (\tilde{Y}_k^{(i)} - \tilde{y}_k)(\tilde{Y}_k^{(i)} - \tilde{y}_k)^T + R_k \quad (25)$$

where $R_k$ takes into account the measurement noise.

Next, we estimate the cross covariance between $\tilde{x}_k$ and $\tilde{y}_k$

$$\tilde{P}_k^{xy} = \frac{1}{2D}\sum_{i=1}^{2D} (\tilde{X}_k^{(i)} - \tilde{x}_k)(\tilde{Y}_k^{(i)} - \tilde{y}_k)^T \quad (26)$$

Finally, the measurement at the time-step $k$ is used to update the state vector and its covariance

$$\begin{aligned} \hat{x}_k &= \tilde{x}_k + K_k(y_k - \tilde{y}_k) \\ \hat{P}_k^{xx} &= \tilde{P}_k^{xx} - K_k\tilde{P}_k^{xy} \end{aligned} \quad (27)$$

where

$$K_k = \tilde{P}^{xy}(\tilde{P}^{yy})^{-1} \quad (28)$$

The *a posteriori* observation $\hat{y}_k$ is recovered by $\hat{y}_k = W(\hat{x}_k, t_k)$.

We calculate the AIC measure for the two models used in Figure 6 using the following equations [35]

$$\begin{aligned} AIC &= 2\zeta + N[ln(RSS/N)] \\ RSS &= \sum_{i=1}^{N} (y_i - \hat{x}_i)^2 \end{aligned} \quad (29)$$

Where $\zeta$ is the total number of parameters in the model, $N$ is the total number of data samples ($N = 150000$ for examples in Figure 6), and $RSS$ is the residual sum of squares. The model that includes ion concentration dynamics has four extra parameters, $\beta$, $I_{max}$, $\kappa$, and $G_{glia}$. Therefore, we take $\zeta = 0$ and 4 for the models without and with ion concentrations dynamics respectively.

All simulations were carried out using MATLAB on $2 \times 4$ multi-core Mac Pro computer. The MATLAB code for the results is archived at ModelDB (http://senselab.med.yale.edu/modeldb/default.asp) and can also be provided by the authors upon request.

## Supporting Information

**Figure S1** Estimates of remaining variables for the INs shown in Figure 7. (A) intracellular $Ca^{2+}$ concentration (arbitrary units), (B) $K^+$ channel gating variable, $n$, and (C) $Na^+$ channel gating variable, $h$.
Found at: doi:10.1371/journal.pcbi.1000776.s001 (0.40 MB TIF)

**Figure S2** Estimates of remaining variables for the PCs shown in Figure 8A, B. intracellular $Ca^{2+}$ concentration (arbitrary units) (A) and gating variables, $n$ (B), $h$ (C).
Found at: doi:10.1371/journal.pcbi.1000776.s002 (0.30 MB TIF)

**Figure S3** Estimates of synaptic variables for PCs and INs shown in Figure 8A–D. Synaptic variables, $s_p$ (A), $\eta_p$ (B), $s_i$ (C), and $\eta_i$ (D). As is clear from (D), $\eta_i$ reaches high values when the INs lock into depolarization block, causing $\chi_i$ to approach zero thus shutting off the synaptic inputs from INs to PCs. When not in depolarization block, such as when fast spiking, $\eta_i \rightarrow 0$ and $\chi_i \rightarrow 0$, not affecting synaptic currents.
Found at: doi:10.1371/journal.pcbi.1000776.s003 (0.21 MB TIF)

## Acknowledgments

We extend our heartfelt thanks to Jokubas Ziburkus for his constructive comments on the manuscript and generously providing us with access to the experimental data.

## Author Contributions

Conceived and designed the experiments: GU SJS. Performed the experiments: GU. Analyzed the data: GU. Wrote the paper: GU SJS.

## References

1. Kalnay E (2003) Atmospheric modeling, data assimilation, and predictability. Cambridge University Press, New York.
2. Kalman RE (1960) A new approach to linear filtering and prediction problems. Trans ASME J Basic Eng 82: 35–45.

3. Simon D (2006) Optimal state estimation Wiley-Interscience.
4. Baek SJ, Hunt BR, Kalnay E, Ott E, Szunyogh I (2006) Local ensemble Kalman filtering in the presence of model bias. Tellus A 58: 293–306.
5. Yang SC, Baker D, Li H, Cordes K, Huff M, et al. (2006) Data assimilation as synchronization of truth and model: Experiments with the three-variable Lorenz system. J Atmos Sci 63: 2340–2354.
6. Evensen G (1994) Sequential data assimilation with a nonlinear quasi-geostrophic model using monte carlo methods to forecast error statistics. J Geophys Res 99: 10143–10162.
7. Evensen G, van Leeuwen PJ (2000) An ensemble Kalman smoother for nonlinear dynamics. Mon Weather Rev 128: 1852–1867.
8. Julier SJ, Uhlmann JK (1997) A consistent, debiased method for converting between polar and cartesian coordinate systems. P SPIE 3068: 110–121.
9. Julier SJ, Uhlmann JK (1997) A new extension of the kalman filter to nonlinear systems. P SPIE 3068: 182–193.
10. Cressman Jr. JR, Ullah G, Ziburkus J, Schiff SJ, Barreto E (2009) The influence of sodium and potassium dynamics on excitability, seizures, and the stability of persistent states: I. Single neuron dynamics. J Comput Neurosci 26: 159–170.
11. Voss HU, Timmer J (2004) Nonlinear dynamics system identification from uncertain and indirect measurements. Int J Bifurcat Chaos 14: 1905–1933.
12. Schiff SJ, Sauer TD (2008) Kalman filter control of a model of spatiotemporal cortical dynamics. J Neur Eng 5: 1–8.
13. Ullah G, Schiff SJ (2009) Tracking and control of neuronal Hodgkin-Huxley dynamics. Phys Rev E 79: 040901.
14. Sauer TD, Schiff SJ (2009) Data assimilation for heterogeneous networks: The consensus set. Phys Rev E 79: 051909.
15. Schiff SJ (2010) Towards model-based control of parkinson's disease. Phil Trans Royal Soc A, in press.
16. Schiff SJ, Cressman Jr. JR, Barreto E (2008) Towards a dynamics of seizure mechanics. in Computational Neuroscience in Epilepsy (Academic Press), London: pp 496–514.
17. Lehnertz K, Mormann F, Osterhage H, Muller A, Prusseit J, et al. (2007) State-of-the-art of seizure prediction. J Clin Neurophysiol 24: 147–153.
18. Mormann F, Andrzejak RG, Elger CE, Lehnertz K (2007) Seizure prediction: the long and winding road. Brain 130: 314–333.
19. Mormann F, Kreuz T, Rieke C, Andrzejak RG, Kraskov A, et al. (2005) On the predictability of epileptic seizures. J Clin Neurophysiol 116: 569–587.
20. Shu Y, Hasenstaub A, McCormick DA (2003) Turning on and off recurrent balanced cortical activity. Nature 423: 288–293.
21. Chub N, Mentis GZ, O'Donovan MJ (2006) Chloride-sensitive MEQ fluorescence in chick embryo motoneurons following manipulations of chloride and during spontaneous network activity. J Neurophysiol 95: 323–330.
22. Huang X, Troy WC, Yang Q, Ma H, Laing CR, et al. (2004) Spiral waves in disinhibited mammalian neocortex. J Neurosci 24: 9897–9902.
23. Ziburkus J, Cressman Jr. JR, Barreto E, Schiff SJ (2006) Interneuron and pyramidal cell interplay during in vitro seizure-like events. J Neurophysiol 95: 3948–3954.
24. Schiff SJ, Sauer TD, Kumar R, Weinstein SL (2005) Neuronal spatiotemporal pattern discrimination: the dynamical evolution of seizures. Neuroimage 28: 1043–1055.
25. Ullah G, Cressman Jr. JR, Barreto E, Schiff SJ (2009) The influence of sodium and potassium dynamics on excitability, seizures, and the stability of persistent states: II. Network and glial dynamics. J Comput Neurosci 26: 171–183.
26. Bazhenov M, Timofeev I, Steriade M, Sejnowski TJ (2004) Slow state transitions of sustained neural oscillations by activity-dependent modulation of intrinsic excitability. J Neurophysiol 92: 1116–1132.
27. Frohlich F, Timofeev I, Sejnowski TJ, Bazhenov M (2008) Extracellular potassium dynamics and epileptogenesis. In: Computational Neuroscience in Epilepsy (Academic Press), London: pp 419–439.
28. Mitra P, Bokil H (2007) Observed brain dynamics. Oxford University Press, USA.
29. Toth Z, Peña M (2007) Data assimilation and numerical forecasting with imperfect models: The mapping paradigm. Physica D 230: 146–158.
30. Ullah G, Schiff SJ (2009) Models of epilepsy. Scholarpedia 4: 1409.
31. Somjen GG (2004) Ions in the brain: normal function, seizures, and stroke. Oxford University Press, USA.
32. Traynelis SF, Dingledine R (1988) Potassium-induced spontaneous electrographic seizures in the rat hippocampal slice. J Neurophysiol 59: 259–276.
33. Jensen MS, Yaari Y (1997) Role of intrinsic burst firing, potassium accumulation, and electrical coupling in the elevated potassium model of hippocampal epilepsy. J Neurophysiol 77: 1224–1233.
34. Bikson M, Hahn PJ, Fox JE, Jefferys JGR (2003) Depolarization block of neurons during maintenance of electrographic seizures. J Neurophysiol 90: 2402–2408.
35. Akaike H (1974) A new look at the statistical identification model. IEEE T Automat Contr 19: 716–723.
36. Trevelyan AJ, Sussillo D, Watson BO, Yuste R (2006) Modular propagation of epileptiform activity: Evidence for an inhibitory veto in neocortex. J Neurosci 26: 12447–12455.
37. Brown EN, Nguyen DP, Frank LM, Wilson MA, Solo V (2001) An analysis of neural receptive field plasticity by point process adaptive filtering. P Natl Acad Sci USA 98: 12261–12266.
38. Barbieri R, Wilson MA, Frank LM, Brown EN (2005) An analysis of hippocampal spatio-temporal representations using a Bayesian algorithm for neural spike train decoding. IEEE T Neur Sys Reh 13: 131–136.
39. Smith AC, Brown EN (2003) Estimating a state-space model from point process observations. Neural Comp 15: 965–991.
40. Srinivasan L, Brown EN (2007) A state-space framework for movement control to dynamic goals through brain-driven interfaces. IEEE T Bio-med Eng 54: 526–535.
41. Srinivasan L, Eden UT, Mitter SK, Brown EN (2007) General-purpose filter design for neural prosthetic devices. J Neurophysiol 98: 2456–2475.
42. Smith AC, Wirth S, Suzuki WA, Brown EN (2007) Bayesian analysis of interleaved learning and response bias in behavioral experiments. J Neurophysiol 97: 2516–2524.
43. Wu W, Gao Y, Bienenstock E, Donoghue JP, Black MJ (2006) Bayesian population decoding of motor cortical activity using a Kalman filter. Neural Comp 18: 80–118.
44. Ergun A, Barbieri R, Eden UT, Wilson MA, Brown EN (2007) Construction of point process adaptive filter algorithms for neural systems using sequential Monte Carlo methods. IEEE T Bio-med Eng 54: 419–428.
45. Li Z, O'Doherty JE, Hanson TL, Lebedev MA, Henriquez CS, et al. (2009) Unscented Kalman Filter for Brain-Machine Interfaces. PLoS One 4: e6243.
46. Hunt BR, Kostelich EJ, Szunyogh I (2007) Efficient data assimilation for spatiotemporal chaos: a local ensemble transform Kalman filter. Physica D 230: 112–126.
47. Ott E, Hunt BR, Szunyogh I, Zimin AV, Kostelich EJ, et al. (2004) Estimating the state of large spatio-temporally chaotic systems. Phys Lett A 330: 365–370.
48. Baek SJ, Hunt BR, Kalnay E, Ott E, Szunyogh I (2006) Local ensemble Kalman filtering in the presence of model bias. Tellus A 58: 293–306.
49. Spiller ET, Budhiraja A, Ide K, Jones CKRT (2008) Modified particle filter methods for assimilating Lagrangian data into a point-vortex model. Physica D 237: 1498–1506.
50. Salman H, Kuznetsov L, Jones C, Ide K (2006) A method for assimilating lagrangian data into a shallow-water-equation ocean model. Mon Weather Rev 134: 1081–1101.
51. Cornick M, Hunt BR, Ott E, Kurtuldu H, Schatz MF (2009) State and parameter estimation of spatiotemporally chaotic systems illustrated by an application to Rayleigh–Bénard convection. Chaos 19: 013108.
52. Paninski L, Ahmadian Y, Ferreira DG, Koyama S, Rahnama Rad K, et al. (2009) A new look at state-space models for neural data. J Comput Neurosci. pp 1–20.
53. Huys QJM, Paninski L (2009) Smoothing of, and parameter estimation from, noisy biophysical recordings. PLoS Comput Biol 5: e1000379.
54. Deng B, Wang J, Che Y (2009) A combined method to estimate parameters of neuron from a heavily noise-corrupted time series of active potential. Chaos 19: 015105.
55. Charney JG (1951) Dynamic forecasting by numerical process. in Compendium of Meteorology, American Meteorological Society, Boston: pp 470–482.
56. Hodgkin AL, Huxely A (1952) A quantitative description of membrane current and its application to conduction and excitation in nerve. J Physiol 117: 500–544.
57. Lauger P (1991) Electrogenic ion pumps. Distinguished lecture series of the Society of General Physiologists, Vol 5, Sinauer Associates Inc MA, USA.
58. Kager H, Wadman WJ, Somjen GG (2007) Seizure-like afterdischarges simulated in a model neuron. J Comput Neurosci 22: 105–128.
59. Paulson OB, Newman EA (1987) Does the release of potassium from astrocyte endfeet regulate cerebral blood flow? Science 237: 896–898.
60. Kuschinsky W, Wahl M, Bosse O, Thurau K (1972) The dependency of the pial arterial and arteriolar resistance on the perivascular h+ and k+ conconcentrations. a micropuncture study. Eur Neurol 6: 92–95.
61. McCulloch J, Edvinsson L, Watt P (1982) Comparison of the effects of potassium and ph on the calibre of cerebral veins and arteries. Pflugers Arch 393: 95–98.
62. Fisher RS, Pedley TA, Prince DA (1976) Kinetics of potassium movement in norman cortex. Brain Res 101: 223–237.
63. Scharrer E (1944) The blood vessels of the nervous tissue. Quart Rev Biol 19: 308–318.
64. McBain CJ, Traynelis SF, Dingledine R (1990) Regional variation of extracellular space in the hippocampus. Science 249: 674–677.
65. Gutkin BS, Laing CR, Colby CL, Chow CC, Ermentrout GB (2001) Turning on and off with excitation: the role of spike-timing asynchrony and synchrony in sustained neural activity. J Comput Neurosci 11: 121–134.

J Comput Neurosci
DOI 10.1007/s10827-008-0130-6

# The influence of sodium and potassium dynamics on excitability, seizures, and the stability of persistent states: II. Network and glial dynamics

**Ghanim Ullah · John R. Cressman Jr. · Ernest Barreto · Steven J. Schiff**

Received: 20 June 2008 / Revised: 17 October 2008 / Accepted: 24 November 2008


**Abstract** In these companion papers, we study how the interrelated dynamics of sodium and potassium affect the excitability of neurons, the occurrence of seizures, and the stability of persistent states of activity. We seek to study these dynamics with respect to the following compartments: neurons, glia, and extracellular space. We are particularly interested in the slower time-scale dynamics that determine overall excitability, and set the stage for transient episodes of persistent oscillations, working memory, or seizures. In this second of two companion papers, we present an ionic current network model composed of populations of Hodgkin–Huxley type excitatory and inhibitory neurons embedded within extracellular space and glia, in order to investigate the role of micro-environmental ionic dynamics on the stability of persistent activity. We show that these networks reproduce seizure-like activity if glial cells fail to maintain the proper micro-environmental conditions surrounding neurons, and produce several experimentally testable predictions. Our work suggests that the stability of persistent states to perturbation is set by glial activity, and that how the response to such perturbations decays or grows may be a critical factor in a variety of disparate transient phenomena such as working memory, burst firing in neonatal brain or spinal cord, up states, seizures, and cortical oscillations.

**Keywords** Neuronal networks · Instability · Glia buffering · Seizures · Persistent activity

**Action Editor: Alain Destexhe**

G. Ullah (✉) · S. J. Schiff
Center for Neural Engineering,
Department of Engineering Science and Mechanics,
The Pennsylvania State University,
212 Earth Engineering Science Building,
University Park, PA 16802, USA
e-mail: ghanim@psu.edu

J. R. Cressman Jr. · E. Barreto
Department of Physics and Astronomy,
The Center for Neural Dynamics,
and The Krasnow Institute for Advanced Study,
George Mason University,
Fairfax, VA 22030, USA

S. J. Schiff
Departments of Neurosurgery and Physics,
The Pennsylvania State University,
University Park, PA 16802, USA

## 1 Introduction

Despite an extraordinary amount of interest in understanding the dynamics of seizures, we still lack a unifying dynamical definition of what a seizure is (Soltesz and Staley 2008). The extraordinary variety of experimental preparations and human epilepsies makes the quest for unifying principles especially difficult.

In the first of these two companion papers, we examined the role of potassium dynamics on the stability of the activity of a single neuron (Cressman et al. 2009). In this second of two papers, we apply our findings to the stability of networks of neurons. We undertake our study using the concept of "persistent states" of activity as a paradigm for our investigation. Increasing evidence points to the importance of persistent activity in the maintenance of mental state and working memory (Miller et al. 2003; Wang 2003). The maintenance of neural activity over time following an event has been observed experimentally in monkey prefrontal cortex during short-term working memory, i.e., delay periods of tasks that require the animals to remember certain features

Published online: 13 December 2008

such as target location (Funahashi et al. 1989; Fuster 1995; Goldman-Rakic 1995; Miller et al. 1996; Rainer et al. 1998; Romo et al. 1999). The brain requires a certain degree of instability to form such an activity balance (often likened to a Turing instability (Murray 2003)). We here ask: what are the network properties that render such physiological persistent states stable to perturbations? and especially: what are the circumstances where such perturbations lead to seizure-like activity?

Synaptic interaction is in many systems the driver of persistent excitation. Neurons within a network may sustain activity by circulating activity among themselves, thus bypassing individual neurons' refractory periods. Such persistent network activity often requires a balance between inhibitory and excitatory activity (McCormick et al. 2003; Shu et al. 2003; Van Vreeswijk and Sompolinsky 1996). When inhibition is strong compared to excitation, the network responds to strong stimuli, but negative feedback suppresses the network such that the activity of all neurons decays with time. In intermediate conditions, where the excitation is balanced by inhibition, the network can exhibit a stable focus of activity (see for example Durstewitz et al. 2000; Vogels et al. 2005). This mode can be utilized in different kinds of information processing, for example to sustain a representation of spatial information for a period of time (Funahashi et al. 1989). When the network is dominated by excitation, the activity of all neurons can increase to a relatively high firing rate, and information processing by the network is impaired. For example, blocking $GABA_A$-receptor mediated inhibition can result in the transformation of recurrent persistent activity into intense epileptiform activity (Sanchez-Vives and McCormick 2000).

In most models of pathological conditions such as seizures, a shift from dominant (or balanced) inhibition to dominant excitation in a neuronal network is considered to be responsible for the network transition from the pre-ictal to ictal state (Trevelyan et al. 2006). In such conditions of imbalance between inhibition and excitation, moderate perturbations can drive a neuronal network from physiological to seizure-like activity. However, the conditions under which such network transitions occur in response to perturbations are not well known.

We hypothesize that perturbing an active neuronal network will reveal a dynamical signature of functional stability. We draw this analogy from the physics of equilibrium systems (Forster 1990). We suggest that such perturbation responses are an operational test of excitatory-inhibitory neuronal balance in neuronal networks.

We focus on the role that the extracellular space and glia may play in modulating the stability of these persistent states. Glial cells absorb excess ions, most importantly $K^+$, from the extracellular space and thus regulate excessive excitation due to decreased neuronal transmembrane $K^+$ gradients. Glia also release neurotransmitters such as glutamate, which can cause excitation in the surrounding neurons through the activation of NMDA receptors (Parpura et al. 1994; Parpura and Haydon 2000; Tian et al. 2005). However, a characterization of how glial dysfunction affects the dynamics of neuronal network activity remains largely unstudied. For example, what would happen if the glial cells fail to adequately remove the excess $K^+$ ions from the interstitial volume or if they suddenly release excessive glutamate while the network is performing normally?

In recent work, there is gathering evidence characterizing the interplay between excitatory and inhibitory neurons during seizures (Fujiwara-Tsukamoto et al. 2004; Perez-Velazquez and Carlen 1999). Ziburkus et al. (2006) observed interplay between pyramidal cells (PCs) and interneurons (INs) during *in vitro* seizure-like events. In particular, PCs were seen go into a silent state when INs were burst firing, followed by burst firing in PCs when INs went to depolarization block. What might be the underlying network dynamics that can lead to such seizure patterns?

In this second of two companion papers we address these questions through mathematical modeling. We construct a physiologically-motivated model for the neuronal network that combines the Hodgkin-Huxley formalism for the neuronal ionic currents with a model for the dynamics of the extra- and intracellular $K^+$ concentrations ([K]) and includes glia and active ion pumps. We also include dynamic extra- and intracellular $Na^+$ concentration ([Na]). We show that this model is able to maintain localized, persistent activity when the glial network is functioning normally and excitation and inhibition are balanced. The model is then used to explore physiological conditions under which an otherwise normal network would show abnormal activity. We show that such networks reproduce seizure-like activity if glial cells fail to maintain the proper extracellular [K]. Our model builds upon the findings of a simplified single cell ionic micro-environmental model in the accompanying manuscript (Cressman et al. 2009).

## 2 Methods

A schematic of our model network is shown in Fig. 1.

### 2.1 Membrane potential dynamics

We used single-compartment neurons in a network consisting of 100 PCs and 100 INs. The equations

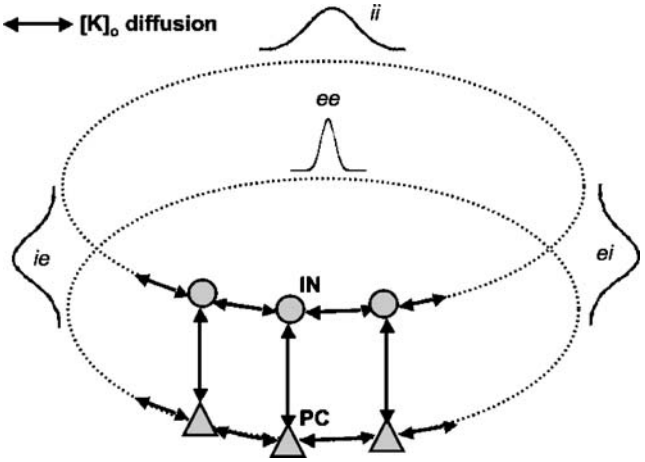


**Fig. 1** Topology of the network. The network consists of one pyramidal cell layer and one interneuron layer, both arranged in a ring (*dotted lines*). The two neuronal types make synaptic connections in the same layer as well as across the layers with Gaussian synaptic footprints (represented by Gaussian curves, where *ee*, *ei*, *ie*, and *ii* stand for excitatory–excitatory, excitatory–inhibitory, inhibitory–excitatory, and inhibitory–inhibitory synaptic connections respectively). The narrower *ee* Gaussian curve indicates that excitatory neurons make more spatially localized synaptic connections to other excitatory neurons (see "Methods" section). The $K^+$ concentration around each neuron diffuses to the nearest neighbors in the same layer and the nearest neighbor in the next layer (represented by *solid lines* with *double arrows*)

governing the membrane potential of the PCs and INs are adopted from the model in (Gutkin et al. 2001), and are as follows.

$$\begin{aligned} C\frac{dV^{e/i}}{dt} &= I_{Na}^{e/i} + I_K^{e/i} + I_L^{e/i} + I_{syn}^{e/i} + I_{ext}^{e/i} + I_{rand}^{e/i} \\ I_{Na}^{e/i} &= -g_{Na}\left[m_\infty^{e/i}\left(V^{e/i}\right)\right]^3 h^{e/i}\left(V^{e/i} - V_{Na}^{e/i}\right) \\ I_K^{e/i} &= -\left(g_K\left[n^{e/i}\right]^4 + \frac{g_{AHP}[Ca]_i^{e/i}}{1+[Ca]_i^{e/i}}\right)\left(V^{e/i} - V_K^{e/i}\right), \end{aligned} \tag{1}$$

where the superscript *e*/*i* refers to PC/IN (excitatory–inhibitory) cells in the network. Both intrinsic and synaptic $\left(I_{syn}^{e/i}\right)$ currents are incorporated into the model neurons. The gating variables for the intrinsic currents are described in the companion paper (Cressman et al. 2009). The leak current used here is lumped and is given as

$$I_L^{e/i} = -g_L\left(V^{e/i} - V_L^{e/i}\right). \tag{2}$$

The slow calcium-activated $K^+$ current (the spike-frequency adapting or afterhyperpolarization current, $g_{AHP}$) is only included in the PCs, i.e. $g_{AHP}$=0 mS/cm$^2$ for INs. The various parameters and variables used in this paper are defined in Table 1.

In order to take into account the Ziburkus et al. (2006) findings of PC–IN interplay during seizure-like events, we modify the synaptic current entering the *j*th PC and IN from that used in (Gutkin et al. 2001). We use

$$\begin{aligned} I_{syn}^e &= -\frac{\left(V_j^e - V_{ee}\right)}{N}\sum_{k=1}^{N} g_{jk}^{ee} s_k^e \chi_{jk}^e - \frac{\left(V_j^e - V_{ie}\right)}{N}\sum_{k=1}^{N} g_{jk}^{ie} s_k^i \chi_{jk}^i, \\ I_{syn}^i &= -\frac{\left(V_j^i - V_{ei}\right)}{N}\sum_{k=1}^{N} g_{jk}^{ei} s_k^e \chi_{jk}^e - \frac{\left(V_j^i - V_{ii}\right)}{N}\sum_{k=1}^{N} g_{jk}^{ii} s_k^i \chi_{jk}^i, \end{aligned} \tag{3}$$

where $V_j^{e/i}$ is the voltage of the jth excitatory–inhibitory neuron, $s_k^{e/i}$ is the variable giving the temporal evolution of the synaptic efficacy emanating from the *k*th excitatory–inhibitory neuron, and $\chi_{jk}^{e/i}$ takes into account the interplay between PCs and INs described above; that is, if a cell goes into depolarization block, then the synaptic inputs from that cell to others are reduced towards zero by the factor $\chi_{jk}^{e/i}$.

**Table 1** Model variables and parameters

| | Description |
|---|---|
| Variable | |
| $V$ | Membrane potential |
| $I_K$ | Potassium current |
| $I_{Na}$ | Sodium current |
| $I_L$ | Leak current |
| $I_{syn}$ | Synaptic current |
| $I_{ext}$ | Stimulus current |
| $I_{rand}$ | Random background noise |
| $s$ | Variable giving the temporal evolution of synapse |
| $V_L$ | Reversal potential of leak current |
| $I_{pump}$ | Pump current |
| $I_{glia}$ | Glial uptake |
| $[K]_o$ | Extracellular potassium concentration |
| $[K]_i$ | Intracellular potassium concentration |
| $g^{ij}$ | Spatial extent of synaptic current from *i*th to *j*th neuron |
| $\chi$ | Variable modeling the depolarization block |
| $\eta$ | Threshold to synaptic block due to the depolarization |
| $[Na]_o$ | Extracellular sodium concentration |
| $[Na]_i$ | Intracellular sodium concentration |
| Parameter | |
| $C$ | Membrane capacitance |
| $I_{amp}$ | Stimulus amplitude |
| $\tau$ | Time constant of synapses |
| $g_L$ | Conductance of leak current |
| $g_{AHP}$ | Conductance of afterhyperpolarization current |
| $k_{o,\infty}$ | Steady state extracellular potassium concentration |
| $G_{glia}$ | Strength of glial uptake |
| $\alpha_{ij}$ | Strength of synaptic current from *i*th to *j*th neuron |
| $\varepsilon$ | Constant for potassium diffusion to bath solution |
| $\gamma$ | Forward rate constant into and out of synaptic block due to depolarization |
| $\widetilde{\gamma}$ | Backward rate constant into and out of synaptic block due to depolarization |
| $D$ | Diffusion coefficient of potassium |
| $[Cl]_o$ | Extracellular chloride concentration |
| $[Cl]_i$ | Intracellular chloride concentration |

$V_{ee}$,$V_{ei}$,$V_{ie}$, and $V_{ii}$ are the reversal potentials for the excitatory–excitatory, excitatory–inhibitory, inhibitory–excitatory, and inhibitory–inhibitory synaptic inputs, respectively. The subscripts $ij$ in all equations in this paper represent the connection from cell $i$ to cell $j$. The variables used in Eqs. (1)–(3) are given as

$$\begin{aligned}
\tau^{e/i}\frac{ds^{e/i}}{dt} &= \phi\sigma\left(V^{e/i}\right)\left(1-s^{e/i}\right)-s^{e/i}\\
\sigma(V^{e/i}) &= 1/\left[1+\exp\left(-\left(V^{e/i}+20\right)/4\right)\right]\\
g_{jk}^{ee} &= \alpha_{ee}\sqrt{\tfrac{100}{\pi}}\exp\left(-100[(j-k)/N]^2\right)\\
g_{jk}^{ie} &= \alpha_{ie}\sqrt{\tfrac{30}{\pi}}\exp\left(-30[(j-k)/N]^2\right)\\
g_{jk}^{ei/ii} &= \alpha_{ei/ii}\sqrt{\tfrac{30}{\pi}}\exp\left(-30[(j-k)/N]^2\right)\\
\chi_{jk}^{e/i} &= \begin{cases}\exp\left(-\eta^{e/i}/\upsilon\right) & \text{if} \quad \eta^{e/i}>5.0\\ 1 & \text{otherwise}\end{cases}\\
\frac{d\eta^{e/i}}{dt} &= \gamma^{e/i}\left(V^{e/i}-V_b\right)-\widetilde{\gamma}\eta^{e/i}\\
\gamma^{e/i} &= \begin{cases}0.4 & \text{if} \quad -30<V^{e/i}<-10\\ 0 & \text{otherwise}\end{cases}.
\end{aligned} \tag{4}$$

The parameter values used in Eqs. (1)–(4) are $\phi$=3, $\tau^{e}$= 4 ms, $\tau^{i}$=8 ms, $g_L$=0.05 mS/cm$^2$, $V_{ee}$=0 mV, $V_{ie}$=−80 mV, $\alpha_{ie}$=0.06, $V_b$=-50.0 mV, $\widetilde{\gamma}=0.4$, $\upsilon$=5.0, $V_{ei}$=0 mV, and $V_{ii}$=−80 mV. The factors −100, −30, and −30 inside the exponential terms in the expressions for $g_{jk}^{ee}$, $g_{jk}^{ie}$, and $g_{jk}^{ei/ii}$, respectively, model the different spatial ranges of synaptic inputs made by the PCs and INs; thus, the PC-to-PC connections have a narrow spatial footprint, while the PC–IN and the IN–IN synaptic footprints are wider. $\chi_{jk}^{e/i}$ models the synaptic block due to depolarization, $\upsilon$ is an associated scale, $V^{e/i} \in [-30, -10]$, and $\eta^{e/i}>5$ is the threshold to synaptic block due to depolarization.

Random currents $\left(I_{rand}^{e,i}\right)$ are chosen from a uniform distribution over [−10, 10], where both negative and positive pulses have equal arrival probability. A constant external current $I_{ext}^{i}=0.5$ is injected into the INs. For simulations in this paper (unless otherwise mentioned), a spatially restricted stimulus of Gaussian form $I_{ext}^{e}=I_{amp}\exp\left(-60[(j-N/2)/N]^2\right)$ was injected into PCs 21–79 at $t$=112 ms for 20 ms to induce the stable focus of activity, where $N$=100, $j$ is neuron number and $I_{amp}$=1.5 (see also Gutkin et al. 2001). A value of $\alpha_{ii}$=0.02 is used in all simulations.

## 2.2 Ion concentrations dynamics

The model also contains dynamic extra- and intracellular [K] and [Na], subject to the constraints in Cressman et al. (2009); see also Eqs. (8) and (9) below. The [K] in the interstitial volume surrounding each cell ($[K]_o$) was continuously updated based on $K^+$ currents across the neuronal membrane, $Na^+$–$K^+$ pumps, uptake by the glial network surrounding the neurons, and lateral diffusion of $K^+$ within the extracellular space. The $[K]_o$ dynamics is modeled by the following differential equation, which is modified from that in (Cressman et al. 2009) because of the network structure:

$$\begin{aligned}
\frac{d[K]_o^{e/i}}{dt} &= 0.33I_K^{e/i}-2\beta I_{pump}^{e/i}-I_{diff}^{e/i}-I_{glia}^{e/i}+\frac{D}{\Delta x^2}\\
&\times\left([K]_{o(+)}^{e/i}+[K]_{o(-)}^{e/i}+[K]_o^{i/e}-3[K]_o^{e/i}\right).
\end{aligned} \tag{5}$$

The factor $\beta$=7.0 corrects for the volume fraction between the interior of the cell and the extracellular space when calculating the concentration change and is based on (Mazel et al. 1998; McBain et al. 1990; Somjen 2004). $[K]_{o(+)}^{e/i}$ and $[K]_{o(-)}^{e/i}$ are the $K^+$ concentrations in the adjacent extracellular volumes corresponding to nearest neighbors in the same layer, $[K]_o^{i/e}$ is the $K^+$ concentration around the nearest neighbor in the second layer and mimics the $K^+$ diffusion across the layers, and $D$=2.5×10$^{-6}$ cm$^2$/s is the diffusion coefficient for $K^+$ in water (Fisher et al. 1976). The factor 0.33 mM cm$^2$/μC in front of $I_K^{e/i}$ is used to convert the currents into ion concentration rate-of-change, and 2.0 in front of $\beta I_{pump}$ is due to the fact that the $Na^+$-$K^+$ pump has an electrogenic 2:3 ratio. Further discussion of $\beta$ and the 0.33 can be found in Appendix A from the companion paper Cressman et al. (2009).

The model also includes terms that replicate the effects of active pumps and diffusion through the surrounding glial network (Cressman et al. 2009). For pumps, we use

$$\begin{aligned}
I_{pump}^{e/i} &= \left(\frac{1.25}{1.0+\exp\left(\left(25.0-[Na]_i^{e/i}\right)/3.0\right)}\right)\\
&\times\left(\frac{1.0}{1.0+\exp\left(8.0-[K]_o^{e/i}\right)}\right).
\end{aligned} \tag{6}$$

The $K^+$ diffusion between the extracellular space and the bath solution is modeled by

$$I_{diff}^{e/i}=\varepsilon\left([K]_o^{e/i}-k_{o,\infty}\right),$$

and the glial uptake is modeled by

$$I_{glia}^{e/i}=-\frac{G_{glia}}{1.0+\exp\left(\left(18-[K]_o^{e/i}\right)/2.5\right)}, \tag{7}$$

where $k_{o,\infty}$ is the steady state $K^+$ concentration in the nearby reservoir—either the bath solution in a slice preparation, or the vasculature in the intact brain. Unless otherwise mentioned, a value of 1.3 s$^{-1}$ for $\varepsilon$ and 66.7 mM/s for $G_{glia}$ is used throughout this paper, where $G_{glia}$ is the glial buffering strength.

To complete the description of the $[K]$ dynamics, we make the assumption that the flow of $Na^+$ into the cell is compensated by flow of $K^+$ out of the cell. Then the internal [K] ($[K]_i$) can be approximated by

$$[K]_i^{e/i} = 140.0mM + \left(18.0mM - [Na]_i^{e/i}\right), \tag{8}$$

where 140.0 and 18.0 mM respectively are the normal resting concentrations of $K^+$ and $Na^+$ inside the cell.

The internal and external $Na^+$ concentrations ($[Na]_i$, $[Na]_o$) are also updated in the model as

$$\frac{d[Na]_i^{e/i}}{dt} = 0.33\frac{I_{Na}^{e/i}}{\beta} - 3I_{pump}^{e/i} \tag{9}$$
$$[Na]_o^{e/i} = 144.0mM - \beta\left([Na]_i^{e/i} - 18.0mM\right),$$

where 144.0 mM in Eq. (9) is the normal resting extracellular $Na^+$ concentration. Further details on $I_{pump}$, $I_{diff}$, $\varepsilon$, $G_{glia}$, $[K]_i$, $[Na]_i$, and $[Na]_o$ can be found in Cressman et al. (2009).

The reversal potential for the leak current used in Eq. (2) is updated based on the instantaneous ion concentrations inside and outside the cell using the Goldman–Hodgkin–Katz equation

$$V_L^{e/i} = 26.64\ln\left(\frac{[K]_o^{e/i}+0.065[Na]_o^{e/i}+0.6[Cl]_i^{e/i}}{[K]_i^{e/i}+0.065[Na]_i^{e/i}+0.6[Cl]_o^{e/i}}\right), \tag{10}$$

where $[Cl]_i^{e/i}$ and $[Cl]_o^{e/i}$ are the concentrations of intra- and extracellular chloride and are equal to 6.0 and 130 mM respectively.

### 2.3 Numerical integration

We integrated the model numerically using the fourth-order Runge–Kutta method with a time step of 0.01 ms. The spatial diffusion of $[K]_o$ was solved by the forward-difference method with a spatial grid $\Delta x$=10.0 μm; note also that the $K^+$ surrounding one cell (e.g. PC) can diffuse to the nearest neighbors in the same layer as well as the next layer (IN). Our results were robust to moderate changes in the ratio and number of PCs and INs. Code for our model is available from ModelDB.[1]

## 3 Results

### 3.1 Persistent states

To study instability in neuronal networks, we investigated a two-layer composite of one-dimensional networks consisting of 100 PCs and 100 INs (see Fig. 1). Both neuron types were modeled as single-compartment conductance-based cells using the Hodgkin-Huxley formalism (Gutkin et al. 2001). The spike-frequency adapting current was only included in the PCs, a common property of these cells (Mason and Larkman 1990; Wang 1998). In the network, both cell types were connected among themselves (PC–PC and IN–IN) and to each other (PC–IN) through spatially-dependent synaptic profiles, where the average PC–PC connections are smaller than the others (IN–IN, PC–IN). Importantly, our model incorporates dynamic intra- and extracellular ion concentrations, along with the effects of pumps, glia, and diffusion. The details of the network connectivity and ion concentration dynamics are described in the "Methods" section.

We followed the protocol of Gutkin et al. (2001) to induce persistent activity in the network by applying a spatially localized Gaussian excitatory stimulus at time $t$= 112 ms for 20 ms. In response, the neurons exhibit discharge spikes that activate the connected neurons, which in turn activate other neurons. For an appropriate choice of synaptic parameters, this positive feedback leads to a self-sustained and spatially-localized activity which outlasts the input stimulus, as shown in Fig. 2(a). As in Fig. 3 of Gutkin et al. (2001), we find that this occurs when there is an appropriate balance between excitation and inhibition.

To clarify this notion, we examined the consequences of varying the overall strength of the PC–PC and the PC–IN synaptic strengths. Figure 2(b) shows plots of the synaptic parameters $\alpha_{ee}$ versus $\alpha_{ei}$ for three different values of the bath potassium concentration $k_{o,\infty}$. The region between the dark curves corresponds to parameter sets for which self-sustained and spatially-contained network activity can be observed. With too much excitation (i.e., in the region above the top curve), the activity spreads throughout the network. With too much inhibition (i.e., below the bottom curve), the network shows only transient activity in response to the stimulus. In the region between the curves, the excitation and inhibition are sufficiently balanced such that the stimulus gives rise to activity that is persistent and spatially restricted, such as that shown in Fig. 2(a).

We observed that the stability region shifts towards smaller values of $\alpha_{ee}$ when $k_{o,\infty}$ is increased (note the different vertical scales in the three panels of Fig. 2(b)). Thus, the increase in $[K]_o$ due to $K^+$ diffusion from the bath must be counterbalanced by a decrease in excitatory synaptic strength to maintain stability. Note also that the width of the stability region decreases with increasing $k_{o,\infty}$; we observed a 25% decrease in width as $k_{o,\infty}$ increased from 3 to 3.5 mM (Fig. 2(b)). These results are consistent with Figs. 3 and 8 of Oberheim et al. (2008), in which it was observed that in the epileptic brain, the

[1] http://senselab.med.yale.edu/modeldb/

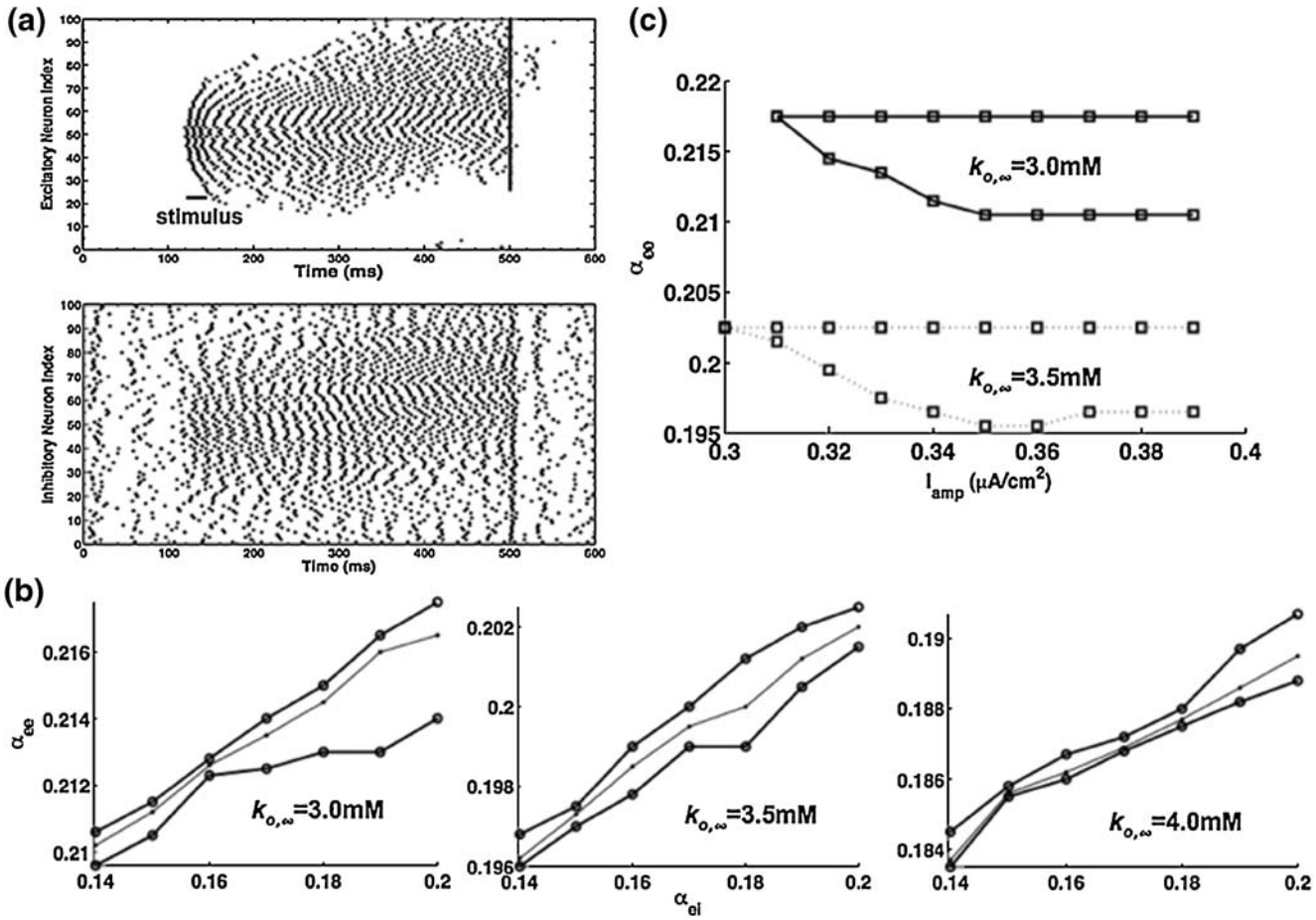


**Fig. 2** The existence and stability of spatially restricted foci of activity in our neuronal network. (**a**) A 20 ms excitatory Gaussian stimulus with amplitude $I_{amp}$=1.5 μA/cm$^2$ (see text) applied to PCs 21–79 causes a persistent and spatially restricted activity packet in the network. This activity is turned off by synchronizing neuronal activity using a strong 1 ms stimulus of 100 μA/cm$^2$ at $t$=500 ms. The *top* (*bottom*) *panel* shows a raster plot for the PC (IN) network where each *dot* represents a single-cell spike in the network. Here $\alpha_{ee}$=0.215, and $k_{o,\infty}$=3.0 mM. (**b**) The region for persistent and spatially restricted focus of activity using three different $k_{o,\infty}$ values. The focus is persistent, spatially restricted and is turned off by a strong synchronizing stimulus in the region enclosed by *two lines* (*thick solid lines* with *circles* for three $k_{o,\infty}$ values). Below this region the inhibition is stronger than excitation and the focus does not exist, while above this region the excitation is stronger as compared to inhibition and the activity spreads throughout the entire network. The $\alpha_{ee}$ values for a stable activity focus decreases as $k_{o,\infty}$ is increased ((**b**), *middle* and *right panels*) showing that for persistent states, the increase in $k_{o,\infty}$, must be balanced by a decrease in excitation (note the different ordinate scales). The *thin solid lines* with bullets inside all activity regions represent the upper bound of the activity regions that are stable against perturbations of fixed (moderate) size. i.e. if the network is between the lower bound of the activity region and the *thin line* with *bullets*, then the network is stable against moderate perturbations. Above the *thin line* in each region the network can show persistent and spatially restricted foci of activity but is not stable against moderate perturbations (although it is still stable against small perturbations). It is clear that the percentage of the activity region that is stable to perturbations decreases with increasing $k_{o,\infty}$. The existence of the focus also depends on the stimulus strength. The focus does not exist if the stimulus is too weak (**c**). After a certain threshold of the stimulus ($I_{amp}$=0.31 here) the weakness of the stimulus is compensated by the excitation strength and external potassium level. A value of $\alpha_{ei}$=0.2 is used for simulations in (**a**), (**c**)

density of spines and the volume of dendrites increases, which causes an increase in excitation. Meanwhile, the overlap of astrocytes and the increase in their volume enhances $[K]_o$ accumulation due to reduced extracellular space. This rearrangement reduces the glial network's capacity to buffer extracellular $K^+$ and contributes to increased glutamate release (Oberheim et al. 2008). The regions above the upper curves in Fig. 2(b) correspond to such a state.

We also investigated the stability of persistent activity by applying perturbing stimuli. Following Gutkin et al. (2001), we observed that persistent activity can be "turned off" by a strong excitatory stimulus (see Fig. 2(a) at $t$=500 ms). We then applied more moderate stimuli to persistent activity generated with networks within the stable regions of Fig. 2(b). The thin lines inside each stability region demarcate the upper bound of the region that is stable to moderate perturbations. More precisely, if the network is between the

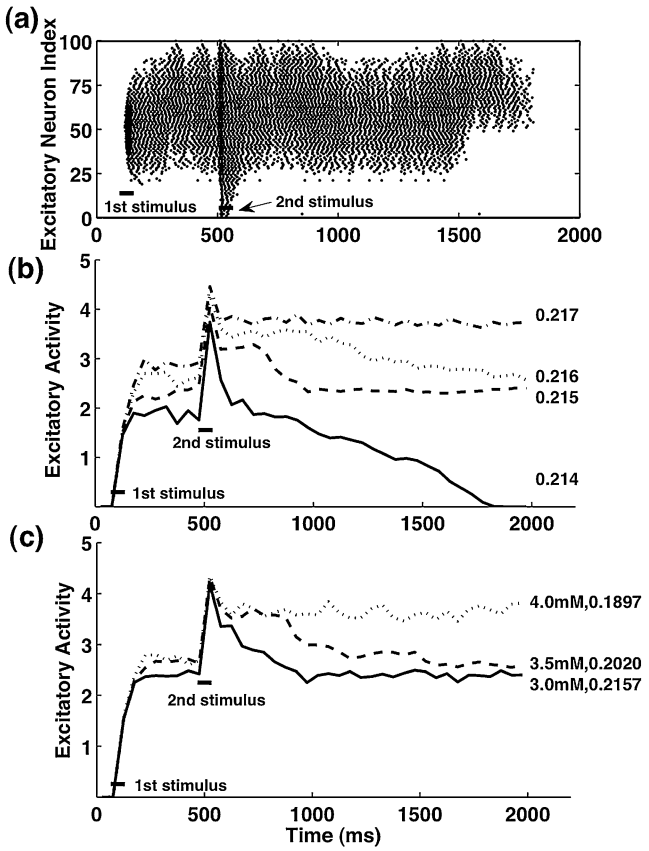


**Fig. 3** The activity (see text for definition) of the excitatory population for various $\alpha_{ee}$ values. The first stimulus (see text) at $t$= 112 ms for 20 ms causes a stable focus of activity in the network. A second stimulus of 1.0 μA/cm$^2$ at $t$=500 ms for 20 ms causes the focus to take over the entire population. After the stimulus is removed the network either decays to the zero-activity state, returns to the stable focus or remains in the state where activity is spread throughout the entire population depending on the excitation strength. In (**a**) we show a raster plot for a single simulation where the activity decays to zero after the perturbation. $\alpha_{ee}$=0.214 is used in this example. (**b**) Network activity for different $\alpha_{ee}$ values. The *numbers* on the *right* of each *line* are the $\alpha_{ee}$ values used during the simulations. (**c**) Same as (**b**) but here we use the different $k_{o,\infty}$ values given in the plot. The stability of the network also depends on the steady state $[K]_o$. For smaller extracellular $K^+$ the network activity decays back to the stable focus after the second stimulus is turned off. However, if $[K]_o$ is high the network maintains its enhanced activity even after the second stimulus vanishes. $\alpha_{ee}$ values are chosen such that they lie at the centers of the activity regions shown in Fig. 2(b) (*right column* in Fig. 3(c)). For all simulations in (**a**)–(**c**) $\alpha_{ei}$=0.2 is used. The *curves* in *panels* (**b**) and (**c**) are averaged over several trials

lower bound of the region and the thin line, then the network is stable to moderate perturbations (see also the discussion of Fig. 3(c) below). Analogous to the experimental results described above, our model shows that the network is less resistant to epileptic drive when already in a relatively excited state (contrast the three panels of Fig. 2(b)).

Persistent activity can only be initiated using a limited range of input current values (Fig. 2(c)). If $I_{amp}$ is too small, the combined effects of the stimulus and excitatory synaptic activity are not sufficient to cause a persistent state. Excessively high input current, $I_{amp}$ is also ineffective at producing long-lasting behavior, as it shuts down the network by synchronizing the activity of all the neurons (e.g. Fig. 2(a)). There is also an intermediate range of $I_{amp}$ values where the network activity spreads over all of the neurons. So in order of increasing stimulus strength, one can see the following four behaviors in the network (results not illustrated): (1) Transient behavior where the activity decays with time (below the lower range of the regions in Fig. 2(c)), (2) a stable focus of activity that lasts for several seconds (within the regions illustrated in Fig. 2(c)), (3) a state where the activity spreads throughout the network (above the upper range of the regions in Fig. 2(c)), and (4) a state with no activity where the current synchronizes and stops the activity of all neurons in the network (further to the right of the activity regions shown in Fig. 2(c)). We note that the experimental work of Pinto et al. (2005, Fig. 2 of this reference) is also consistent with these observations; in that study, a stimulus threshold for wave initiation and its dependence on inhibition and excitation was described.

### 3.2 Transition from persistent states to seizures

To examine the stability of persistent activity against perturbations, we plot the activity of the network for various values of $\alpha_{ee}$ using the same $k_{o,\infty}$=3.0 mM. We estimate the activity of the network by counting the number of spikes in the excitatory (PC) population that occur within 50 ms non-overlapping time windows, and calculating the average (spikes per millisecond). We take the value of $\alpha_{ee}$ such that it either lies at the boundary or within the region where we see a stable focus of activity (shown in Fig. 2(b), left panel). An initial excitatory stimulus (at $t$=112 ms for 20 ms) causes a stable focus of activity to appear. After some time, we apply a second stimulus (at $t$=500 ms for 20 ms) to all neurons in the network. The second stimulus is stronger than the first so that it can recruit all neurons in the network. As shown in Fig. 3(a),(b), we observe different behaviors depending on the value of $\alpha_{ee}$. Inhibition dominates at smaller $\alpha_{ee}$ (0.214) and the excitatory perturbation causes the network to decay to silence as demonstrated through the raster plot in Fig. 3(a). For $\alpha_{ee}$ values within (0.215–0.216), the network returns to the spatially restricted persistent activity that was present before the perturbation. However, for larger $\alpha_{ee}$ (0.217), the network fails to regain its stable focus of activity and all the cells in the network persistently fire action potentials (Fig. 3(b)). The stability of a network persistent state depends on the balance of excitatory and inhibitory synaptic strength of the network. Consistent with our

findings, Pinto et al. (2005) found that the permeability of cortical slices to epileptic wave initiation and spreading decreased by increasing 6,7-dinitroquinoxaline-2,3-dione (AMPA receptor antagonist). An opposite effect was observed by raising the picrotoxin ($GABA_A$ receptor antagonist) concentration (see for example Figs. 5 and 6 of Pinto et al. 2005).

As mentioned above, stability can be maintained after increasing $k_{o,\infty}$ by reducing the excitability in the network. Increasing $k_{o,\infty}$ leads to increases in the local potassium concentration $[K]_o$. In order to investigate how this effects stability, we repeated the simulations in Fig. 3(b) using three different values of $k_{o,\infty}$ (different $[K]_o$ values can also be achieved by varying the glial buffering strength $G_{glia}$, however, the results of these simulations remain unchanged). The values of $\alpha_{ee}$ are chosen such that they are always at the center of the three stability regions shown in Fig. 2(b). It is clear from Fig. 3(c) that for low $k_{o,\infty}$ values (3.0–3.5 mM), the activity of the network drops back to the level observed prior to the perturbation. However, the network is unable to regain its stable focus of activity after perturbation when $k_{o,\infty}$ is higher (4.0 mM). As mentioned earlier, the region of stability shrinks with increased $[K]_o$. At the same time the percentage of the activity region that is stable to perturbation also decreases with increasing $k_{o,\infty}$. In other words, for about 80% of the activity region for $k_{o,\infty}$=3.0 mM in Fig. 2(b) (from lower bound to the thin solid line with bullets), the network activity is stable to perturbations of moderate size. When $k_{o,\infty}$=3.5 mM and 4.0 mM, the network is stable only for about 50% and 30% (between thin solid line with bullets and lower bound) of the persistent activity regions respectively (see Fig. 2(b)). We note that in experimental work, an accelerated spread of epilepsy has been observed by elevating $K^+$ in the bath solution (Figs. 2 and 3 of Konnerth et al. 1984).

Recently, several groups have reported that the $Ca^{2+}$ dependent glutamate release from glial cells generates slow transient inward currents in nearby neurons through the activation of NMDA receptors (Parpura et al. 1994; Parpura and Haydon 2000). These discoveries of neuron-glia interaction have been extended by Tian et al. (2005) and Kang et al. (2005) to glial contributions to epilepsy. They showed that glial cells appear to be capable of synchronizing the activity of adjacent neurons through simultaneous non-synaptic slow inward neuronal currents. Another group has made a contrasting claim that glutamate released by glia is not necessary for the generation of epileptic activity in hippocampal slices (Fellin et al. 2006). We use our computational model to differentiate the conditions under which the glial-based perturbations would cause the neuronal network to go to a seizure-like state from that where the glial perturbations are insufficient for the network to make the transition from normal to seizure-like state.

In the framework of our model, the net effect of glutamate released by glial cells will manifest itself as an increased excitatory synaptic drive ($\alpha_{ee}$) in the network. To test the robustness of the network against glial induced excitability, we began our simulation with normal network activity as previously described. After establishing a stable focus of activity we increased the excitability of the network by increasing $\alpha_{ee}$ above the region of stable activity for 30 ms (i.e. we applied a second stimulus in $\alpha_{ee}$). The abrupt increase in $\alpha_{ee}$ thus mimics the effect of sudden glutamate release from glia. The activity of the network spread throughout the network but whether or not the persistent state could be reestablished depended on the baseline value of $\alpha_{ee}$. The network is stable to this perturbation for baseline values of $\alpha_{ee}$=0.215–0.216 (Fig. 4). However, the rate at which the network restored its stable focus of activity depends on the baseline $\alpha_{ee}$ value. If the baseline value of $\alpha_{ee}$ is too small (≤0.214), the transient $\alpha_{ee}$ increase destroys the persistent state. Similarly, for sufficiently large $\alpha_{ee}$ values the network was unable to restore its stable focus of activity and the analogue of epileptiform spread following perturbation is shown in the upper trace of Fig. 4 (analogous to Figs. 4 and 5 of Tian et al. (2005), where they observed epileptiform activity caused by increased excitation due to $Ca^{2+}$ dependent glutamate release by glia). This behavior also depends on the extracellular $K^+$ concentration. For higher $[K]_o$ ($[K]_o$≥4.0 mM) values the network cannot

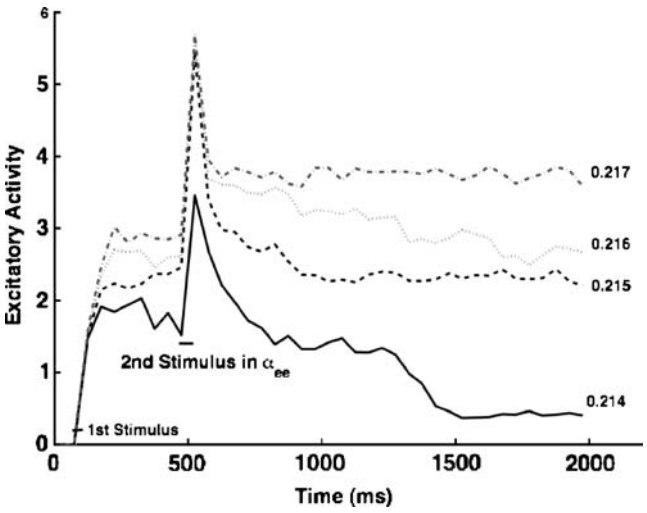


**Fig. 4** Same as Fig. 3(b),(c) but the second stimulus is in $\alpha_{ee}$, i.e. instead of applying current for the second stimulus the $\alpha_{ee}$ is increased beyond the stable activity region (see Fig. 2(b)) to a value of 0.25 for 30 ms at $t$=500 ms. After the $\alpha_{ee}$ value is restored the network returns to the stable focus of activity if the baseline $\alpha_{ee}$ is in an intermediate range. If the baseline $\alpha_{ee}$ is too large the network cannot return to the stable focus. Similarly if the baseline $\alpha_{ee}$ is too small the persistent state decays after the perturbation is removed. The baseline $\alpha_{ee}$ values are given in the plot and $\alpha_{ei}$=0.2

reestablish its stable activity when the excitability is increased and then restored (result not shown).

### 3.3 Spontaneous seizures in the network

Next we investigated the dynamics of the network as $[K]_o$ evolves in time. Since the $K^+$ dynamics is very slow we simulated the network for longer times. For the simulation in Fig. 5(a)–(c), $k_{o,\infty}$ is taken equal to 14.0 mM, which generates very slow oscillations in $[K]_o$ (see Cressman et al. 2009). In Fig. 5(a) we show the membrane potential for one PC in the network. Initially the cell is silent when $[K]_o$ is low (Fig. 5(b)). However, as $[K]_o$ rises, the cell starts seizure-like tonic firing. The firing frequency increases as $[K]_o$ increases, followed by depolarization block. The spiking returns when $[K]_o$ starts decreasing. The cell eventually goes to a silent state after $[K]_o$ has fallen below a certain value and the whole process repeats for the next cycle of $[K]_o$. The locking of the cells into depolarization block has been observed in experiments (Fig. 2 of Bikson et al. 2003; Fig. 2 of Ziburkus et al. 2006) and in simulation (Fig. 3 of Kager et al. 2007). This effect has been shown to quench synaptic transmission and could underlie the interplay seen between PC and IN during *in vitro* seizures if inhibition is differentially lost through depolarization block (Fig. 2 of Ziburkus et al. 2006). In Fig. 5(b) we show the traces for $[K]_o$ and $[Na]_i$, while the excitatory activity of the network is shown in Fig. 5(c). The activity drops to zero at higher $[K]_o$ values when the whole network transiently goes into

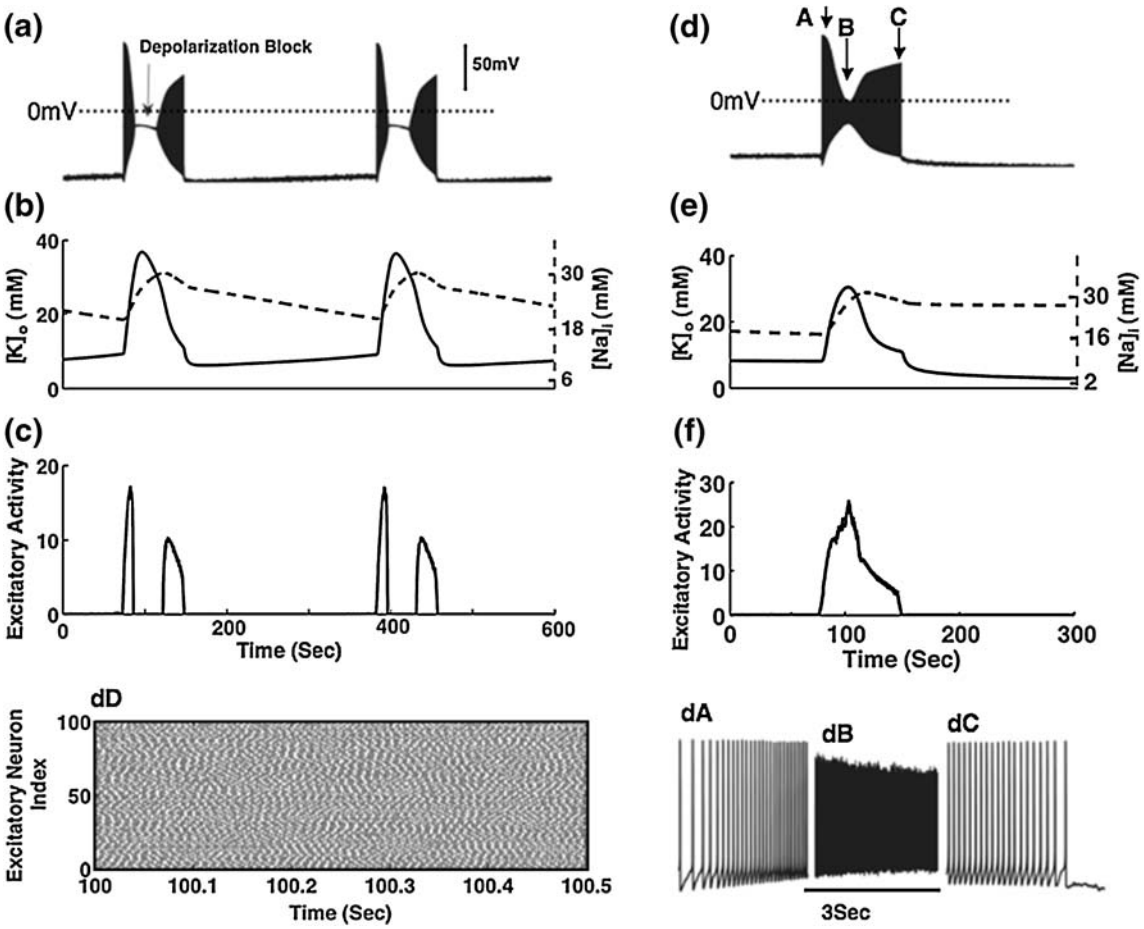


**Fig. 5** Spontaneous activity in the network for varying $[K]_o$. In panel (**a**) we show the membrane potential of one PC in the network as (**b**) $[K]_o$ (*solid line*) and $[Na]_i$ (*dashed line*) evolve in time. (**c**) shows the activity of the network, where the drop in activity occurs at high $[K]_o$ values due to the switching of the network to depolarization block. For (**a**)–(**c**) $G_{glia}$=16.7 *and* $\varepsilon$=0.23. In (**d**)–(**f**) we repeat the simulations in (**a**)–(**c**) using $G_{glia}$=26.7 *and* $\varepsilon$=0.003. For these parameters all cells in the network show high frequency seizure-like firing for higher $[K]_o$ values instead of going into depolarization block. As is clear from (*dA*) each cell exhibits regular spiking initially but shifts to seizure-like bursting for higher $[K]_o$ values (*dB*), and finally to a silent state (end of *dC*). There is a clear peak in the activity of the network at high $[K]_o$ values, indicating the increased synchrony in the network (**f**). The raster plot at peak activity is shown in (*dD*). The *solid* and *dashed lines* in (**e**) show $[K]_o$ and $[Na]_i$ trajectories respectively for the PC shown in (**d**). Parameter values used for simulation in this figure are $k_{o,\infty}$=14 mM, $\alpha_{ee}$=0.12, *and* $\alpha_{ei}$=0.2

depolarization block. In this slow time-scale setting the intervals between seizures are similar to that seen in seizure experiments (Fig. 2 of Ziburkus et al. 2006). Long-time scale intervals with network refractoriness have been also observed in cortical oscillations (Huang et al. 2004), neonatal burst firing (Leinekugel et al. 2002), spinal cord burst firing (Chub et al. 2006), up states (Shu et al. 2003), and interestingly in spreading depression (Somjen 2004; Kager et al. 2000).

After enhancing the glial uptake slightly (compared to the simulation in Fig. 5(a)–(c)) depolarization block disappears and all the neurons in the network show high frequency, lower amplitude seizure-like spiking when $[K]_o$ reaches a sufficiently high value during $[K]_o$ oscillations (Fig. 5(d),(e)). Like the previous example, each cell starts with slow spiking initially as $[K]_o$ starts rising (Fig. 5 dA) followed by rapid tonic firing at high $[K]_o$ (Fig. 5 dB). Finally, the network switches to a silent state as $[K]_o$ slowly falls to lower values (end of Fig. 5 dC) until the next cycle. In Fig. 5(e), we show $[K]_o$ and $[Na]_i$ for the same PC shown in Fig. 5(d). The increases in $[K]_o$ during seizures have been observed in other studies (Bazhenov et al. 2004; Fig. 1 of Bikson et al. 2003; Frohlich et al. 2008; Fig. 8 of Kager et al. 2000; Kager et al. 2007). The activity diagram (Fig. 5(f)) shows a clear peak at high $[K]_o$ values indicating increased but still partial (notice that the activity does not rise to 100 during seizures) spiking synchrony in the network. However, the longer time-scale oscillations (seizure episodes and $[K]_o$ oscillations) are more synchronized through the entire network. In Fig. 5 dD we show a raster plot for the network near the peak $[K]_o$ value during the cycle described above. The network shows a stable focus of activity for smaller $[K]_o$ values, which changes into seizure-like behavior for larger $[K]_o$ values (Fig. 5(f)), and interestingly is asynchronous, consistent with experimental (Figs. 11 and 12 of Netoff and Schiff 2002) and theoretical (Fig. 2 of Gutkin et al. 2001) findings.

## 4 Discussion

We have used a one-dimensional two-layer network model to study the physiological conditions under which a neuronal network can switch to a persistent state of activity, and the stability of the persistent state to perturbations. Previously, several experimental and theoretical studies have shown that spatially localized persistent activity in neuronal networks requires a balance between excitatory and inhibitory synaptic inputs (Compte et al. 2000; Funahashi et al. 1989; Gutkin et al. 2001). We show that the network not only needs balanced excitatory and inhibitory synaptic footprints, but also balanced levels of extracellular $K^+$, controlled by the glial syncytium, to achieve local persistent activity that is stable to perturbations.

Our study successfully models persistent activity during both the up state (Sanchez-Vives and McCormick 2000), and during the delay periods of working memory tasks using recurrent excitation balanced by local inhibition (Compte et al. 2000; Gutkin et al. 2001; Wang 1999). The persistent activity in our model can last for several seconds which has been observed in several experimental preparations (Fuster 1995; McCormick et al. 2003). In addition, the firing rate of our model PCs during the persistent activity is similar to that seen during the delay responses in memory tasks *in vivo* (Funahashi et al. 1989; Miller et al. 1996).

In recent years, neuroscience research has unveiled an unexpected complexity of glial cells. Astrocytes, in particular have been shown to affect virtually every aspect of neuronal function through glia-neuron cross talk. They have the ability to buffer excitatory ions such as $K^+$ from the interstitial volume (Amzica et al. 2002), preventing an undue increase in excitation of the neuronal network. They can also enhance the excitability of the network by releasing glutamate and ATP in a $Ca^{2+}$ dependent manner, which can activate NMDA and AMPA receptors synaptically and non-synaptically (Parpura et al. 1994; Parpura and Haydon 2000). In spite of a direct role of glia in the activity modulation of neuronal networks, detailed models of glia-neuron interaction are few (Nadkarni and Jung 2003). Here we use a model to show that dysfunction of glial cells can cause the transition from normal stable neuronal activity to seizure-like uncontrolled activity. Several experimental studies support glial dysfunction during epileptic seizures (Heinemann et al. 2000; Hinterkeuser et al. 2000). Our results support exploring therapeutic manipulations targeting glial function in regulating pathological activity such as seizures.

The ability of astrocytes to release glutamate in a $Ca^{2+}$ dependent manner has been recently extended by two groups to the glial bases of epilepsy (Tian et al. 2005; Kang et al. 2005). We tested the stability of the network to glial-induced excitatory perturbations by perturbing the network from its stable focus of activity by briefly raising the excitatory weight of the network. Our simulation shows that the ability of glial cells to induce seizure-like activity depends on the initial baseline state of the network. If the network is in a relatively low excitatory state, then a transient glial glutamate perturbation would not be able to cause epileptic activity no matter how strong the perturbations are. However, even a small perturbation by glial cells is enough to cause seizure-like activity in the network if its excitability set point is sufficiently high.

Recent experimental results point to the role of astrocytic domain reorganization in the epileptic brain (Oberheim et al. 2008). To test the effect of realistic spatial arrangements

of glia, spatially explicit models are needed. Such models would have to take into account the effect of extracellular tortuosity and explicit molecular diffusion between network elements, something beyond the scope of the present study.

There is an extensive literature that describes the stability of ensemble systems (Forster 1990), and indeed the fundamental hallmark of a stable (equilibrium) system in physics is reflected in how such systems handle fluctuations. We hypothesize that an analogous principle regarding the response to perturbations applies to characterize the stability of biological systems. We therefore examined the response of our extended network of INs and PCs to fluctuations. First we delivered a perturbation that created a persistently active state and then delivered a second perturbation. Depending upon the excitability of the network, which we could set through the synaptic efficacy (Fig. 3(b)), or the extracellular $K^+$ level (Fig. 3(c)), the response of the persistent state to the second perturbation was either exponential decay back to the persistent state, a runaway expansion of activity to break through the inhibitory constraints and involve more of or the whole network, or destruction of the persistent state with quiescence (behaviors illustrated in Fig. 3(b),(c)). Such competition between excitation and inhibition in response to perturbation appears to be reflected in an 'inhibitory veto' in such networks in cortex (Trevelyan et al. 2006).

Our findings are an extension of previous model studies that demonstrated bistable states in networks, i.e., to fulfill the working memory function, these models have found the physiological conditions under which the network can switch back and forth between a resting state and spatially structured activity induced by transient inputs (see for example Compte et al. 2000). We extended these findings to identify the conditions under which a network displaying stable persistent activity can switch to seizure-like states. The maintenance of a low $[K]_o$ is crucial to create persistent activity robust to perturbations. The $K^+$ mediated modulation described here likely will affect synaptic plasticity and homeostasis (Marder and Prinz 2002; Turrigiano 2008), and this warrants further investigation.

Neurophysiological studies of working memory by Miller et al. (1996) have shown that the delay activity in the prefrontal cortex of monkeys is resistant to occasional distractions. Through mathematical modeling these results were confirmed by Compte et al. (2000). This latter study related the distraction-resistant activity to the stimulus strength; that is, the activity packet was predicted to be resistant to small perturbations. The main finding of our study is that the network activity packet is stable provided that (1) the excitable synaptic strength is not too high (a parameter modulated by glial glutamate release); (2) $[K]_o$ is low enough to be within the physiological range (i.e. the glial network buffer is functioning properly); and (3) the perturbations are not too strong. Thus our study asserts two additional conditions on the stability of the neuronal activity. Even small perturbations can push the network to an unstable state if the network is already in a state of increased $\alpha_{ee}$ *or the* $[K]_o$ *is relatively high. Both of these conditions are regulated by a properly functioning glial network.*

The evolution of activity seen in Fig. 5(a),(d) is intimately linked to the ionic dynamics shown in Fig. 5(b),(e). Without incorporating such ionic and glial dynamics, such evolution would not appear. Seizure patterns, whether observed *in vitro* (Ziburkus et al. 2006), or from human patients recorded from scalp or intracranial electrodes (Schiff et al. 2005), demonstrate a prominent and very consistent evolution from initiation to termination. Whether such evolution observed from such different scales of experimental observation is related to the ionic and glial dynamics studied here is an intriguing question that warrants further exploration.

Although brains are not equilibrium systems, we propose that how neuronal networks respond to perturbations, and how the response to such perturbations decays (or grows), are critical determinants of the state of the brain, with parallels to other physical systems (Forster 1990). How neuronal networks respond to perturbations determines how transient patterns of activity emerge from background activity in response to internal fluctuations of activity or external stimuli. We propose that the response of a balanced, or mildly imbalanced network, to such perturbations is a fundamental feature which may underlie a variety of disparate transient phenomena such as seizures, working memory, up states, cortical oscillations, and spinal cord and hippocampal neonatal burst firing.

**Acknowledgements** We thank Jokubas Ziburkus, Andrew J Trevelyan, Maxim Bazhenov, and Partha Mitra, for their valuable discussions. This work was funded by NIH Grants K02MH01493 (SJS), R01MH50006 (SJS, GU), F32NS051072 (JRC), and CRCNS-R01MH079502 (EB).

## References

Amzica, F., Massimini, M., & Manfridi, A. (2002). Spatial buffering during slow and paroxysmal sleep oscillations in cortical networks of glial cells *in vivo*. *Journal of Neuroscience*, *22*(3), 1042–1053.

Bazhenov, M., Timofeev, I., Steriade, M., & Sejnowski, T. J. (2004). Potassium model for slow (2–3 Hz) *in vivo* neocortical paroxysmal oscillations. *Journal of Neurophysiology*, *92*, 1116–1132.

Bikson, M., Hahn, P. J., Fox, J. E., & Jefferys, J. G. R. (2003). Depolarization block of neurons during maintenance of electrographic seizures. *Journal of Neurophysiology*, *90*(4), 2402–2408.

Chub, N., Mentis, Z. G., & O'Donovan, J. M. (2006). Chloride-sensitive MEQ fluorescence in chick embryo motoneurons following manipulations of chloride and during spontaneous network activity. *Journal of Neurophysiology*, *95*, 323–330.

Compte, A., Brunel, N., Goldman-Rakic, P. S., & Wang, X. J. (2000). Synaptic mechanisms and network dynamics underlying spatial working memory in a cortical network model. *Cerebral Cortex*, *10*(9), 910–923.

Cressman, J. R., Ullah, G., Ziburkus, J., Schiff, S. J., & Barreto, E. (2009). The influence of sodium and potassium dynamics on excitability, seizures, and the stability of persistent states: I. Single neuron dynamics. *Journal of Computational Neuroscience*. doi:10.1007/s10827-008-0132-4.

Durstewitz, D., Seamans, J. K., & Sejnowski, T. J. (2000). Neurocomputational models of working memory. *Nature Neuroscience*, *3*, 1184–1191.

Fellin, T., Gomez-Gonzalo, M., Gobbo, S., Carmignoto, G., & Haydon, P. G. (2006). Astrocytic glutamate is not necessary for the generation of epileptiform neuronal activity in hippocampal slices. *Journal of Neuroscience*, *26*(36), 9312–9322.

Fisher, R. S., Pedley, T. A., & Prince, D. A. (1976). Kinetics of potassium movement in norman cortex. *Brain Research*, *101*(2), 223–237.

Forster, D. (1990). *Hydrodynamic fluctuations, broken symmetry, and correlation*. Boulder: Westview.

Frohlich, F., Timofeev, I., Sejnowski, T. J., & Bazhenov, M. (2008). Extracellular potassium dynamics and epileptogenesis. In I. Soltesz, & K. Staley (Eds.), *Computational neuroscience in epilepsy*. Amsterdam: Academic.

Fujiwara-Tsukamoto, Y., Isomura, Y., Kaneda, K., & Takada, M. (2004). Synaptic interactions between pyramidal cells and interneuron subtypes during seizure-like activity in the rat hippocampus. *Journal of Physiology*, *557*(3), 961–979.

Funahashi, S., Bruce, C. J., & Goldman-Rakic, P. S. (1989). Mnemonic coding of visual space in the monkey's dorsolateral prefrontal cortex. *Journal of Neurophysiology*, *61*(2), 331–349.

Fuster, J. M. (1995). *Memory in the cerebral cortex*. Cambridge: MIT.

Goldman-Rakic, P. S. (1995). Cellular basis of working memory. *Neuron*, *14*(3), 477–485.

Gutkin, B. S., Laing, C. R., Colby, C. L., Chow, C. C., & Ermentrout, G. B. (2001). Turning on and off with excitation: the role of spike-timing asynchrony and synchrony in sustained neural activity. *Journal of Computational Neuroscience*, *11*(2), 121–134.

Heinemann, U., Gabriel, S., Jauch, R., Schulze, K., Kivi, A., Eilers, A., et al. (2000). Alterations of glial cell function in temporal lobe epilepsy. *Epilepsia*, *41*(Suppl. 6), S185–S189.

Hinterkeuser, S., Schroder, W., Hager, G., Seifert, G., Blumcke, I., Elger, C. E., et al. (2000). Astrocytes in the hippocampus of patients with temporal lobe epilepsy display changes in potassium conductances. *European Journal of Neuroscience*, *12*(6), 2087–2096.

Huang, X., Troy, W. C., Yang, Q., Ma, H., Laing, C. R., Schiff, S. J., et al. (2004). Spiral waves in disinhibited mammalian neocortex. *Journal of Neuroscience*, *24*, 9897–9902.

Kager, H., Wadman, J. W., & Somjen, G. G. (2000). Simulated seizures and spreading depression in a neuron model incorporating interstitial space and ion concentrations. *Journal of Neurophysiology*, *84*, 495–512.

Kager, H., Wadman, J. W., & Somjen, G. G. (2007). Seizure-like afterdischarges simulated in a model neuron. *Journal of Computational Neuroscience*, *22*, 105–128.

Kang, N., Xu, J., Xu, Q., Nedergaard, M., & Kang, J. (2005). Astrocytic glutamate release-induced transient depolarization and epileptiform discharges in hippocampal CA1 pyramidal neurons. *Journal of Neurophysiology*, *94*(6), 4121–4130.

Konnerth, A., Heinemann, U., & Yaari, Y. (1984). Slow transmission of neural activity in hippocampal area CA1 in absence of active chemical synapses. *Nature*, *307*, 69–71.

Leinekugel, X., Khazipov, R., Cannon, R., Hirase, H., Ben-Ari, Y., & Buzsaki, G. (2002). Correlated bursts of activity in the neonatal hippocampus *in vivo*. *Science*, *298*(5575), 2049–2052.

Marder, E., & Prinz, A. A. (2002). Modulating stability in neuron and network function: The role of activity in homeostasis. *BioEssays*, *24*, 1145–1154.

Mason, A., & Larkman, A. (1990). Correlations between morphology and electrophysiology of pyramidal neurons in slices of rat visual cortex. II. Electrophysiology. *Journal of Neuroscience*, *10*(5), 1415–1428.

Mazel, T., Simonova, Z., & Sykova, E. (1998). Diffusion heterogeneity and anisotropy in rat hippocampus. *Neuroreport*, *9*(7), 1299–1304.

McBain, C. J., Traynelis, S. F., & Dingledine, R. (1990). Regional variation of extracellular space in the hippocampus. *Science*, *249* (4969), 674–677.

McCormick, D. A., Shu, Y., Hasenstaub, A., Sanchez-Vives, M., Badoual, M., & Bal, T. (2003). Persistent cortical activity: Mechanisms of generation and effects on neuronal excitability. *Cerebral Cortex*, *13*, 1219–1231.

Miller, E. K., Erickson, C. A., & Desimone, R. (1996). Neural mechanisms of visual working memory in prefrontal cortex of the macaque. *Journal of Neuroscience*, *16*(16), 5154–5167.

Miller, P., Brody, C. D., Romo, R., & Wang, X. J. (2003). A recurrent network model of somatosensory parametric working memory in the prefrontal cortex. *Cerebral Cortex*, *13*, 1208–1218.

Murray, J. D. (2003). *Mathematical Biology II: Spatial models and biomedical applications*. New York: Springer.

Nadkarni, S., & Jung, P. (2003). Spontaneous oscillations of dressed neurons: A new mechanism for epilepsy? *Physical Review Letters*, *91*(268101), 1–4.

Netoff, T. I., & Schiff, S. J. (2002). Decreased neuronal synchronization during experimental seizures. *Journal of Neuroscience*, *22*, 7297–7307.

Oberheim, N. A., Tian, G. F., Han, X., Peng, W., Takano, T., Ransom, B., et al. (2008). Loss of astrocytic domain organization in the epileptic brain. *Journal of Neuroscience*, *28*(13), 3264–3276.

Parpura, V., & Haydon, P. G. (2000). Physiological astrocytic calcium levels stimulate glutamate release to modulate adjacent neurons. *Proceedings of the National Academy of Sciences of the United States of America*, *97*, 8629–8634.

Parpura, V., Basarsky, T. A., Liu, F., Jeftinija, K., Jeftinija, S., & Haydon, P. G. (1994). Glutamate-mediated astrocyte–neuron signalling. *Nature*, *369*(6483), 744–747.

Perez-Velazquez, J. L., & Carlen, P. L. (1999). Synchronization of GABAergic interneuronal networks during seizure-like activity in the rat horizontal hippocampal slice. *European Journal of Neuroscience*, *11*, 4110–4118.

Pinto, D. J., Patrick, S. L., Huang, W. C., & Connors, B. W. (2005). Initiation, propagation, and termination of epileptiform activity in rodent neocortex *in vitro* involve distinct mechanisms. *Journal of Neuroscience*, *25*(36), 8131–8140.

Rainer, G., Asaad, W. F., & Miller, E. K. (1998). Memory fields of neurons in the primate prefrontal cortex. *Proceedings of the National Academy of Sciences of the United States of America*, *95*, 15008–15013.

Romo, R., Brody, C. D., Hernandez, A., & Lemus, L. (1999). Neuronal correlates of parametric working memory in the prefrontal cortex. *Nature*, *399*(6735), 470–473.

Sanchez-Vives, M. V., & McCormick, D. A. (2000). Cellular and network mechanisms of rhythmic recurrent activity in neocortex. *Nature Neuroscience*, *3*, 1027–1034.

Schiff, S. J., Sauer, T., Kumar, R., & Weinstein, S. L. (2005). Neuronal spatiotemporal pattern discrimination: The dynamical evolution of seizures. *NeuroImage*, *28*, 1043–1055.

Shu, Y., Hasenstaub, A., & McCormick, D. A. (2003). Turning on and off recurrent balanced cortical activity. *Nature*, *423*(6937), 288–293.

Soltesz, I., & Staley, K. (2008). *Computational neuroscience in epilepsy*. Amsterdam: Academic.

Somjen, G. G. (2004). *Ions in the brain: normal function, seizures, and stoke*. Oxford: Oxford University Press.

Tian, G. F., Azmi, H., Takano, T., Xu, Q., Peng, W., Lin, J., et al. (2005). An astrocytic basis of epilepsy. *Nature Medicine*, *11*(9), 973–981.

Trevelyan, A. J., Sussillo, D., Watson, B. O., & Yuste, R. (2006). Modular propagation of epileptiform activity: Evidence for an inhibitory veto in neocortex. *Journal of Neuroscience*, *26*(48), 12447–12455.

Turrigiano, G. G. (2008). The self-tuning neuron: Synaptic scaling of excitatory synapses. *Cell*, *135*, 422–435.

Van Vreeswijk, C., & Sompolinsky, H. (1996). Chaos in neuronal networks with balanced excitatory and inhibitory activity. *Science*, *274*(5293), 1724–1726.

Vogels, T. P., Rajan, K., & Abbott, L. F. (2005). Neural network dynamics. *Annual Review of Neuroscience*, *28*, 357–376.

Wang, X. J. (1998). Calcium coding and adaptive temporal computation in cortical pyramidal neurons. *Journal of Neurophysiology*, *79*(3), 1549–1566.

Wang, X. J. (1999). Synaptic basis of cortical persistent activity: the importance of NMDA receptors to working memory. *Journal of Neuroscience*, *19*(21), 9587–9603.

Wang, X. J. (2003). Persistent neuronal activity: Experiments and theory. *Cerebral Cortex*, *13*, 1123.

Ziburkus, J., Cressman, J. R., Barreto, E., & Schiff, S. J. (2006). Interneuron and pyramidal cell interplay during *in vitro* seizure-like events. *Journal of Neurophysiology*, *95*, 3948–3954.